Enabling Single Molecule Fluorescence Microscopy Investigations of Chemical Reactions Using a Spiroconjugated BODIPY Fluorophore

By

Daniel A. Hinton

A dissertation submitted in partial fulfillment
of the requirements for the degree of

Doctor of Philosophy

(Chemistry)

at the

UNIVERSITY OF WISCONSIN – MADISON

2018

Date of final oral examination: December 10, 2018

This dissertation is approved by the following members of the Final Oral Committee:

Randall Goldsmith, Associate Professor, Chemistry
Tehshik Yoon, Professor, Chemistry
Jennifer Schomaker, Professor, Chemistry
A.J. Boydston, Professor, Chemistry

Abstract

Single-molecule fluorescence microscopy can provide invaluable insights into chemical phenomena by means of direct observation and transition-metal catalyzed reactions provide a rich area for such exploration. Using single-molecule spectroscopy provides a means of observing individual catalyst molecules behaving under relevant conditions to *directly* probe otherwise hidden but meaningful species and measure reaction dynamics in real time. The development of more efficient catalysts follows from deeper mechanistic understanding. As the demand for more active and selective catalysts grows, so too does the need for improved measurements.

This thesis describes research in this area with an emphasis on the rational design and synthesis aspects. A spiroconjugated red BODIPY fluorophore was selected from the literature and adapted to single-molecule fluorescence microscopy investigations. The red BODIPY was modified with a silyl ether handle and immobilized on glass coverslips and its base stability was analyzed as a model compound for silyl ether supported fluorophore-labeled catalysts. Next, a nobornene monomer labeled with the red BODIPY was synthesized for the purpose of investigating polymerization reactions and an unexpected photophysical discovery was made. The results of the characterization and mechanism developed are detailed in this thesis.

The final chapter of this thesis describes synthetic progress toward a FRET-based high-throughput screening platform. A system has been rationally designed involving fluorophore-labeled reaction partners of the Phenolic Kinetic Resolution reaction as a proof-of-concept system for the rapid determination of enantiomeric excess for enantioselective nucleophilic ring-opening reactions.

Acknowledgements

I am so glad that I chose to go to graduate school at UW-Madison and join the Goldsmith Group. I would like to thank Randy for being such an enthusiastic and inspiring advisor. Randy has an unwavering commitment to scientific research and he is always responsive, available, and caring. Over the years, Randy has taught me how to be an efficient, open-minded, and critical scientist. I will also be forever grateful to Randy for supporting my personal development by allowing me to do research abroad at the Tokyo Institute of Technology for three months via NSF GROW. I learned a tremendous amount in those three months and the GROW program helped me develop confidence in myself which I will have for the rest of my life. Thank you so much, Randy. I also thank the NSF for funding via the NSF GRFP program and for offering the NSF GROW program to fellows.

The Goldsmith Group has been a joy to work with through the years. This group is hardworking, talented, and caring. I thank Sunil Upadhyay for so much of my training. Sunil can seemingly synthesize any target molecule given to him and he taught me with great patience and enjoyment how to tackle the syntheses of a variety of molecules. I will also never forget his amazing food which he was always so generous in sharing. In general, the Goldsmith group has always had plenty of food to share, which has been fantastic. I thank James for his patience with all my questions and tolerating me in times of high stress. I will never forget the day we drove to Chicago in the pouring rain to run experiments in the Wasielewski lab. I also would like to thank him for all his work toward our JACS paper together, in addition to those experiments. I thank Angela for being such an excellent lab mate. On top of being extremely intelligent, Angela was always a joy to work with. I also will always miss the dock parties Angela and Scott threw at their apartment. They played a huge role in making our department such a great place to be a student. I thank Lydia for being such an excellent lab leader and keeping all of us on track as well as always being willing to give advice and edit document drafts.

Lydia and I have had some funny times together as well (she loves messing with me, that's for sure). Morgan has also been great at this and I had such a good time at group dinner when went to Dlux recently (which was organized by Morgan) just to give one example. Andrew has been an excellent colleague, roommate, and friend for years. He provides such a great example for being a patient, open-minded, critical thinker. I thank Katie for being a great friend and for so many good memories both in and outside the lab (many of which involve excellent meals or Roller Derby) in addition to her work for our Langmuir paper. Mike Foy was the undergraduate I worked with the longest. It was always a pleasure working with such an intelligent and motivated student. He showed me what young researchers are capable of when they are driven and focused. I would also like to give Kasie Knapper a shoutout as a fellow Southerner who has been a great friend and someone I could discuss things I have missed about home with (such as the significantly better weather).

UW-Madison is a truly collaborative department, which has made our department such an enjoyable place to be a student and researcher. I thank Tehshik Yoon for being so kind and allowing me to join his research group meetings. I learned a great deal from Tehshik and his students over the years and thank him for being a committee member for my TBO as well as my thesis defense. I also thank Jen Schomaker and A.J. Boydston for serving on my committee. I learned so much in Jen's NMR course and I would like to wish A.J. a warm welcome and the best of luck here. I thank the other wonderful faculty here who I've interacted with in various ways and who taught me during my coursework. The staff here are also excellent. I thank Ilia Guzei for all his help with crystallography; Charlie Fry and Heike Hofstetter for help in the NMR facility; and Martha Vestling for all the mass spec assistance. I will miss my time at UW-Madison and I have a lot of great memories to look back on in my future on top of the excellent training.

I also thank my parents for always encouraging me to realize my full potential.

Contents

Figures

Tables

Chapter 1

1. Introduction

1.1 Single-Molecule Fluorescence Microscopy: History and Reactions Involving Small Molecules

Single-molecule fluorescence microscopy can provide invaluable insights into chemical phenomena by means of direct observation. Homogeneous transition-metal catalysis provides a rich area for such exploration. In the past, kinetic analyses on the bulk scale have been used to study reaction rates and the factors that affect them. However, ensemble measurements have inherent limitations. The outcome of catalytic reactions can be dominated by short-lived intermediates which cannot be probed by conventional spectroscopic techniques because their equilibrium concentrations are simply too low or because they exist beyond the rate determining step on the reaction coordinate. As a catalytic cycle progresses, these transient species form and diminish in an unsynchronized manner across the ensemble. Nonetheless, single molecule spectroscopy provides a means of observing individual catalyst molecules behaving under relevant conditions to *directly* probe these otherwise hidden but meaningful species. The history of organic synthesis has shown that the development of more efficient catalysts follows from deeper mechanistic understanding. As the demand for more active and selective catalysts grows, so too does the need for improved measurements.

The study of individual biomolecules constitutes most of the literature on single-molecule experiments.[1-5] Major discoveries have been made by measuring the catalytic activity of individual enzymes. It is now known that individual enzymes in an ensemble do not catalyze the same reaction at the same rate. This observation constitutes a case of *static* heterogeneity.[5] A growing body of evidence suggests that there exists a distribution of rate constants within the ensemble – not all the enzymes function at the same velocity.[5] In addition, *dynamic* heterogeneity has been observed due to the existence of rate constants for individual enzymes fluctuating over time.[5] These findings have motivated studying nanoparticle and molecular transition-metal catalyzed reactions in more recent times.

Some of the earliest reports of single-molecule level investigations of chemical reactions involve measurements of nanoparticle-catalyzed reactions[6] and reactions at the surfaces of large crystals.[7] In one of the first reports, the Hofkens lab describes the real-time monitoring of chemical reactions occurring at single organic molecules, which were catalyzed by crystals of a double layered hydroxide in solution.[7] The reactions in this case were an ester hydrolysis and transesterification.[7] This was accomplished using wide field microscopy and observing a fluorogenic reaction of a fluorescein-based probe at room temperature and ambient pressure, in contrast to measurements performed on model reactions under less relevant vacuum conditions.[7] The researchers found that the reactions are spatially localized with the hydrolysis occurring on one face and transesterification on another by performing the reaction in aqueous conditions and again in alcohol solvent.[7] The Hofkens lab has since published more work on fluorogenic reactions at nanoparticles[8] and measuring individual steps in catalytic cycles.[9] The Chen group reported in 2008 on observing single turnover events of a fluorogenic reaction at gold nanoparticles.[6] The reaction is the reduction of resazurin to resorufin by hydroxylamine being imaged using a total internal reflection fluorescence (TIRF) setup.[6] By probing the reaction beyond the ensemble level, the researchers were able to discover heterogeneous reaction pathways and surface structural dynamics which would have been otherwise hidden by ensemble averaging.[6] The Chen group has since performed similar experiments on other reactions catalyzed by gold nanoparticles[10-14] as well as palladium[11] and platinum nanoparticles.[15, 16] In addition, the Scaiano group has published on investigations involving the copper(I)-catalyzed alkyne-azide cycloaddition "click" reaction as catalyzed by copper nanoparticles as well as Cu@charcoal.[17, 18]

There are more recent reports of work being performed on elementary reactions of transition metal complexes. One of the first publications in this area by the Herten group describes measuring metal-coordination by designing a photoswitch system and tracking its fluorescence quenching at the single-molecule level.[19] The researchers accomplish this by the design and implementation of a carefully engineered system with a glass surface bound to an oligonucleotide photoswitch via streptavidin/biotin chemistry.[19] The oligonucleotide photoswitch contained a bypyridine site on one oligonucleotide and a tetramethylrhodamine complex bound to the connected oligonucleotide.[19] When Cu(II) binds to the bypyridine, the rhodamine complex nearby becomes quenched.[19] This creates a system which begins fluorescent and then becomes non-fluorescent upon metal binding, from which the formation and dissociation of the copper(II)-bipyridine can be measured at the single-molecule level.[19] The Blum group has reported on the imaging of platinum-sulfur exchange reactions, furthering the understanding of elementary organometallic reactions.[20-22] The first report by the Blum group describes the TIRF imaging of boron-dipyrromethane (BODIPY)-labeled platinum complexes in solution reacting with a thiourea-functionalized glass coverslips.[21] The ligand exchange reaction *at platinum* (the BODIPY acts as a spectator in which no reaction occurs at the BODIPY and the BODIPY does not become quenched) generates a fluorescent, immobilized spot on the glass surface that becomes illuminated via TIRF while the fluorescent ligand in solution exists outside the excitation volume and remains invisible.[21] It was demonstrated from this experiment that a single ligand exchange reaction at the surface does not influence where future ligand exchange reactions occur, meaning the reactions are uncorrelated.[21] The Blum group later published a paper which expounded upon this work and explains how these measurements provide information inaccessible to traditional techniques and AFM[20] in addition to publishing on the deconvolution of the biexponential first-order kinetics of this reaction.[22] The Blum lab has more recently published on the formation of organozinc reagents, which is a fundamental step in the Negishi coupling reaction.[23, 24]

1.2 Single-Polymer Measurements

Polymers are ubiquitous in modern society and their importance for improving quality of life and impact on the environment cannot be overstated. There exists a great need for more detailed and fundamental studies of polymer physics and chemistry and there is an expansive and growing body of research in this area. While many examples exist and continue to be reported on the dynamics of the chemistry of small molecules using single-molecule fluorescence microscopy, an underexplored but related area of research awaits in measurements on polymerization dynamics of single polymers. Most experiments combining fluorescence microscopy and single polymers involve pre-formed conjugated (with some exceptions involving non-conjugated polymers) polymers such as poly(carbazole) and poly(fluorene) derivatives.[25-34] One report by the Hofkens lab describes progress made toward observing polymerization dynamics by monitoring the polymerization of styrene at the single-molecule level by tracking the diffusion constant of dyes within the polystyrene being formed.[35] However, this measurement was an indirect measurement of the kinetics and was not performed in real-time. The Vacha group has published extensively on the study of single polymer chains imaged at room temperature to investigate exciton dynamics,[25, 30] diffusion[27, 29] as well as the spatial location of emission.[26]

One drawback to these experiments lies in the fact that these polymers are imaged in a polymeric host matrix, which restricts conformational flexibility and makes drawing conclusions for the behavior of polymers in organic solvent difficult.[36] However, there are some recent reports of experiments performed on single polymer chains in organic solvent in a conformationally non-restricted system.[36, 37] A report by Tenopala-Carmona et al. in 2018 describes an experiment in which single polymer chains are examined in organic solvent by covalently anchoring one end of the polymer to a surface via silane chemistry.[36] The researchers examine pre-formed poly(3-hexylthiophene)

(P3HT) using single-molecule fluorescence microscopy in *ortho*-dichlorobenzene, a known "good" solvent for P3HT, and DMSO, a "poor" solvent.[36] By examining populations of single polymer chains, they discovered a great deal of heterogeneity exists between and within polymer chains which is a function of solvent quality as well as the molecular weight/length of polymer.[36] In addition, they were able to probe the conformational switching of the polymer chains induced by rapid solvent changes in real time.[36] A report by Liu et al. combines many of these advantages such as observations of single polymers in organic solvent, but differs in an important manner by being the first publication definitively characterizing the dynamics of single polymer chains during their growth/formation over the course of a Ring Opening Metathesis Polymerization (ROMP) (Figure 1-1).[37] In addition, the report does not rely on a fluorescent reporter of any sort.[37] The real time measurements are made using molecular tweezers by attaching a functionalized Grubbs catalyst to a magnetic particle on one end and a silyl ether functionalized norbornene monomer attached to the other end at the surface of a glass coverslip.[37] A force is applied which pulls the polymer up from the surface in a solution

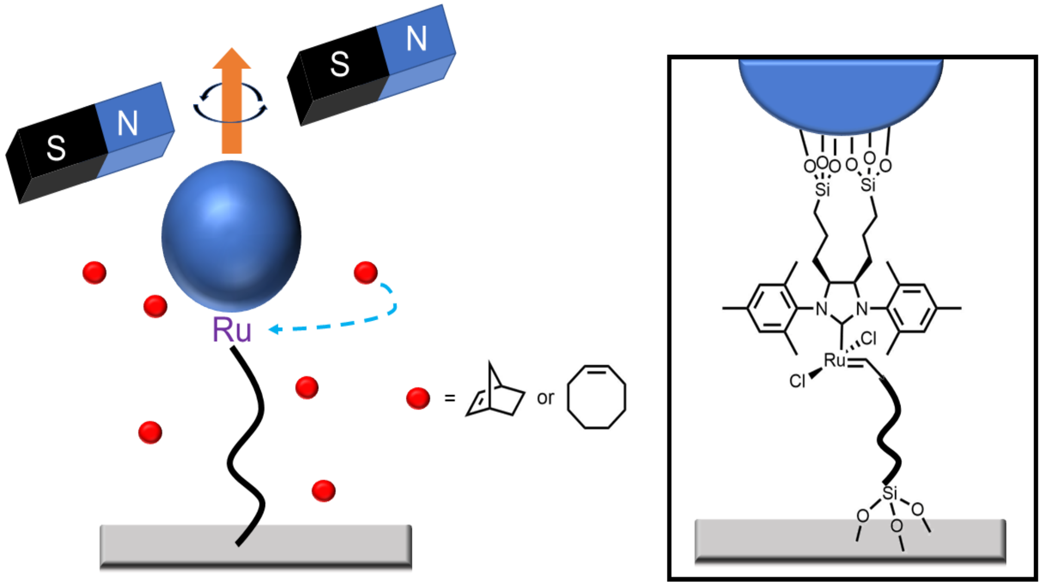

Figure 1-1. Single-polymer experiment investigating growth dynamics. (Left) The polymer grows as the entire chain is pulled using mechanical tweezers due to the catalyst being attached to a magnetic nanoparticle. (Right) The structure of the Grubbs catalyst modified for attachment to the magnetic particle at the NHC ligand. Figure adapted from reference 37.

containing norbornene monomer (as well as performing the experiment with *cis*-cyclooctene) in toluene.[37] The growth of the polymer occurring in real time was observed by determining the location of the magnetic particle.[37] The researchers discovered that growing polymer chains do not lengthen continuously.[37] Instead, there are "wait" and "jump" steps due to entanglements of monomers the authors refer to as "hairballs".[37] In addition to publishing work on ligand exchange events[20-22] (as discussed previously), the Blum group has also reported using single-molecule fluorescence microscopy to investigate ROMP in which they elucidated (spatially) whether the reaction was homogeneous vs. heterogeneous[38] as well as observing the incorporation of single monomers catalyzed by clusters of ruthenium catalysts.[39, 40] These reports highlight the difficulties of measuring the dynamics of polymerization reactions at the single-molecule/polymer level as well as indicate that the future holds plenty of room for exploration as there are a multitude of polymerization mechanisms to be investigated and this can be achieved using non-immobilized molecules as well as supported molecules and anything from fluorescent dyes to magnetic tweezers.

1.3 Fluorophore Selection

Fluorescent labels are usually a necessary component for performing measurements on catalytic reactions at the single-molecule level. The molecules of interest must be targeted amongst a multitude of molecules in the solvent and medium. Many design considerations are taken in order to enable such experiments. It is crucial to ensure that the optimal amount of information is obtained with minimal interference to the catalytic cycle. In addition, performing measurements on transition-metal catalyzed reactions requires using dyes which are soluble in organic solvents, as opposed to experiments on enzymes performed in water. Because of this, using non-commercial, tailor-made dyes is necessary[41] and opens up new areas for discovery as the single-molecule level photodynamics of fluorescent dyes have, to the best of our knowledge, only been examined in water.[42, 43]

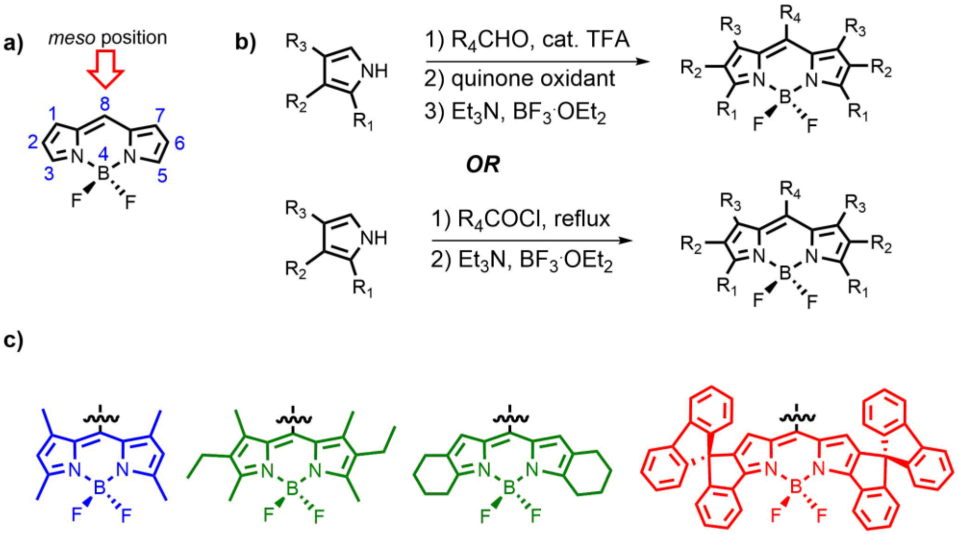

Figure 1-2. BODIPY basics. a) BODIPY core structure with nomenclature displayed. b) BODIPY-forming conditions for aldehydes (top) and acyl chlorides (bottom). c) Selected structures of BODIPYs.

BODIPY dyes are an attractive class of dyes to use in these experiments (Figure 1-2). BODIPY dyes are soluble in organic solvents and feature fewer potential coordination sites than related organic dyes, such as coumarins, rhodamines, and cyanines.[44] There also exists precedence for their use in single-molecule fluorescence experiments.[21, 38, 45-50] In addition, BODIPY dyes can be synthetically modified to fit the specific demands of a given experiment. BODIPY dyes also have many attractive features for spectroscopic measurements as they are typically bright, stable, high quantum yields, and small Stokes shifts (~5-10 nm),[51, 52] and many of these properties are responsible for their wide usage in the labeling of biomolecules such as proteins and DNA.[51] A typical BODIPY dye is synthesized by combining a functionalized pyrrole (some of which are commercially available) with an acyl chloride or aldehyde in a one-pot, multi-step reaction (Figure 1-2). The *meso* position as well as the 4 position (B-F bond) offer perhaps the most straightforward locations for attaching the BODIPY to other molecules of interest. The former can be accomplished by functionalizing the aldehyde or acyl chloride prior to the BODIPY-forming reaction. Substitution at the *meso* position also results in a negligible change in the absorption and fluorescence spectra of BODIPYs, which is supported both empirically and by theory, and offers a predictable and reliable method for producing BODIPYs with intended spectral features. The latter, substitution of the B-F bond, typically involves substituting with alkoxy, alkyl, alkynyl, or aryl functional groups using alkoxides or Grignard and organolithium reagents.[51] Depending on sterics, substituting at the B-F position can have significant, noticeable effects on the absorption and fluorescence spectra as well as the quantum yield. For instance, the quantum yield can decrease drastically when substituting the same core BODIPY structure from methyl ($\Phi = 0.33$) to *n*-butyl ($\Phi = 0.06$) groups.[51] Substituting with aryl groups has also been shown to result in red-shifts in the fluorescence emission wavelengths in polar solvents.[51]

A spiroconjugated red BODIPY has proven to be effective in many single-molecule fluorescence microscopy experiments. A red BODIPY was chosen because red-absorbing dyes have been shown to be beneficial for reducing background as a consequence of the longer excitation and detection wavelengths used.[53] This confers another handle for reducing background in addition to intensive solvent purification steps. The red BODIPY also contains spirofluorene groups, which been shown to reduce self-induced quenching in other chromophores.[54] The spirofluorene moieties are in conjugation with the BODIPY core, which results in a red-shift in the absorption and fluorescence spectra. However, the non-planarity of the groups was hypothesized to decrease the propensity for

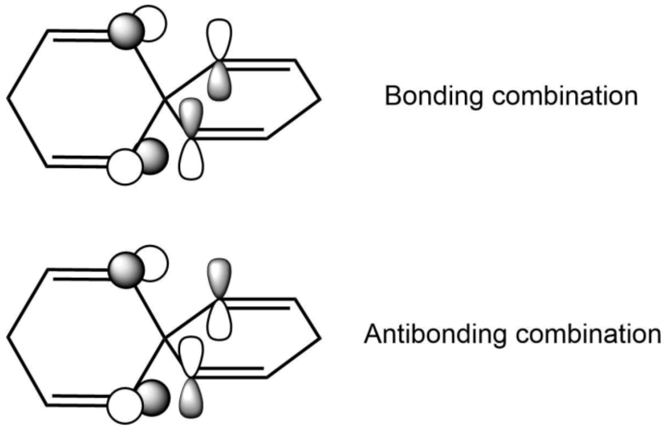

Figure 1-3. Simplified orbital diagram for a model spiroconjugated system.

aggregation when it was selected for the experiments in this report. Additionally, the quantum yield is higher than similar red dyes due to the rigidity of the spiro groups.[55] Calculations performed on four *p*-orbitals which are orthogonal to one another in pairs show that there is a through-space interaction with an overlap integral that is 20 % of the value for four *p*-orbitals in a planar, π-conjugated system (Figure 1-3).[56] The selected red BODIPY can also be excited with a commercial 633 nm laser. The pyrrole synthesis involves four straightforward steps which can be performed on a relatively large scale (> 10 g) and proves stable enough to be stored for extended periods (> 2 years).[55] Thus far, the red BODIPY scaffold has been derivatized in a variety of ways at the *meso* position and has been a reliable fluorophore for many single-molecule experiments, particularly in protic organic solvents such as 2-propanol (IPA).

1.4 Outline

This thesis reports on the rational design and synthesis aspects of enabling investigations of transition-metal catalysts using single-molecule fluorescence microscopy. Chapter 2 describes the design and synthesis of a silyl ether functionalized BODIPY fluorophore and the evaluation of its base stability as well as its use as a model compound to investigate the initiation dynamics of a palladium catalyst at the single-molecule level. In Chapter 3, an unexpected photophysical discovery involving a norbornene monomer labeled with the same BODIPY fluorophore is described. Chapter 4 focuses on the synthetic progress toward a new high-throughput screening system.

Chapter 2

2. Development of Surface Chemistry and Single Molecule Investigation of the Initiation Dynamics of a Molecular Palladium Catalyst

Part of this chapter was published in *Langmuir*, **2016**, *32* (36), 9171-9179 and *J. Am. Chem. Soc.*, **2016**, *138* (11), 3876-3883. It was amended for this thesis. My contributions to these publications were in the design, synthesis, and characterization of the red BOIDPY fluorophore label and the synthesis of the silyl-ether functionalized molecules (not of the final product labeled PEPPSI catalyst molecule) as well as intellectual contributions.

2.1 Abstract

Single-molecule fluorescence microscopy has proven to be a powerful method for the observation of dynamics and behavior of biological systems and has recently begun to be employed in chemical systems. In order to study the initiation dynamics of a molecular palladium catalyst, the catalyst had to be immobilized on the silica surface of an all glass reaction chamber. A model compound was designed and synthesized and the surface stability in the presence of base (KOtBu) was evaluated so that the data for the initiation dynamics could be reliably analyzed. The model compound enabled the investigations of silyl ether-silica chemistry at the single-molecule level as well as the first single-molecule investigation of catalyst initiation dynamics for a molecular palladium catalyst.

2.2 Introduction

The surface stability of a silyl ether-silica linkage in response to basic conditions was investigated using a surface-linked BODIPY molecule as a probe. The nature of the linkage between the molecular species and surface support is an important consideration when designing surface-supported catalysts. A variety of deposition conditions are employed in the literature for attaching silyl ether functionality to silica surfaces, differing significantly in time of reaction, temperature, and use of blocking layers.[57-60] The surface-supported BODIPY model compound was used to investigate the viability of these conditions in the presence of various concentrations of base (potassium *tert*-butoxide, KOtBu). We selected KOtBu as a target base because it is an effective base for Suzuki reactions in isopropanol[61] and is highly soluble in isopropanol.

To systematically investigate the influence of different conditions, three alkylsiloxane surface support deposition schemes were used, varying the use of thermal annealing and use of an alkylsiloxane blocking layer. In the first two procedures, only the alkylsiloxane-functionalized probe

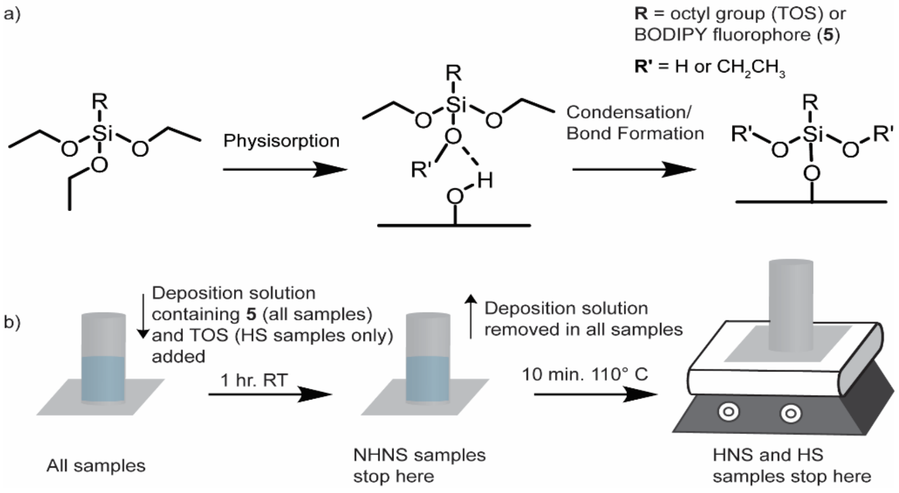

Figure 2-1. Deposition scheme. a) Suggested mechanism for bond formation between an alkylsiloxane and bare silica surface including physisorption step, where hydrogen bonding is the principle means of attaching the alkylsiloxane to the surface, and a thermal annealing step, where covalent bond formation occurs. b) shows a simplified procedure for depositing compound **5** at the silica surface.

molecule, compound **5**, is deposited with no silane blocking layer, with one procedure undertaken solely at room temperature (no heat no silane, NHNS) and the other including a post-deposition heating step (heat, no silane, HNS). In the third deposition procedure, **5** is co-deposited with a high concentration of a commercially available alkylsiloxane, triethoxyl octyl silane, to create a nonpolar barrier which helps resist base attack.[62] These samples are termed HS (for their inclusion of the TOS blocking layer) and were thermally annealed like the HNS sample after the initial deposition. By investigating samples with and without a heating step, the effect of heating on the strength of the surface bond is investigated. It has been shown that hydrogen bonding may be a major mode of surface attachment in unheated films and that heat curing produces covalently bound siloxane.[63, 64] Thus, surface attachment may be represented by the mechanism shown in Figure 2-1 and a thermal annealing step may be necessary to ensure a stable surface bond. Two places are left ambiguous in the mechanism: 1) the state of the silyl ether most strongly electrostatically interacting with the surface, which may or may not have been hydrolyzed by surface water,[63] and 2) the state of the remaining germinal silyl ether linkages after covalent attachment of one silyl ether to the surface, which also may or may not have been hydrolyzed, assuming another surface site is not available. Inclusion of the blocking layer also allows evaluation of the role of a steric obstacle in determining disruption kinetics. More broadly, investigating the surface stability of the alkylsiloxy linkage at three deposition conditions when exposed to base allows us to characterize the bonding landscape of the silica surface. We use single-molecule microscopy because it provides a means of examining surfaces in real time under relevant chemical conditions, recording individual molecular trajectories, and granting both temporal and spatial resolution. Dynamics of molecules at the surface can be assessed, providing a more complete view of the surface's properties.

One motivation for this systematic study of surface-attachment chemistry was the challenge for designing silyl ether-supported catalysts for use in single-molecule investigations. A major difficulty lies in the silyl-ether silica support linkages are known to be susceptible to detachment when exposed to basic conditions. However, silyl ether chemistry is attractive because molecules can be modified with silyl ether appendages relatively easy with all-carbon alkyl linkers as opposed to functional groups, such as triazoles, which would likely interact with transition-metal catalysts. An ideal molecular catalyst for SM studies would have several qualities facilitating single-molecule fluorescence microscopy. The ideal catalyst must be reliably tethered to a surface, and immobilized in the microscope sample plane. The test system must be fluorescently labeled in a way that allows the fluorescence signal to convey information on the catalyst's chemical transitions. Finally, a good catalyst for study would be stable for long periods of time in ambient conditions. For the above reasons, pyridine enhanced precatalyst, preparation, stabilization, and initiation (PEPPSI) palladium catalysts are an attractive target for single-molecule studies. PEPPSI catalysts are employed in a variety of coupling chemistries including Suzuki-Miyaura reactions,[61, 65-67] as well as amination[67, 68] and sulfonylation[69] reactions, due to a combination of superior air and moisture stability[66] and high catalyst activity.[70] PEPPSI catalysts provide a convenient synthetic handle for reliable surface support through the N-heterocyclic carbene[71] and for addition of fluorescent functionality via the labile pyridine ligand.[47] Importantly, as loss of the pyridine ligand must precede formation of the active catalyst,[61] and as the ligand itself has been implicated in the remarkable stability of PEPPSI catalysts,[65] a fluorescent label at this ligand offers the opportunity to explore these important processes at the single-molecule level.

In order to observe initiation of catalyst compound **6** under Suzuki-Miyaura coupling conditions, we conducted wide-field fluorescence microscopy employing an objective-type pseudo-total internal reflectance fluorescence (TIRF) excitation mode. In TIRF, laser excitation is restricted to close proximity to the surface, making our fluorescence measurements highly surface selective.[72] In this experimental configuration (Figure 2-2), BODIPY fluorophores appended to uninitiated catalyst will be fluorescent, while ligands freed during initiation will quickly diffuse out of the excitation volume and no longer emit, making fluorescence a targeted probe of catalyst initiation. By controlling the surface density of catalyst molecules so that we can resolve individual catalysts on the surface, we can gather kinetic information on initiation resolved at the level of single catalyst molecules (Figure 2-2, bottom). Our single-molecule investigations were also corroborated by bulk NMR experiments.

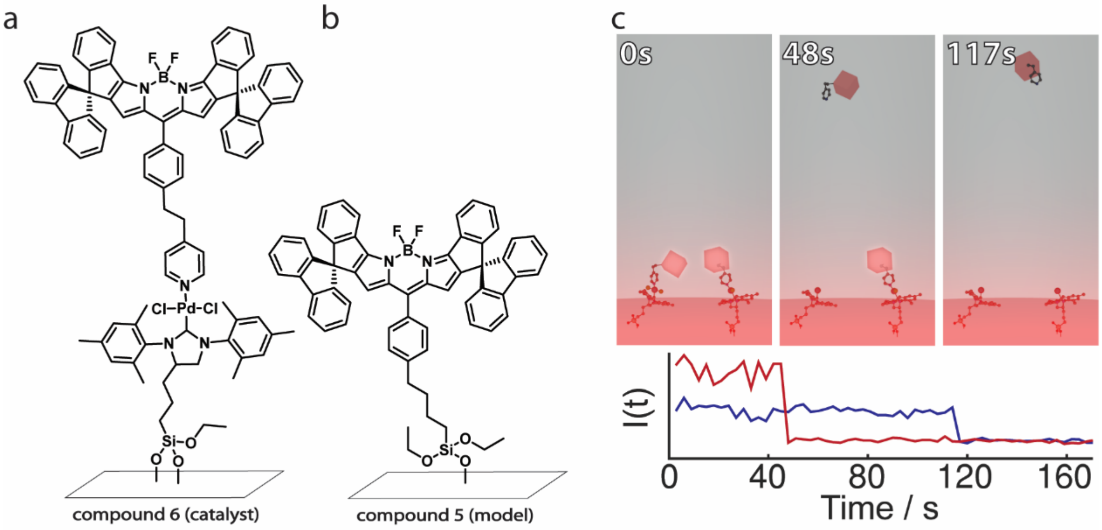

Figure 2-2. Single-molecule investigation of surface-supported molecular catalysts. A surface-supported, BODIPY-labeled catalyst (a), or surface-supported BODIPY model compound (b), is deposited on a glass sample chamber, and viewed on a microscope. Multiple catalyst molecules are observed simultaneously (c, top left). The catalysts fluoresce (c, top) until one initiates, at which time the fluorescent ligand leaves the excitation volume and signal from that catalyst is lost (c, top middle). As multiple catalysts initiate, the fluorescence intensity traces (c, bottom, simulated) from each will show a transition, providing initiation kinetics resolved at the level of individual molecules. The surface anchoring chemistry in a) is shown differently for the two molecules, representing diverse bonding configurations.

2.3 Synthesis of a Surface-Supported Red BODIPY

The control experiments for determining the viability of our surface attachments are effectively performed using a model compound. This model compound consists of the red BODIPY dye directly attached to the glass coverslip (Figure 2-3). This transformation involves attaching a silyl ether to the phenyl ring on the meso position of the red BODIPY. An alkyl spacer exists between the phenyl ring and the silyl ether to 1) aid in the immobilization 2) act as a control for the surface-supported catalyst(s) and 3) disrupt the photophysics of the dye as little as possible.

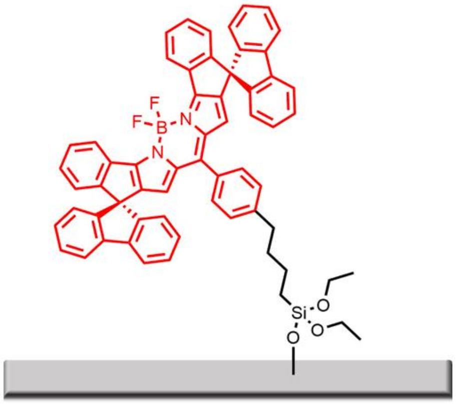

Figure 2-4. Model compound immobilized on a glass coverslip.

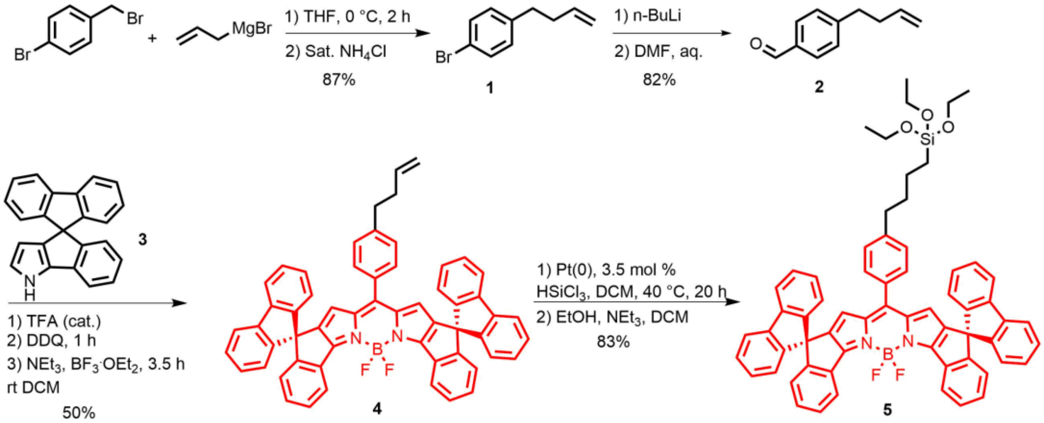

Figure 2-3. Synthesis of silyl-ether functionalized red BODIPY.

The synthesis of the model compound was achieved by first reacting 4-bromobenzyl bromide with allylmagnesium bromide in THF to give compound **1** (Figure 2-4).[73] The next step was a lithium-halogen exchange performed by reaction with *n*-butyllithium and then addition of DMF to furnish the corresponding aldehyde **2** upon aqueous workup. The aldehyde was reacted with the red BODIPY pyrrole **4** to give the terminal alkenyl red BODIPY analogue **4** in standard BODIPY-forming reaction conditions. The final step was a hydrosilylation reaction with Karstedt's catalyst followed by addition of ethanol and triethylamine in dichloromethane.[74] The final step proved to be challenging and was repeated several times before succeeding to afford the silyl ether functionalized model compound **5**. The reason for the success can partially be attributed to the use of a fresh bottle of trichlorosilane (SureSeal® as opposed to standard bottle).

2.4 Qualitative Results

For a more in-depth report of the results, see the original publications.

In our examination of the surface attachment, the addition of high concentrations of KOtBu resulted in a rapid loss of fluorescence, caused by the removal of surface bound molecules from the surface into the bulk solution. As the concentration of KOtBu is decreased, the loss of fluorescence is more gradual indicating that molecules are being removed from the surface less rapidly. In a control experiment, where no base was added, there is still a gradual loss of fluorescence. This is likely caused by hydrolysis because water is not specifically excluded from the experimental setup. However, we also uncovered a trend in which thermal annealing and blocking layers increase the stability of the surface linkage.

While loss of the fluorescently labeled ligand due to catalyst initiation will result in loss of the SM fluorescence signal, other loss mechanisms must also be considered. In order to ascertain the contributions of photobleaching, as well as lysis of the surface anchoring functionality, which could also result in loss of fluorescence, we measured **5**, in which the BODIPY is covalently bound to the surface support with the same anchoring functionality as **6**, under similar conditions to **6**. The median survival times of **5** were found to be 1-2.5 orders of magnitude greater than those of **6**, indicating a significant separation of timescales of catalyst initiation (fast) and combined destruction of the surface support and photobleaching (slow). The mixing time of solution in the sample chamber, blinking of the BODIPY fluorophore, and presence of fluorescent impurities were all considered as possible confounding processes in our experiment and determined to be minor contributors. Consequently, catalyst initiation was viewed as the dominant mechanism of fluorescence loss, and fluorescence loss was used as a proxy for catalyst initiation.

We discovered that the various microenvironments present at the surface influence the isopropoxide base's approach to and interaction with the catalyst metal center, which was reflected in the catalyst behavior, particularly initiation. Critically, though the existence of structural heterogeneity at the surface has been verified by other experimental approaches,[75] our investigation constituted the first direct observation of the effect of the molecular catalyst *structural* heterogeneity on the catalyst *dynamics*. That effect was encapsulated in the increasing spread of rates with increasing concentration of KOtBu. We also developed a saturation model to describe the kinetics we measured.

2.5 Conclusions

From our single-molecule investigation of surface-support degradation at silica surfaces, we found that TOS slows the base-induced destruction of the silica support by creating a non-polar barrier to base attack. We came to the conclusion that the benefit of thermal annealing and blocking layers derives not from an increase in the stability of the surface linkage but from a decrease in the rate at which base molecules approach the surface before irreversible attack at the silyl ether linkage.

We also showed that the observed heterogeneity in kinetics is likely caused by the innate structural diversity of the silica surface. These results suggest that efforts to make silyl-ether constructs at silica interfaces more stable in basic environments should focus on further reducing mass transport of bases through the functional layer to the silica surface.

From our investigation of organometallic catalyst initiation, the initiation kinetics were observed to be highly heterogeneous, grew more heterogeneous with increasing base concentration, and this increasing heterogeneity was shown to be consistent with a saturation model that includes the need to access a limited number of entry sites. That a diversity of microenvironments would yield a corresponding diversity of initiation dynamics was anticipated. The unexpected element is that the apparent diversity *increases* as a function of base concentration. If the heterogeneous dynamics stem from the heterogeneity in microenvironments, then a single underlying structural distribution, largely independent of base concentration, must be capable of yielding increasingly heterogeneous dynamics under different chemical conditions. Said another way, the structural diversity may be nearly constant in all samples, but the dynamics *appear* to be increasingly heterogeneous at high base concentrations, despite likely deriving from the same underlying family of structures.

Population diversity in catalysts has important implications to a wide range of reactions, where inactive subpopulations could significantly slow bulk reaction kinetics. For example, our results indicate that this highly heterogeneous distribution of observed rates at high base concentrations includes a significant population of slow-initiating species, even as the majority initiates quickly. Further study of catalyst initiation could provide insight into causes of catalyst inefficiency and failure by allowing us to create a more detailed model of supported catalyst behavior that includes this diversity.

2.6 Experimental Procedures

2.6.1 Synthetic Procedures

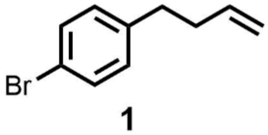

1

1: Compound **1** was synthesized according to a modified literature procedure and its ^{1}H NMR spectrum matched that reported in the literature.[73]

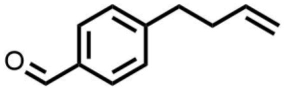

2

2: Compound **2** was synthesized according to a modified literature procedure and its ^{1}H NMR spectrum matched that reported in the literature.[76]

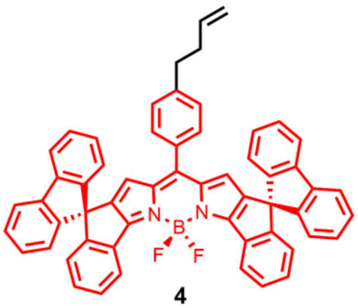

4

4: Compound **4** was synthesized by following a similar procedure to Kowada et al.[55] by charging a in a 100 mL single-neck RBF with aldehyde **2** (100 mg, 0.6 mmol) with pyrrole 1**4** (384 mg, 1.26 mmol) in dichloromethane (15 mL). Next, a catalytic amount of trifluoroacetic acid (TFA, 3 drops) was added and the reaction was stirred at room temperature for 24 hours under N_2. The next day, DDQ (140 mg, 0.66 mmol) was added all at once as a solid and stirred at room temperature for 1 hour. Next, triethylamine (0.25 mL) was added and stirred at room temperature for 30 minutes. Finally, boron trifluoride diethyl etherate (47%, 0.5 mL) was added slowly and stirred at room temperature for 3.5 hours at room temperature. At this time, the solvent was evaporated from the crude reaction mixture and it was purified via column chromatography (1:1 EtOAc/hexanes) to give the pure product (300 mg, 50%). ^{1}H NMR (300 MHz, Chloroform-*d*) δ 7.96 (dt, *J* = 7.6, 0.9 Hz, 2H), 7.77 (dt, *J* = 7.6, 0.9 Hz, 4H), 7.41 (td, *J* = 7.5, 1.1 Hz, 2H), 7.34 (td, *J* = 7.5, 1.1 Hz, 4H), 7.23 (s, 1H), 7.20 – 7.07 (m, 7H), 7.00 (d, *J* = 7.9 Hz, 2H), 6.91 (dt, *J* = 7.6, 0.9 Hz, 4H), 6.61 (dt, *J* = 7.8, 0.9 Hz, 2H), 5.99 (s, 2H), 5.77 (ddt, *J* = 16.8, 10.2, 6.5 Hz, 1H), 5.04 – 4.85 (m, 2H), 2.57 (dd, *J* = 9.3, 6.5 Hz, 2H), 2.25 (q, *J* = 7.1 Hz, 2H). ^{13}C NMR (126 MHz, $CDCl_3$) δ 161.52, 156.67, 148.21, 143.92, 142.97, 142.29, 141.30, 141.09, 137.62, 132.50, 131.65, 130.46, 130.39, 128.74, 128.17, 127.97, 127.92, 124.33, 124.23, 124.18, 120.71, 120.03, 115.14, 59.72, 35.04, 35.02. ESI-MS m/z calculated 798.3127, found 798.3123 $[M+H]^+$

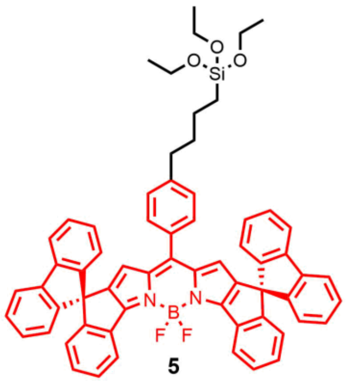

5

5: An oven-dried 25 mL round bottom flask was charged with a solution of **4** (60 mg, 0.75 mmol) in 5 mL dry CH_2Cl_2. Next, Karstedt's catalyst (0.5 mL of a 3.8 % solution of platinum(0)-1,3-divinyl-1,1,3,3-tetramethyldisiloxane complex solution in xylenes) was added to the round bottom flask connected to a condenser through a crack between the condenser and round bottom flask with a strong flow of N_2. Next, trichlorosilane (3 mL) was added in the same manner. The reaction was allowed to reflux overnight. The next day, the solvent was removed using a flow of N_2 (the main purpose is to remove excess trichlorosilane). Next, 5 mL dry CH_2Cl_2 was added and cooled to 0 °C. Then, a 1:1 solution of EtOH/NEt_3 (3 mL) was added via syringe and the solution was stirred for 1.5 hours. The crude mixture was purified via column chromatography (3:7 → 100% EtOAc/hexane) to give the product **4** (50 mg, 83% yield). ^{1}H NMR (300 MHz, Chloroform-*d*) δ 8.75 (d, *J* = 7.7 Hz, 2H), 7.78 (d, *J* = 7.5 Hz, 4H), 7.49 (t, *J* = 7.6 Hz, 2H), 7.35 (t, *J* = 8.0 Hz, 5H), 7.24 (s, 1H), 7.20 – 7.11 (m, 6H), 7.03 (d, *J* = 8.2 Hz, 2H), 6.95 (d, *J* = 7.5 Hz, 4H), 6.62 (d, *J* = 7.6 Hz, 2H), 6.13 (s, 2H), 3.71 (q, *J* = 7.0 Hz, 6H), 2.50 (t, *J* = 7.6 Hz, 2H), 1.11 (t, *J* = 7.0 Hz, 9H), 0.63 – 0.49 (m, 2H). ^{13}C NMR (126 MHz, $CDCl_3$) δ 156.66, 148.83, 144.55, 142.98, 141.43, 133.39, 130.51, 129.99, 128.75, 128.18, 128.00, 125.39, 124.33, 120.12, 119.89, 59.71, 58.41, 35.34, 22.50, 18.37, 10.28, 0.15. ESI-MS m/z calculated 963.02, found 981.3$[M + NH_4]^+$

Chapter 3

3. Mapping Forbidden Emission to Structure in Self-Assembled Organic Nanoparticles

This chapter was published as *J. Am. Chem. Soc.* **2018**, *140* (46), 15827-15841.

3.1 Abstract

The interplay between micromorphology and electronic properties is an important theme in organic electronic materials. Here, we show that a spirofluorene-functionalized boron-dipyrromethene (BODIPY) with an alkyl norbornyl tail self-assembles into nanoparticles with qualitatively different properties as compared to the polymerized species. Further, the nanoparticles exhibit a host of unique emissive properties, including photobrightening, a blue satellite peak, and spectral diffusion. Extensive photophysical characterization, including single-particle imaging and spectroscopy, and time-resolved fluorescence, coupled with electronic structure calculations based on an experimentally determined crystal structure, allow a mechanism to be developed. Specifically, BODIPY chromophores are observed to form quasi-two-dimensional layers, where stacking of unit cells adds either J-aggregate character or H-aggregate character depending on the direction of the stacking. Particularly strongly H-coupled domains show the rare process of emission from an upper exciton state, in violation of Kasha's rule, and result in the blue satellite peak. The spatial heterogeneity of structure thus maps onto a gradient of photophysical behavior as seen in single-particle imaging, and the temporal evolution of structure maps onto fluctuating emissive behavior, as seen in single-particle spectroscopy. Taken together, this system provides a striking example of how physical

structure and electronic properties are intertwined, and a rare opportunity to use one to chart the other.

3.2 Introduction

Synthetic multi-chromophore arrays are versatile nanoscale platforms for controlling and understanding the photophysics of exciton transport. A rich variety of emergent phenomena, including long-range energy transfer,[77, 78] superradiance,[79] unusual scaling laws,[80] and exciton blockades[81, 82] can be observed. Shifting from covalently organized scaffolds to self-assembled systems offers additional opportunities for emergent properties and applications,[83] but also reduces direct control. In particular, small changes in chemical structure may have dramatic effects on morphology, which in turn may have dramatic effects on photophysical behavior.[84,85] For example, with small inter-chromophore distances, balancing interaction strength with the opening of new quenching pathways can be difficult.[86] Similarly, when multiple electronic states are involved, small changes to energetics can result in fundamentally different relaxation and emission mechanisms. This article details the discovery and exploration of a self-assembled chromophore nanoparticle where specific structural motifs of domains within the nanoparticle map onto qualitatively different emissive properties, a rich example of the diversity that can emerge in self-assembled organic materials.

Applications of assembled organic nanomaterials that take advantage of these emergent phenomena range from fluorescence imaging[87, 88] to organic optoelectronic devices[89, 90] (OLEDs, OFETs, molecular electronics) to artificial photosynthesis.[91-93] In biomedical imaging applications, organic nanoparticles have higher *in vivo* compatibility as compared to inorganic nanomaterials.[87] In particular, nanoparticles composed of polymer-bound chromophores (Pdots)[88] have recently been shown to be effective imaging agents. Boron-dipyrromethene (BODIPY) chromophores incorporated into Pdots result in narrow-band emission, a useful feature for multiplexed imaging.[94] In that study,[94] the mole fraction of BODIPY monomers needed to be kept low to avoid self-quenching and spectral broadening, two undesirable aggregation-based processes and vivid examples of the balance required for optimizing properties. A variety of conjugated polymers which contain BODIPY dyes in the main chain have been synthesized and characterized.[95-97] However, polymer scaffolds also present disadvantages, including solubility constraints and difficulty of synthesis.

Here, we present organic nanoparticles derived from self-assembled BODIPY monomers, where the emergent behavior of the self-assembled particle deviates considerably from the polymerized sample. Most conspicuous is a significantly blue-shifted satellite emission peak. Non-uniformities in the brightness and emission spectrum across the particle suggest a non-trivial role of particle morphology. Self-assembled particles were also observed to brighten upon prolonged photoexcitation, a behavior seen in inorganic nanocrystals[98, 99] but previously unobserved in organic nanoparticles. These behaviors were investigated by a combination of steady-state bulk spectroscopy, single-particle microscopy and spectroscopy, time-resolved bulk spectroscopy, structural characterizations, and via electronic structure calculations. Different emission patterns are shown to map onto different structural morphologies which offer different sets of allowed radiative transitions, including the rarely observed phenomenon of emission from an H-aggregated structure. Taken together, our experiments reveal how a simple molecule presents a uniquely rich array of photophysical phenomena that can then be used to illustrate the dominant role of morphology. We expect these themes to be important in optimizing organic nanomaterials for their most promising applications.

3.3 Results

3.3.1 Dye-Labeled Monomer and Polymer

Our target chromophore is a spiro-conjugated BODIPY dye[55] that can be excited with a commercial 633 nm red laser. Using red excitation results in less background fluorescence due to impurities, a feature that has motivated use of this dye in recent single-molecule fluorescence microscopy experiments, where the dye was incorporated as a spectator-fluorophore for monitoring chemical dynamics of individual molecules.[48, 49] This dye also offers the key feature of being rigid, yet non-planar. We had expected this structural property to result in less aggregation, which is often a potential drawback of planar dyes.[100] We incorporated this chromophore into a polymeric scaffold by attaching it to a moiety which would undergo Ring-Opening Metathesis Polymerization (ROMP) (Figure 3-1). By selecting a fast-initiating catalyst, ROMP can be rendered living and, therefore, one can synthesize very well-defined, monodisperse polymers.[101]

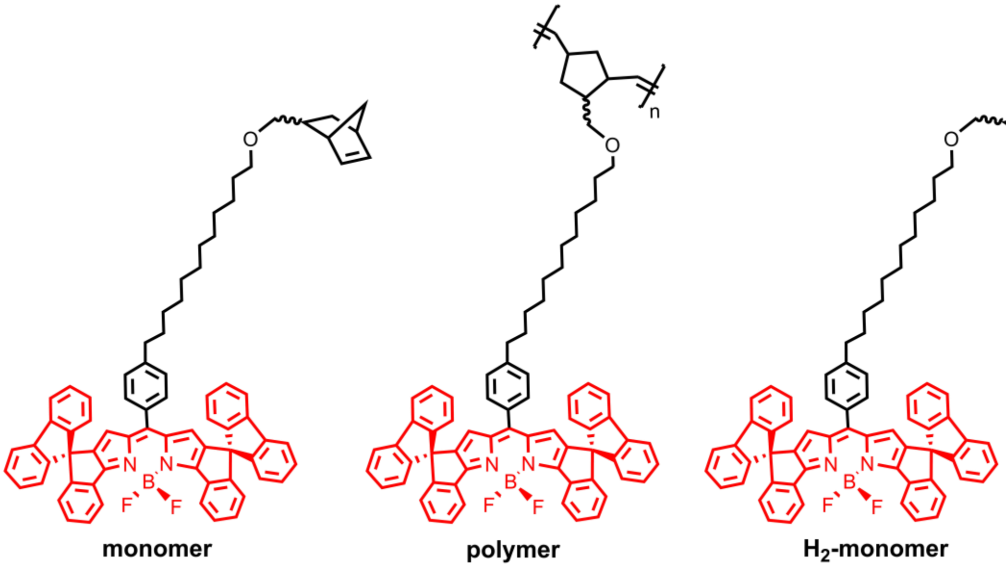

Figure 3-1. Structure of BODIPY-labeled fluorescent norbornene monomer, fluorescent norbornene polymer, and the hydrogenated monomer.

3.3.2 Monomer Synthesis

A common method for synthesizing BODIPY dyes combines an aldehyde and a pyrrole in a one-pot, multi-step reaction.[51, 52] The spiroconjugated pyrrole was synthesized following published procedures.[55] An aldehyde functionalized with a norbornene unit and flexible alkyl chain was synthesized as per Figure 3-2. First, 1,4-dibromobenzene was reacted with *n*-butyllithium followed by addition of 1,12-dibromododecane to obtain compound **7** (Figure 3-2).[102] Next, an O-alkylation was performed to attach 5-norbornene-2-methanol followed by conversion of the aryl bromide **8** to the aryl aldehyde by treatment with *n*-butyllithium and then DMF. Aqueous workup provided aldehyde **9**.

The aldehyde and pyrrole were combined and treated with a catalytic amount of trifluoroacetic acid, followed by dichlorodicyanobenzoquinone (DDQ), then buffering triethylamine and boron trifluoride diethyl etherate to generate the desired BODIPY monomer **10** (Figure 3-1 and Figure 3-2, monomer). The monomer was purified by column chromatography and characterized by ^{1}H-NMR,

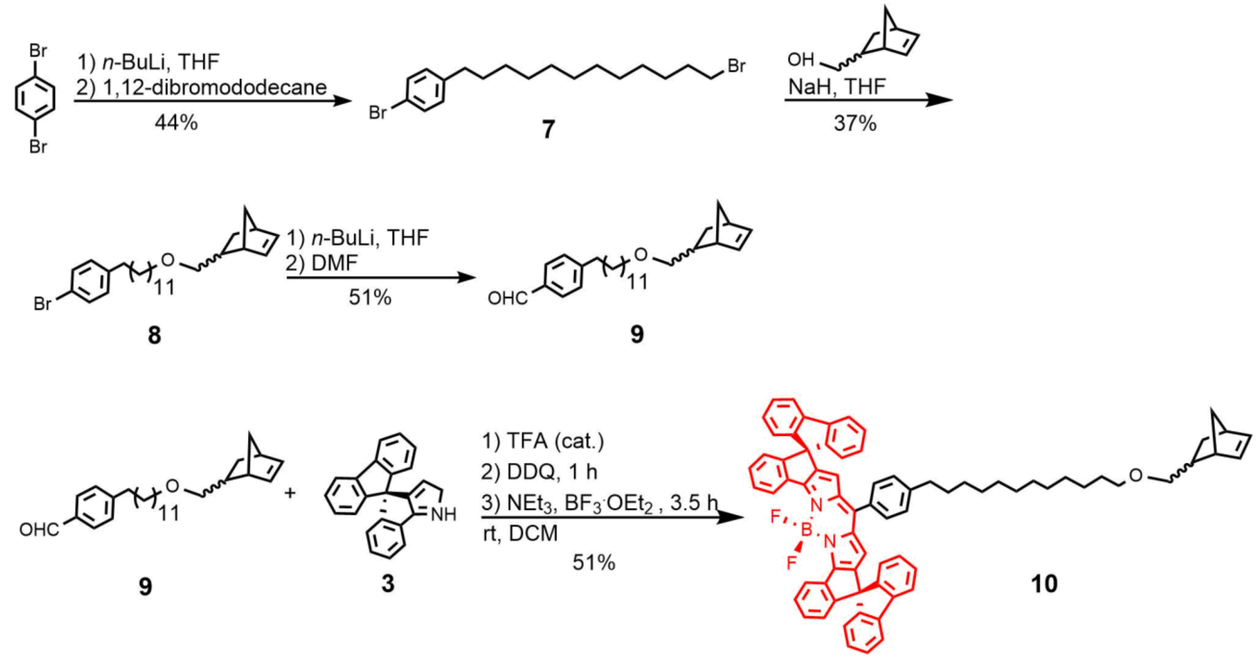

Figure 3-2. Reaction scheme for the synthesis of monomer **10.**

^{13}C-NMR, high-resolution mass-spectrometry, and UV/vis spectroscopy. All synthetic details and characterization data can be found in the Supporting Information.

3.3.3 Polymer Synthesis

Grubbs Generation III catalyst was prepared by reacting Grubbs Generation II catalyst with 3-bromopyridine.[101] Fresh catalyst was then reacted with monomer, resulting in polymer, Figure 3-1, with M_n = 22,240 Daltons (~22 monomer units) as determined by GPC.

Table 1. Molecular weight and polydispersity of BODIPY-norbornene polymer.

Mn (Daltons)	22,240
Mw (Daltons)	38,270
PDI = M_w/M_n	1.721

3.3.4 Solution Phase Absorption and Fluorescence

The monomer and polymer have similar absorption spectra in toluene, with a λ_{max} of 639 nm, and fluorescence emission from the monomer at 643 nm, with polymer emission 120 cm^{-1} redder, at 648 nm (Figure 3-3a). In a 0.1% v/v solution of toluene/isopropanol (IPA), the monomer absorbance and fluorescence blueshift to 634 nm and 639 nm, respectively, while the polymer absorbance develops a red shoulder around 660 nm, with a fluorescence redshift to 665 nm (Figure 3-3b). The shoulder in the absorbance peak of the BODIPY-norbornene polymer in the toluene/IPA solution suggests aggregation of BODIPY units, with the overall red-shift likely indicating chromophores arranged in a J-stacked configuration, but the width of the peak suggests a variety of arrangements spanning H and J aggregates. However, the reduced quantum yield (Table 1) of the polymer in toluene/IPA suggests that there is facile energy transfer to traps that leads to a drastic quenching of the BODIPY fluorescence compared to the monomer in similar conditions.

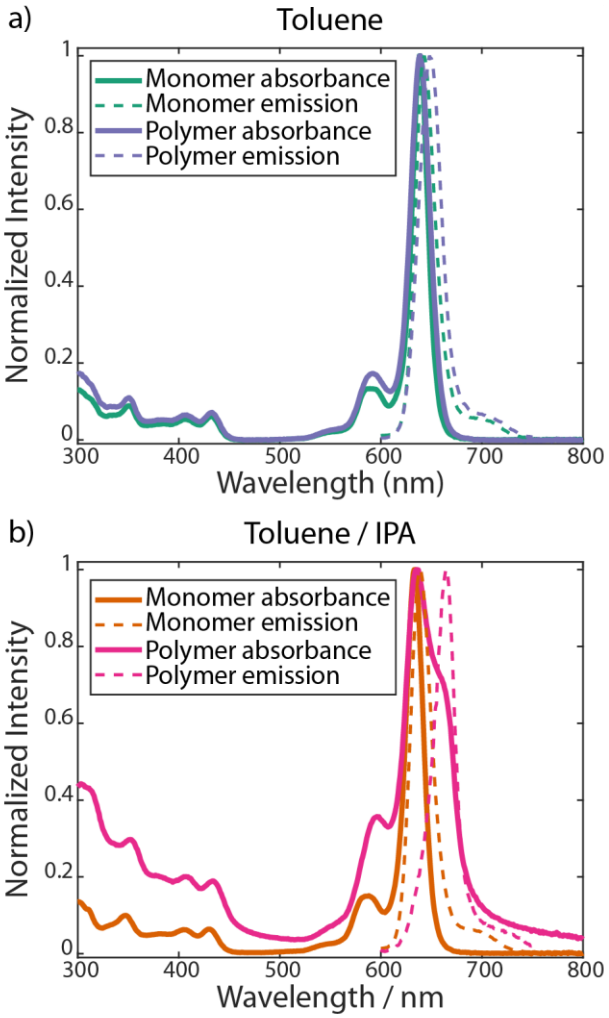

Figure 3-3. Absorbance and Fluorescence Emission spectra of BODIPY monomer and polymer in toluene (a) and 0.1% v/v toluene/IPA mixture (b). Absorbance and fluorescence are normalized to λ_{max}. Fluorescence excitation is at 580 nm. The monomer blueshifts slightly in the mixed solvent, while the polymer absorption broadens and redshifts.

Table 2. BODIPY Quantum Yields

	Monomer	**Polymer**
QY in Toluene	0.55 ± 0.08	0.50 ± 0.07
QY in 0.1% toluene in IPA	0.5 ± 0.1	0.044 ± 0.003

3.3.5 Single-Molecule and Single-Particle Microscopy

Single-molecule spectroscopy and microscopy have a history of providing mechanistic insights into organic materials, including for conjugated polymers,[103-106] multi-chromophore systems,[81, 107-109] and model systems for OLEDs.[110] 5 ng/mL solutions of **monomer** and **polymer** were spin-coated from toluene onto glass coverslips as well-separated nano-objects, Figure 3-4a. Monomers and polymers showed single-step photobleaching and blinking behavior, Figure 3-5. While single-step bleaching is typical of individual fluorophores, such behavior in polymers suggests a well-coupled multi-chromophore system.[81, 111] Further, even when polymer molecules are in their most emissive state, their intensities are comparable to the intensities exhibited by the monomers (Figure 3-5), despite an average polymer size near 22 monomers. Thus, a potent quenching mechanism must be operative in order to not have increased brightness despite the increased number of fluorophores. Since the quantum yield of monomers and polymers in toluene is similar as determined via the solution-phase steady-state spectroscopy (Table 2), these quenching mechanisms are only operative in the single-particle measurement, either because of the absence of solvent, presence of the surface, or higher excitation intensities which may result in saturation effects.[47]

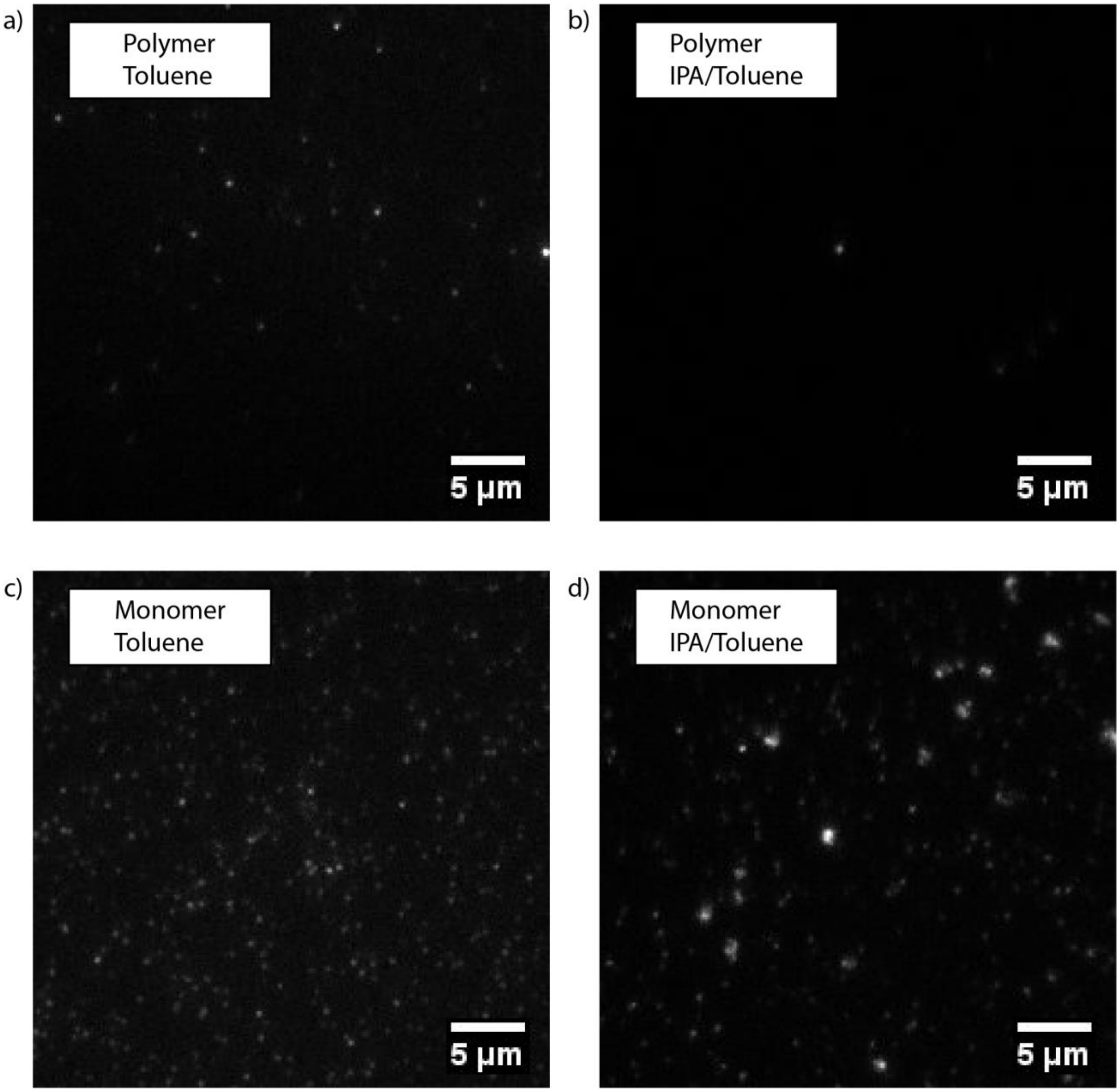

Figure 3-4. Samples of polymer and monomer spin-coated from 5 ng/mL solutions, excited at 633 nm at an intensity of 25 W/cm^2 and imaged with a 30 ms exposure time. Polymer spin-coated from toluene (a) and 0.1 % v/v toluene/IPA (b) deposited as a sparse coating of particles of similar brightness. Monomer spin-coated toluene (c) deposited as a more densely populated layer, with similar brightness. Monomer deposited from 0.1 % v/v toluene/IPA (d) densely covers the surface, and is significantly brighter. All images displayed with similar brightness and contrast.

A growing body of research has demonstrated the importance of solvents in shaping the morphology (and therefore, bulk properties) of organic materials including in individual conjugated polymer chains.[105, 106, 112-114] For instance, solvent vapor annealing (SVA) has been used as a post-processing method to change film morphology, and these changes have been systematically examined at the single-polymer level.[106] Large differences in aggregation propensity were observed between solvent systems of disparate polarity.[106] For our work, in order to test the effect of changing the deposition solvent on our polymer photophysics, we made a 5 ng/mL solution of polymer in 0.1% vol/vol toluene/isopropanol (IPA) by diluting the toluene stock in IPA. The **polymer** samples spin-coated from the polar solvent mixture show discrete intensity levels of similar brightness to those spin-coated from pure toluene at this low concentration, but with a lower surface density (Figure 3-4a,b). While Table 2 reports quantum yields of similar value for **monomer** and **polymer** in toluene, in toluene/IPA the quantum yield of the **polymer** is significantly decreased, whereas the solution-phase **monomer** quantum yield is largely unaltered. Thus, whereas the quenching of the **polymer** relative to the monomer in toluene is not seen in solution and is only seen in the single-particle measurement, in toluene/IPA the **polymer** is quenched relative to the **monomer** in both solution and in the single-particle measurement, suggesting that quenching mechanisms, including formation of aggregates with H character, are operational in solution and at the surface.

Surprisingly, the monomer spin-coated at 5 ng/mL from a toluene/IPA mixture shows individual nano-objects with significantly increased fluorescence intensity compared to both the monomer deposited from toluene and the polymer deposited from toluene/IPA (Figure 3-5). Emission from these nano-objects does not show blinking or single-step photobleaching, suggesting that monomers deposit as aggregates under these deposition conditions, and that the aggregation does not result in quenching, a sharp contrast to the behavior exhibited by the polymers that show emission intensity comparable to isolated monomers.

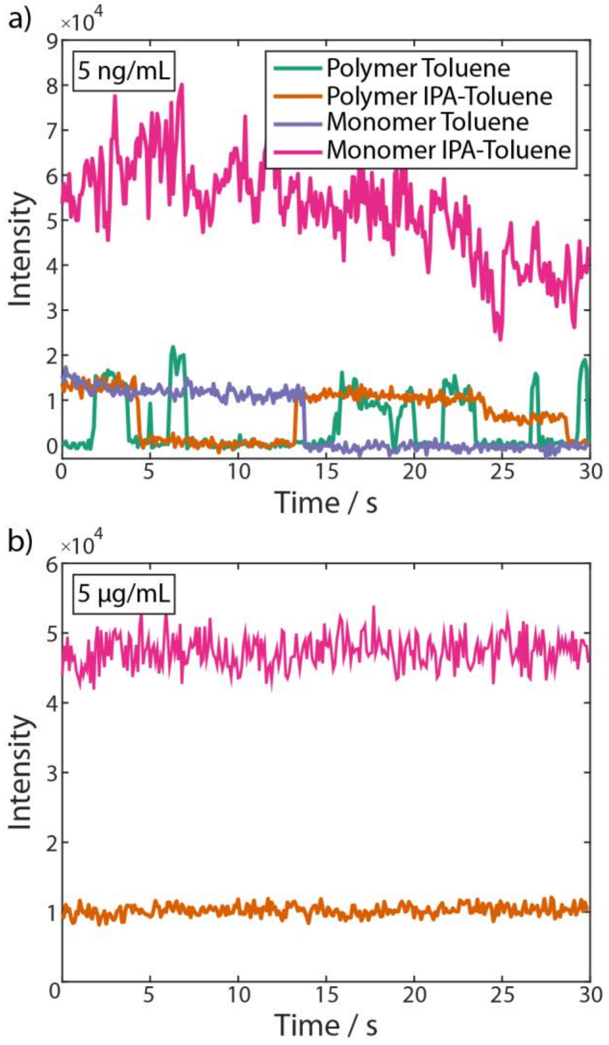

Figure 3-5. Single Particle Trajectories from 5 ng/mL videos (a) and 5 µg/mL videos (b) depicted in figures 4 and 6. ng/mL traces taken at 28 W/cm^2, 30 ms exposure time. µg/mL traces taken at 280 mW/cm^2, 10 ms exposure time. At 5 ng/mL particles blink, indicating fluorescence from a single or small number of molecules, and have similar brightness, under all conditions except for **monomer** spin-coated from 0.1 % toluene/IPA. At 5 µg/mL, **monomer** nanoparticles act as a large number of emitters, without blinking.

Increasing the deposition concentration of the toluene solutions of both monomer and polymer to 5 µg/mL increases the surface coverage, leading to the formation of a thin film (see original publication). Depositing monomer from 0.1% v/v toluene/IPA solvent mixture at 5 µg/mL results in bright fluorescent particles which are still clearly spatially resolved, with surface densities comparable to the 5 ng/mL deposition condition (Figure 3-6b), but the individual particles are substantially brighter. Adjusting for different imaging conditions, these new particles are 400 times brighter than at the lower concentration (see original publication). Polymers deposited from these conditions are also brighter (Figure 3-6a) and also show sustained emission without blinking or

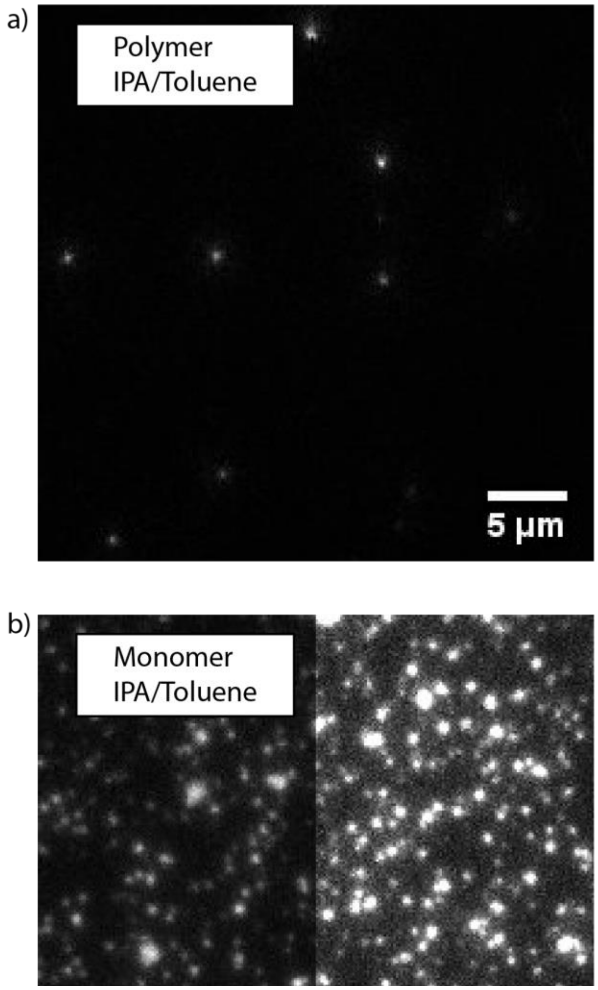

Figure 3-6. Samples of **polymer** and **monomer** spin-coated from 5 µg/mL solutions, excited at 633 nm at an intensity of 0.25 W/cm^2 and imaged with a 10 ms exposure time. **Polymer** deposited from 0.1 % toluene/IPA still sparsely covers the surface (a), and **monomer** deposited from the mixed solvent (b) is still a dense layer of isolated spots, much brighter than samples prepared at 5 ng/mL. (b, right) is displayed under similar brightness/contrast settings to (a) while (b, left) is rescaled to avoid saturation.

photobleaching (Figure 3-5b), in contrast to the more dilute deposition conditions where blinking was prevalent. However, polymer particles were still substantially dimmer than monomer particles.

3.3.6 Photobrightening

When excited near their absorption maximum at 633 nm, the emission from bright aggregated **monomer** nanoparticles is largely constant over minutes, with slow photobleaching (Figure 3-7, red). However, when excited at 532 nm, surprisingly, the aggregated **monomer** nanoparticles show increasing fluorescence intensity over time (Figure 3-7, light green and dark green). Fluorescence

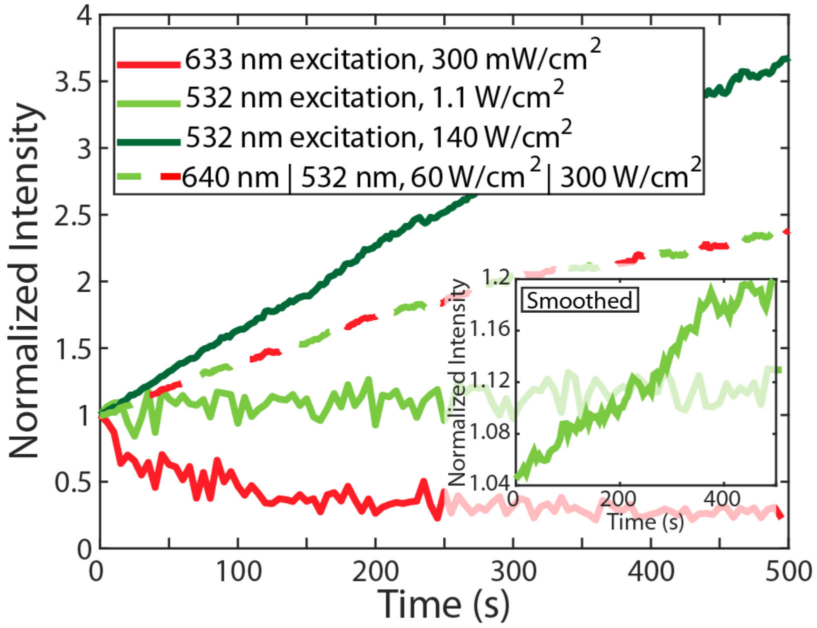

Figure 3-7. Fluorescence intensity trajectories of monomer particles excited at 633 nm (red) and 532 nm (greens). The particles increase in fluorescence intensity by more than 250% over 500 seconds when they are excited by green light at 140 W/cm^2 (dark green), and more subtly when excited with 1 W/cm^2 (light green) but bleach normally when excited by red light at 0.3 W/cm^2 (red). When alternately excited at 532 nm and 640 nm, the emission from 640 nm excitation increased over time instead of bleaching (red/green dashed trace). Smoothing and rescaling of the 532 nm, 1.1 W/ cm^2 trajectory highlights the subtle increase in intensity over time (Inset, light green).

intensity of particles spin-coated at 6 μg/mL increased by over 250% over 500 seconds when excited at high excitation intensity (Figure 3-7, dark green), before eventually photobleaching. While the

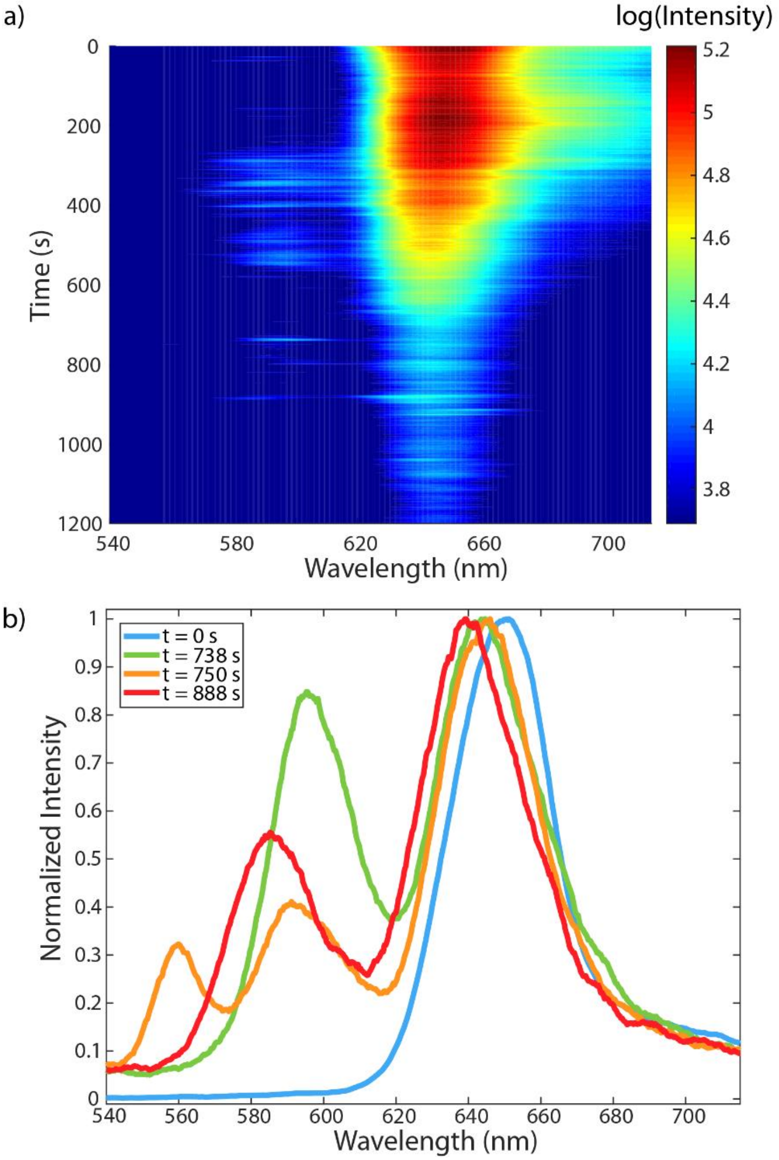

Figure 3-8. Spectra of a single monomer particle spin-coated from toluene-IPA mixture over time (a), and selected normalized spectra at several time points chosen to highlight emission from the blue satellite (b). The monomer nanoparticle shows an increase in fluorescence intensity before bleaching. Spectrally, the S_1 emission near 640 nm blue-shifts a small amount over time, and the relative intensity of the satellite peak increases largely due to bleaching of S_1 fluorescence after ~700 s. The wavelength of the blue satellite is mostly centered at 590 nm (green), but occasionally spontaneously shifts to 580 nm (red), and extremely rarely displays a third even higher energy peak (orange). Spectra are smoothed with a moving mean of width ~7 nm. CW excitation is provided at 532 nm at 690 W/cm^2.

degree of brightening was variable, increasing emission over time was consistently observed. **Polymer** samples under similar conditions exhibited the typically observed slow photobleaching, without the period of increasing fluorescence (see original publication), indicating that the photobrightening behavior is unique to the aggregated **monomer**.

Photobrightening with excitation at 532 nm can occur if a population is being irreversibly converted to a new photoproduct with stronger 532 nm absorption and emission, which would result in decreased emission from the original red species. To test for this possibility, we used alternating excitation between 532 nm and 640 nm light (Figure 3-7, dashed red and green) with emission spectrally resolved into two channels separated by a 650 nm dichroic mirror. Though the brightening was uniquely driven by excitation at 532 nm light, the emission intensity increased whether the sample was excited by green or red light, contradicting the hypothesis of a new photoproduct described above. To better understand these unexpected photophysics, we further characterized particles formed from **monomer** deposited at 5-6 μg/mL. All further characterization was applied to these high-concentration monomer-derived nanoparticles unless otherwise mentioned.

3.3.7 Single-Particle Spectroscopy

To further explore the physical transition that occurs during photobrightening, emission spectra of single particles were acquired as a function of time. Single-particle spectra of one representative **monomer** nanoparticle excited at 532 nm shows a broad peak centered at 650 nm likely originating from S_1 emission, with an unexpected blue satellite peak which blinks on and off and diffuses spectrally, ranging from 550-600 nm, Figure 3-8. A trivial source of dual emission could be the presence of a fluorescent impurity in the **monomer**. However, an excitation spectrum of **monomer** in solution measuring emission at the emission maximum contains all the absorption features of the solution spectrum, ruling out a chemical impurity (see original publication). The major and minor solution-phase absorption and emission peaks do not follow the mirror image relationship expected of a vibronic progression, and the minor fluorescence peak is higher in energy than the major solution-phase absorption peak. Therefore, an additional mechanism that allows for radiation from higher electronic or excitonic species must be at play, in violation of Kasha's rule.[86]

3.3.8 Spectrally Resolved Imaging

Seeing the above evidence of spectral heterogeneity, we added a degree of spectral decomposition to our single-particle imagine by resolving the image into blue (560 nm – 590 nm) and red (660 nm – 720 nm) emission channels (Figure 3-9). When imaging small particles, no significant spatial differences were seen in the two color channels (though blue satellite emission was weaker as expected, see original publication), likely to due to the sub-diffraction limited particle size. However, spectrally decom-posed imaging when applied to large (~1 μm) particles showed a qualitatively different behavior. Surprisingly, while the red-channel emission from large monomer particles took the commonly observed form of homogenous circular puncta (spots), emission in the spectral channel that includes the blue satellite appears as rings of fluorescence, Figure 3-9a. Prolonged excitation at 532 nm results in a collapse of the ring to a circular punctum, easily visible in sequential images (Figure 3-10a) or movies (see original publication). Observation of rings only occurred in large aggregates, with the size of the aggregate depending sensitively on the deposition conditions including sample concentration and sample history. In contrast, the observation of photobrightening (Figure 3-7) was very robust to various sample preparation conditions.

3.4 Discussion

Norbornene functionalized BODIPY **monomer** and **polymer** were synthesized and compared. **Polymer** showed significant quenching in solution due to the close proximity of the

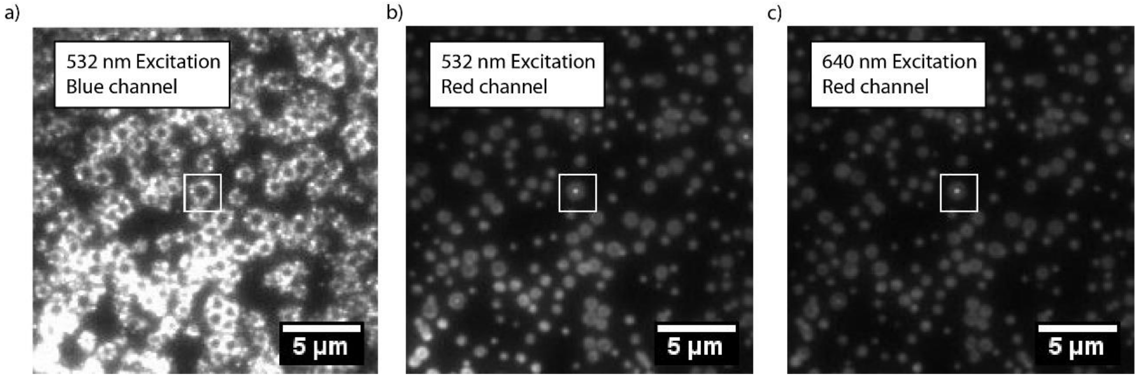

Figure 3-9. Images of large particles spectrally decomposed into blue (a, 560-590 nm) and red (b and c, 660-720 nm) channels with 532 nm excitation (a and b), or 640 nm excitation (c). All images set to the same brightness and contrast settings. Samples were excited at an intensity of 300 W/cm^2 at 532 nm, and 60 W/cm^2 at 640 nm. The particle used in Fig 3-10 is boxed in the center of the images.

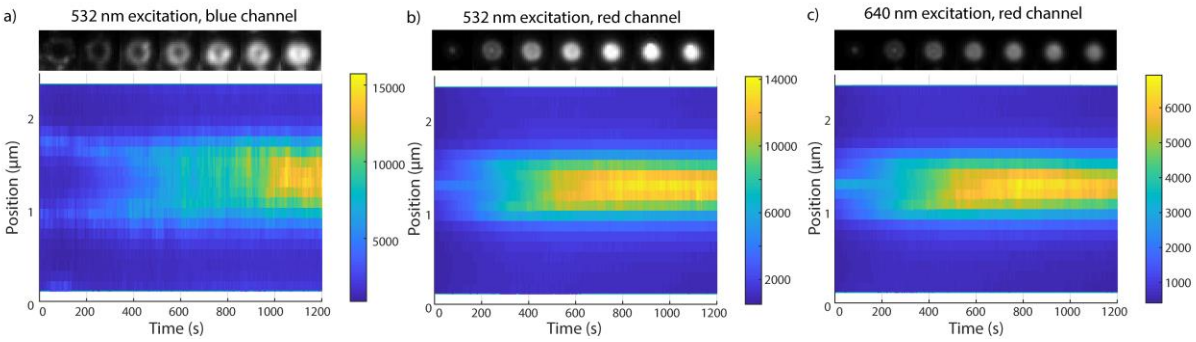

Figure 3-10. Waterfall plots of large monomer nanoparticle emission intensity under alternating excitation. Single monomer particle excited by alternating 532 nm (a,b) and 640 nm (c) laser light shows increasing fluorescence intensity in both the blue (a, 560-590 nm) and red (b, c, 660-720 nm) channels. Plots show fluorescence intensity of a line profile through a single particle (*y*) over time (*x*), with 2 second resolution. Over time, the particles become brighter in all channels, while remaining a similar size. The blue channel signal with 532 nm excitation shows initial fluorescence from a ring around the perimeter of the particle, which becomes more intense and fills in the center of the particle over time (a). Red channel fluorescence is concentrated inside the blue-channel fluorescent ring, is similarly localized in both excitation channels, and also increases over time.

pendant BODIPYs. The **monomer**, when spin-coated from a poor polar solvent mixture forms nanoparticles. Surprisingly, bright **monomer** nanoparticles fluoresce with in-creasing intensity as they are excited at 532 nm, and exhibit a blue satellite peak at 550-600 nm in addition to the typical S$_1$ emission near 650 nm, in violation of Kasha's rule. For large particles, the blue satellite peak occurs uniquely at the exterior rim of the particle while being absent at the particle centers, with a shifting spatial distribution over time. The intensity, spectral, and spatial changes in emission over time suggest a change in chemical structure or morphology of the nanoparticle aggregate.

Most organic fluorophores will eventually become oxidized to a non-fluorescent state after repeated photoexcitation, with a large collection of non-interacting fluorophores displaying an analog decrease in fluorescence intensity. Alternatively, emission can be increased over time if that emission is initially partially quenched by an energy acceptor that is subsequently eliminated. Indeed, increasing Förster Resonance Energy Transfer (FRET) donor emission has been observed in FRET microscopy due to bleaching of an acceptor dye.[115, 116] PbS[98] and CdSe[99] quantum dots have also been shown to brighten controllably under irradiation in a process due to filling of surface electron-trap sites. The validity of these mechanisms and others will be considered below for our system.

3.4.1 Ruling out a Chemical Mechanism

Nanoparticle photobrightening could derive from a chemical reaction, such as the result of an intra- or inter-molecular photocycloaddition reaction involving the norbornene alkene moiety and the BODIPY. The double bond in the strained ring system of norbornene is well-known for its high reactivity.[117, 118] Additionally, norbornene is known to participate in visible light-mediated photocycloaddition reactions under mild conditions.[119] A new chemical species produced from such a reaction could have different photophysical properties and, therefore, be responsible for the observed photobrightening behavior. In order to rule this out, we hydrogenated the BODIPY monomer using palladium on carbon and hydrogen at atmospheric pressure yielding **H_2-monomer (11)**, (Figure 3-1). **H_2-monomer** displayed the same behavior as the parent monomer when analyzed at the single-particle level (see original publication). Therefore, we can confidently rule out any chemical behavior due to alkene reactivity of the norbornene moiety. The norbornene/norbornane moiety appears to function primarily as a morphology-directing group.

3.4.2 Photobrightening Results from a Photothermal Mechanism

Photobrightening only occurred upon excitation at 532 nm, while excitation at 633 nm produced continuous emission at a slowly decreasing intensity due to photobleaching, Figure 3-7. While excitation with higher energy 532 nm photons could access a higher electronic or vibronic state with a different photophysical fate, it much more commonly results in the same emission with a larger fraction of the input energy dissipated as heat (Kasha's Rule). That dissipated heat could result in morphological changes that could affect the apparent brightness. However, if a photothermal mechanism is responsible, external heating should also have an effect on emission properties. Heating

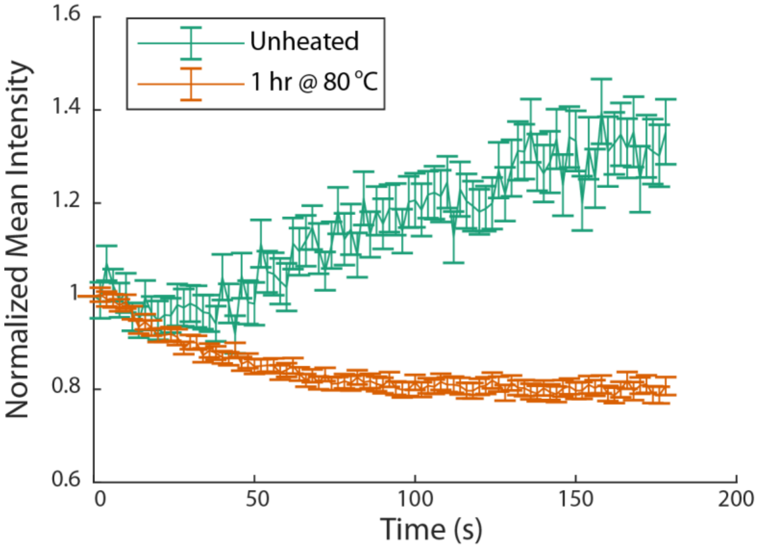

Figure 3-11. Summed intensity trajectories of many monomer nanoparticles upon 532 nm excitation as spin-coated (green) or after being pre-heated at 80 °C for 1 hour (orange), normalized to initial intensity. Pre-heated samples are brighter (see SI of original publication) and do not continue to photobrighten, suggesting that the brightening mechanism is photothermal in nature.

spin-coated monomer nanoparticle samples on a hotplate at 80 °C led to an increased initial fluorescence intensity (see original publication) and an absence of photobrightening after thermal annealing (Figure 3-11). The fluorescence intensity integrated over 200 s increases by a factor of 5 after 3 hours of heating (see original publication). After heating, the photobrightening effect vanishes, Figure 3-11. Because the photobrightening effects are mimicked by thermal annealing, the increased fluorescence over time is likely due to a photothermal mechanism, such as evaporation of solvent or thermal rearrangements of the dye molecules, leading to changes in the internal structure of the particles.

3.4.3 Assessing Structure and Morphology of Nanoparticles

Before delving into the unique optical phenomena, it is desirable to learn more about the dimensions and molecular packing of the self-assembled dye aggregates.

Atomic Force Microscopy (AFM) images were acquired (see original publication). Monomer spin-coated onto glass from a 5 μg/mL 0.1% toluene/IPA mixture shows aggregation into well-separated nanoparticles 160 ± 30 nm in diameter and 14 ± 5 nm tall, with a surface density of 0.3 ± 0.1 / μm^2. These conditions produce particles similar to those in Figure 6 as opposed to Figure 3-9.

To obtain more insight into the relative orientation of the BODIPY chromophores in the aggregates as directed by the norbornene tail, crystals of monomer were grown via slow diffusion ($CHCl_3$/CH_3CN) at room temperature for 72 hours. The single-crystal X-ray diffraction (XRD) data was suitable for drawing basic conclusions regarding the relative orientation of the monomer BODIPY moieties (Figure 3-12), but not well-resolved enough to locate atoms within the alkyl chain or determine exact bond lengths and distances. The N–N vector within each BODIPY core is approximately parallel to the *a* axis, Figure 3-12a. The BODIPY units form corrugated sheets parallel to the *ac* plane, Figure 3-12b. These ~18.7 Å thick layers are separated along the *b* axis by ~27.8 Å (roughly the length of the extended alkyl chain). We suspect that these alkyl chains are extending along the *b* axis between the BODIPY layers. Likely, the BODIPY core units have a propensity to stack with one another into a somewhat organized structure largely due to solvent interactions while the long alkyl chains remain highly disordered. The balance between π stacking interactions, steric repulsions from the spirofluorene groups, and segregation of disordered aliphatic chains is likely responsible for the quasi-two-dimensional BODIPY packing.

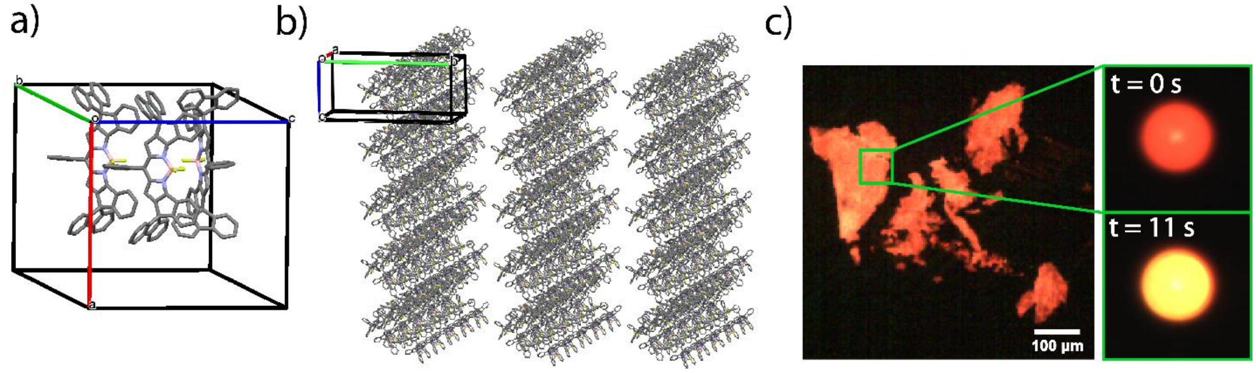

Figure 3-12. Crystal structure and photobrightening of crystals. a) View of the unit cell, showing three symmetry-independent BODIPY molecules, with cores oriented so that the N–N vectors are approximately parallel to the *a* axis. Color scheme: grey C, blue N, orange B, green F. b) A molecular packing diagram illustrating the existence of quasi-two-dimensional sheets. Alkyl chains are not shown. c) Individual crystals fluoresce red upon widefield excitation. Upon prolonged excitation with a more focused beam (diameter ~150 μm), intense red emission is observed, followed by yellow emission (insets).

3.4.4 Coupling between Morphology and Electronic Structure

The crystal structure presented in Figure 3-12 provides a basis to formulate a model for the electronic structure of BODIPY aggregates that underlies the rich set of optical measurements presented above.

Simulated spectra of molecular aggregates were prepared as follows. First, electronic excitation spectra, transition dipoles, and transition densities of single BODIPY molecules were calculated using time-dependent density functional theory (see original publication). The lowest optically allowed electronic excitation is at 2.34 eV (530 nm) with the corresponding transition dipole about 10 D. The second optically active transition is at 3.4eV (360 nm), which leaves an optically "dark" window of about 1 eV and allows consideration of only the lowest intramolecular transitions in the formation of

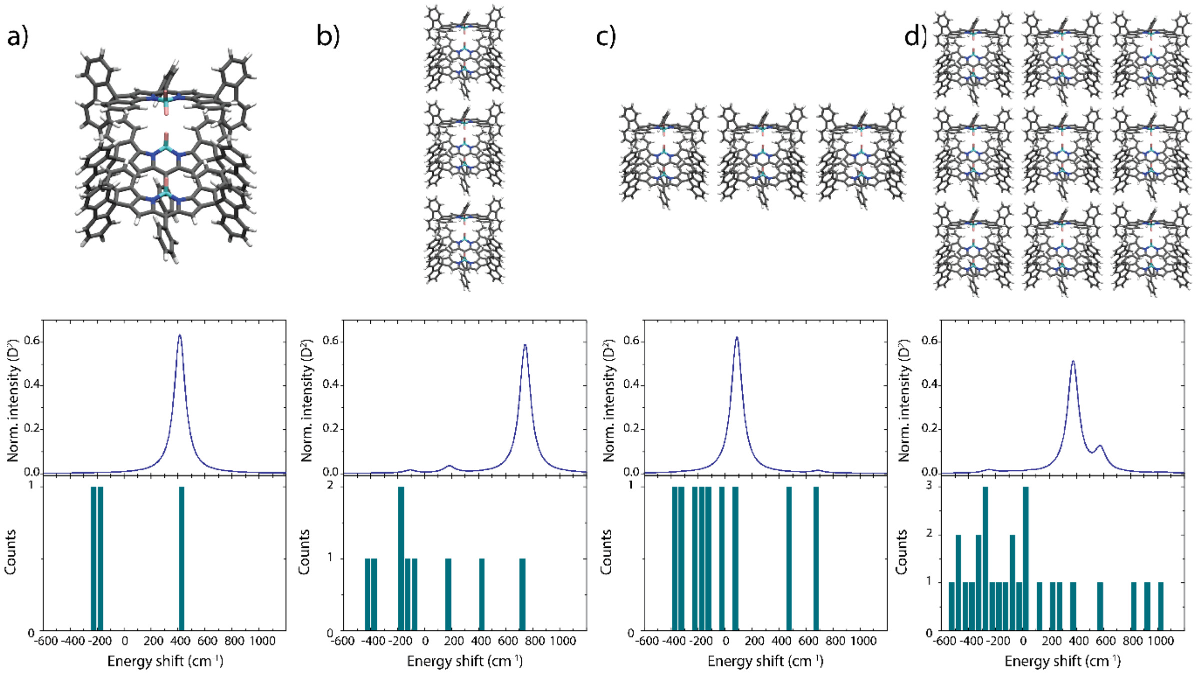

Figure 3-13. Calculations on packing structures. Correlation between unit cell packing (top), predicted spectra (middle) and density of states (DOS, bottom) for a) a single unit cell, b) a 1x3 unit cell aggregate, c) a 3x1 unit cell aggregate, and d) a 3x3 unit cell aggregate of **monomer**.

collective excitonic states in the BODIPY aggregates. The collective excitonic states in the molecular aggregates are formed due to the Förster interaction between intramolecular excitations.[120] Frequently, to reduce the computational cost, this interaction is modeled using a multipole fit to microscopic models.[121] Here, we follow a different route and compute the intermolecular couplings directly from the transition densities. Spectra of small BODIPY aggregates are singly or doubly peaked with spectral position and density of states (DOS) highly sensitive to the shape of the aggregate, Figure 3-13.

Thus, the unit cell is an H-aggregate with a dipole-allowed upper exciton band shifted 400 cm^{-1} blue of the isolated monomer while dipole forbidden states exist around -200 and -250 cm^{-1}, and thus there is a 650 cm^{-1} splitting be-tween the dipole allowed state and the next lowest state, Figure 3-13a. However, the nature of the interaction of the unit cell with other unit cells varies significantly depending on crystallographic orientation. As shown in Figure 3-12b, the BODIPY cores assemble in quasi-two-dimensional layers, with aliphatic chains largely insulating the BODIPY layers from each other. Figure 3-13b-d shows how the exciton coupling varies as unit cells are expanded along the remaining two crystallographic axes. Expansion along the *c* axis (Figure 3-13b) results in an additional blue shift, resulting in even more H character and a splitting between upper and lower exciton bands near 1000 cm^{-1} for a trimer. In contrast, expansion along the *a* axis (Figure 3-13c) results in red shift, opposing the H character within the unit cell, resulting in a net J aggregate character. Creation of a full two-dimensional layer, Figure 3-13d, results in a dominant dipole-allowed transition net negligibly shifted from the isolated monomer, suggesting that interactions in the two crystallographic directions largely oppose each other in the ideal geometry. Extension of this effect to higher order aggregates, Figure 3-14, shows a saturation of the effect by ten unit cell repeats, with one dimensional structures along the *c* axis showing a splitting between upper and lower exciton bands just exceeding 1000 cm^{-1}.

This ideal geometry does not include the significant amount of disorder present in the aggregates, though it does provide a mechanism for how the geometry of different shaped nanodomains maps onto electronic structure. The smallest domains likely resemble a single or small number of unit cells, and thus a net H-character domain. Domains with eccentricity along one direction are then predicted to range from having strong H-character to weak J-character. Thus, fracturing the ideal two-dimensional array into nanodomains predicts a heterogeneous mixture of electronic state distributions, Figure 3-15a.

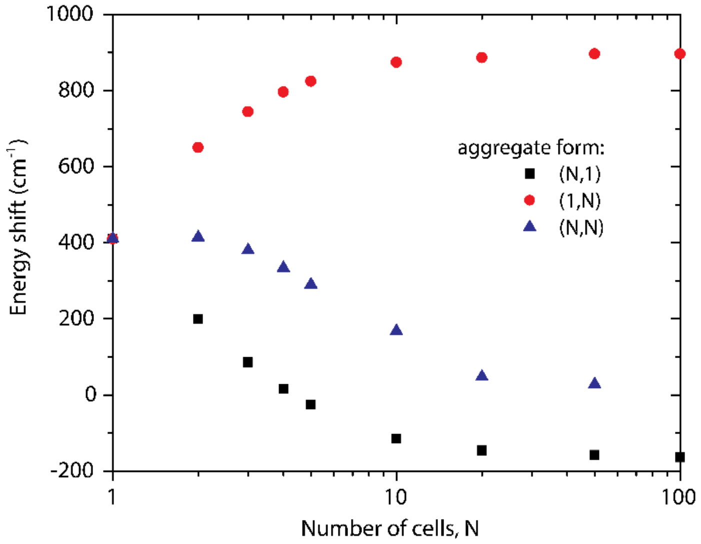

Figure 3-14. Relationship between energy shift and aggregate size. Energy shift of emissive band relative to the isolated monomer in 1D (black and red) and 2D (blue) aggregates of increasing number of unit cells (N). The (1,3) data point corresponds with Figure 3-13b and the (3,1) data point corresponds with Figure 3-13c.

It is also important to emphasize that the single crystal structure is one of many possible geometries that may exist in the nanoparticle. For example, films made via dropcasting that are suitable for thin-film XRD show broad features (see original publication) indicative of many contributing structures. These films do not show evidence of photobrightening or satellite emission, suggesting that the special geometries required for these phenomena exist in the nanoparticles but not in the thin film. On the other hand, the individual crystals used for the crystal structure shown in Figure 3-12a show photophysical behavior qualitatively similar to the nanoparticles. Upon illumination at 532 nm, individual crystals first show red emission but then show yellow emission (~560-590 nm) upon prolonged excitation, Figure 3-12c. Thus, molecules packed in this geometry also show the appearance of a blue-shifted spectral feature, suggesting that it is reasonable to use the determined crystal structure to understand the behavior of the nanoparticles. Photobrightening was also observed, but inconsistently as photobleaching was also quite rapid. Importantly, even as the crystal structure can provide a basis for the photophysical observations in the nanoparticles, it should be taken as one piece of evidence that a particular molecular ordering motif exists that can provide both H- and J- character. Other molecular packing geometries are also possible.

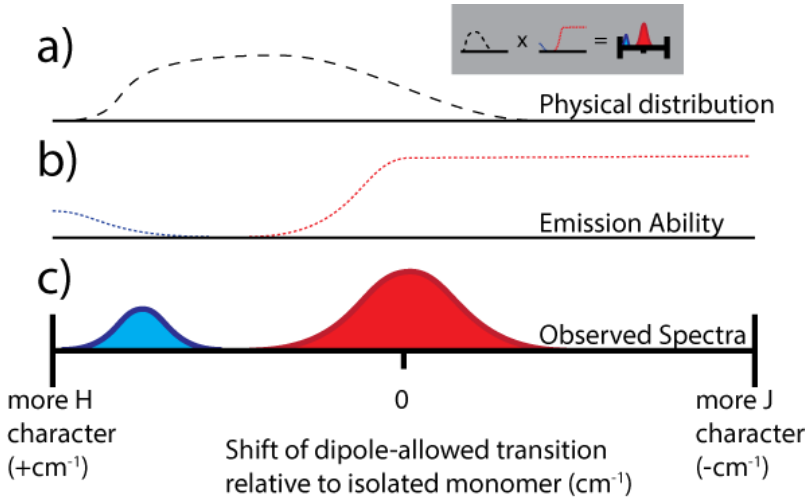

Figure 3-15. Summary of expected emissive properties. a) Samples of monomer aggregates display a range of exciton coupling behaviors, ranging from weak J-aggregates to strong H-aggregates. b) J- aggregates are expected to demonstrate red emission slightly or significantly red-shifted from the unaggregated monomer depending on the strength of the J-coupling. In contrast, weakly H-aggregated species should be non-emissive, and strongly coupled H-aggregates may display weak blue-shifted emission. c) Taking into consideration the expected distribution of electronic structures and different emissive behaviors, this model predicts a major peak near the unaggregated monomer and a weaker blue satellite peak, as observed.

3.4.5 Mapping Electronic Structure onto Emissive Properties and Time-Resolved Emission

The final piece then is using the model of electronic structure above to predict emission behavior, Figure 3-16. Strongly J-coupled aggregates are expected to result in red-shifted fluorescence enhanced in intensity due to a transition dipole distributed across multiple molecules (i.e., superradiance).[122] However, as predicted above, due to the H-coupling within the unit cell, even the most favorable assemblies for generating J-coupling should only result in a weakly J-coupled aggregate, suggesting such strong red-shifted emission should not be seen, as is born out in experiments, Figure 3-8.

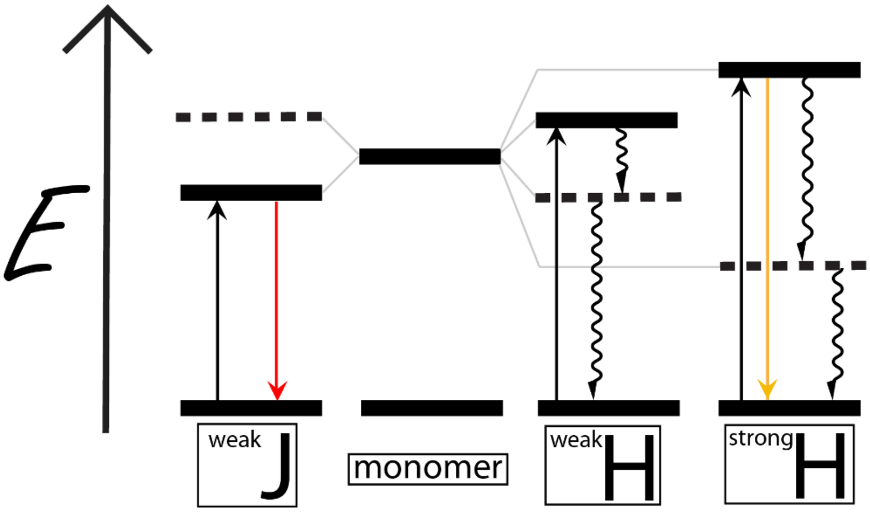

Figure 3-16. Jablonski Diagram, showing emissive properties of observed aggregates. Weakly J-coupled aggregates are expected to demonstrate red emission, similar to the solution-phase monomer. Weakly H-coupled aggregates are expected to be non-emissive due to rapid internal conversion to the non-emissive lower exciton level. Strongly H-coupled aggregates will possess a large energetic splitting between the upper and lower exciton bands that will slow internal conversion, allowing weak emission from the upper exciton state, observable as emitted orange (near 580 nm) light, which is referred to as the "blue satellite" peak.

Weakly H- or J-coupled species should present with emission that is similar to the isolated monomer. The diagnostic feature of a distribution of weakly exciton-coupled species should be a broad emission peak centered close to the isolated monomer emission, as seen in experiments, Figure 3-8.

The most exotic observation in our experiments is the blue-shifted satellite peaks, Figure 3-8. H-aggregates result in blue-shifted dipole-allowed transitions, but are generally assumed to be non-emissive and at the heart of so-called "self-quenching" behavior. The origin of the quenching in H-aggregates is that rapid internal conversion from the upper dipole-allowed exciton level to the lower dipole-forbidden levels depopulates the radiative species, resulting in the population of formally non-radiative species that ultimately relax by further internal conversion to the ground state, Figure 3-16.[86] Thus, a dipole-allowed transition typically populates the upper exciton level (resulting in the characteristic blue shift of the absorption peak), but radiation from this state is outcompeted by internal conversion to a lower non-radiative state.

Although optical transitions from the lower excited state of a perfectly ordered H-aggregate is forbidden, there is precedent for emission from H-aggregates. Spano and Silva modeled the electronic states giving rise to emission from conductive polymers as HJ-aggregates, with J-like interaction between chromophores within polymer chains and H-like interaction across chains.[123] The diversity of polymer morphologies leads to a complex range of delocalized electronic states observed in different systems. Of note, regioregular poly(3-hexylthiophene) films emit from an entirely H-like state.[124, 125] Emissive H-aggregates have also been observed in a number of small organic molecules. The mechanism generally involves imperfect H-aggregate formation, where angular rotation[126-129] or slip-stacking[130] between fluorophores leads to weakly allowed emission from the lower H-aggregate excited state. Alternatively, aggregation induced emission can occur when steric deactivation of isomerization or rotation reduces the nonradiative relaxation rate from the lower excited state.[126,131-134] In all of the cases of H-aggregate emission, emission was observed from the normally dark lower exciton-coupled state of the H-aggregate, and was thus red-shifted relative to the non-aggregated chromophore. Recently, Bayda and co-workers examined H-aggregates of phthalocyanines and observed emission from the upper exciton-coupled state.[135] They suggested that emission from the upper-exciton-coupled state was caused by thermal repopulation from the lower exciton-coupled state.[135] In all of these cases, H-aggregate emission, when observed, displayed a longer radiative lifetime than in the unaggregated chromophore. In all cases except for that reported by Bayda,[135] emission from the lower H-aggregate exciton peak is also redshifted relative to unaggregated chromophore, unlike the blue satellite peak in our system.

To account for our blue satellite peak, we propose a different mechanism for emission from the H-aggregate, Figure 3-16. As described above, the first step of the quenching mechanism of the H-aggregate is internal conversion depopulating the upper species. However, the rate of internal conversion scales inversely with the energetic distance between the upper state and the lower states, resulting in the well-known "energy gap law" for estimating relative rates of internal conversion.[86] The prediction then is that strongly coupled H aggregates where a large energy gap exists should exhibit slower internal conversion that is less able to outcompete fluorescence. This behavior is seen in species with large energetic gaps between S_1 and S_2 electronic states.[136] For example, room temperature solutions of 1,4-anthraquinone show emission from both S_1 and S_2 states with an 1100 cm^{-1} gap between them, similar to the spacing predicted here. As described by Kasha's rule, emission from S_2 is generally forbidden because of rapid internal conversion, similar to emission from the upper exciton band. However, in species where the gap is large, radiative emission from S_2 not only competes with internal conversion to S_1, but can be the dominant decay channel.

We propose that the blue-shifted satellite peak is emission from the upper exciton state in a strongly-coupled H-aggregate, Figure 3-16. We emphasize that the satellite peak is in most cases substantially less intense than the main peak, and thus emission from the species does not need to completely outcompete internal conversion, it just needs to be competitive enough to have a non-negligible quantum yield of emission. Thus, we expect the lifetime of this emissive species to be extremely short since internal conversion is still expected to be in the picosecond range. Bayda[135] also considered the possibility of this mechanism, but ultimately found a long-lived emission species, and thus rejected it in favor of thermal repopulation of the upper exciton-coupled state.

To test this prediction, monomer in 0.1 % toluene/IPA was spin-coated on glass coverslips at 5 μg/mL to create an array of nanoparticles which were investigated via fluorescence lifetime spectroscopy using 560 nm pump light with 100 kHz repetition rate at 15 nJ/pulse. Emission was detected on a streak camera with 40 ps time resolution. As seen in Figure 3-17a,c, the main peak and blue satellite observed in the single-particle fluorescence spectra are visible in the lifetime spectra. The major peak at 650 nm has a 2 ns lifetime, typical of emission from an organic dye, but the emission from the blue satellite peak is extremely short lived, with lifetime <40 ps, the streak camera time resolution. The extremely fast decay of the blue satellite fluorescence is consistent with emission from a higher electronic excited state like an upper exciton level, with an extremely short observed lifetime likely due to competition from a fast non-radiative decay. This short lifetime also additionally rules out emission from the bottom manifold of an H-aggregate via a softening of the symmetry rules forbidding emission, as described above, since this mechanism would be associated with a ns or greater lifetime. Spin-coated monomer nanoparticles heated at 80 °C for 3 hours behaved similarly to photothermally heated samples that showed an increased intensity of the blue satellite peak, Figure 10. Here, pre-heated samples showed an increased intensity of the blue satellite from 4% to 19% of the main fluorescence peak, with a similarly instrument-limited measured life-time, Figure 3-17b,c.

With this mechanism supported by time-resolved fluorescence, we can now present a succinct picture of how morphology maps onto emission properties. Computational results based on our crystal structure suggests domains ranging from the strongly H-coupled to the weakly J-coupled, Figure 3-15a. Species ranging from weakly H-coupled to strongly J-coupled should show emission in a spectral range near the isolated fluorophore and extending red, Figure 3-15b. Moderately H-coupled species should show no emission, as in these cases the internal conversion depopulating the upper exciton band is swift, as predicted by the energy gap law. Strongly H-coupled species should show weak, short-lived blue-shifted emission, as observed. Finally, the presence of the quenched range at moderate H-coupling means that this blue-shifted emission would appear as an isolated peak, Figure 3-15c, as observed in Figure 3-8.

It is likely that domains that display this characteristic blue emission are rather small. Even in optimally H-aggregated 1xN structures where N is large, Figure 3-14, though much of the density of states will be concentrated at the bottom of the energy ladder, some states will be distributed throughout the energy gap. These states may still provide efficient conduits for internal conversion, and as a consequence quenching, due to being closer in energy to the higher emissive states as predicted by the energy gap law. Alternatively, in large 1xN systems multiple closely spaced levels at the top of the manifold may be emissive, and consecutive relaxation through these levels may afford another pathway for emission, as the need to pass through multiple states could allow the slower radiative relaxation the opportunity to play a weak role. This pathway would also present with a fast excited state lifetime, as observed, and cannot be confirmed or ruled out with the available data.

While the computation in Figure 3-14 suggests a maximum blue shift of ~900 cm^{-1}, some of the satellite peaks seen in Figure 3-8 are even more blueshifted from the isolated monomer. Two factors may contribute to this difference. First, the DFT calculations in Figure 3-14 involve transition densities, and may overestimate charge delocalization. On the other hand, computation with point dipoles (see original publication) predicts larger shifts up to ~1700 cm^{-1}, with the true value likely lying somewhere between these limiting cases. Second, as discussed above, the crystal structure in Figure 3-12 should not be taken as a direct representation as to the precise ordering present in the nanoparticles, and that likely a diversity of molecular packings exists. Reduction of the intra-unit cell BODIPY-BODIPY distance by only 15% would elevate the blue shift to ~1500 cm^{-1} even via the transition density calculation.

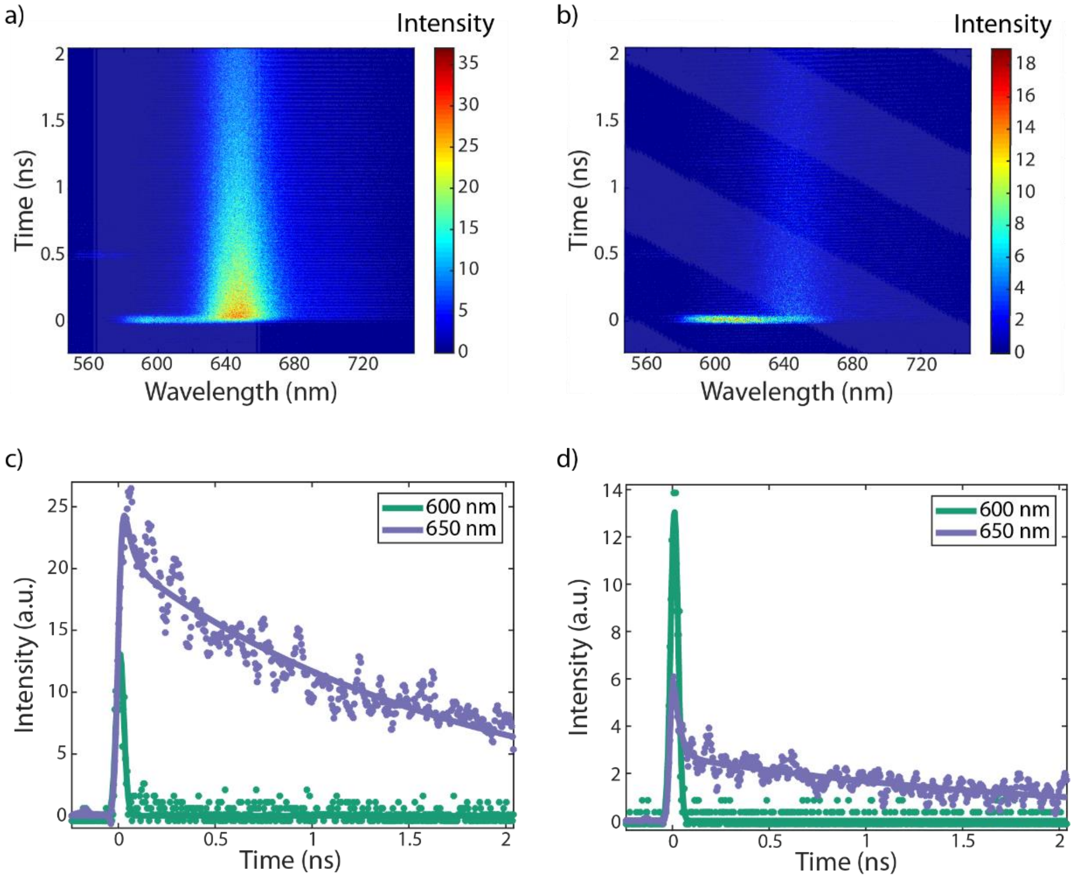

Figure 3-17. Fluorescence lifetime data. Time and wavelength-resolved emission of **monomer** nanoparticles before (a,c) and after (b,d) heating. In lifetime fits of unheated (c) and heated (d) **monomer** nanoparticles, the fluorescence of the blue satellite peak at 600 nm decays with a lifetime of <40 ps, limited by the instrument time resolution. The main peak at 650 nm fluorescence is well fit by a bi-exponential for both heated and unheated samples, with components of lifetime <40 ps and 2±0.2 ns in the unheated sample (c) or 1.7±0.2 ns in the heated sample (d). In the heated samples, the relative amplitude of the ultrafast decay increases significantly.

3.4.6 Understanding Spatially Non-Uniform Particles, Particle Thermal Evolution, and Spectral Diffusion

The scale in Figure 3-15 provides a framework to understand how the emissive properties of the nanoparticles vary in space and time, summarized in Figure 3-18. In the large particles in Figure 3-10, panel a) shows a spectral channel that includes the blue satellite peak, while panels b) and c) show a spectral channel that includes the red edge of the main peak. Just after deposition, upon excitation at 532 nm, considerably blue of the isolated monomer, the outer rims of the nanoparticles show evidence of the blue satellite peak. Excitation at 633 nm, resonant with the isolated monomer peak, results in only weak emission at the outer rim. Thus, the outer rim is composed predominantly of moderately and strongly coupled H-aggregates, resulting in domains that emit in the satellite peak or not at all. In contrast, the centers of the particles show emission in the main peak when excited at 532 or 633 nm. Thus, the centers are composed predominantly of domains that show weak H- or J-

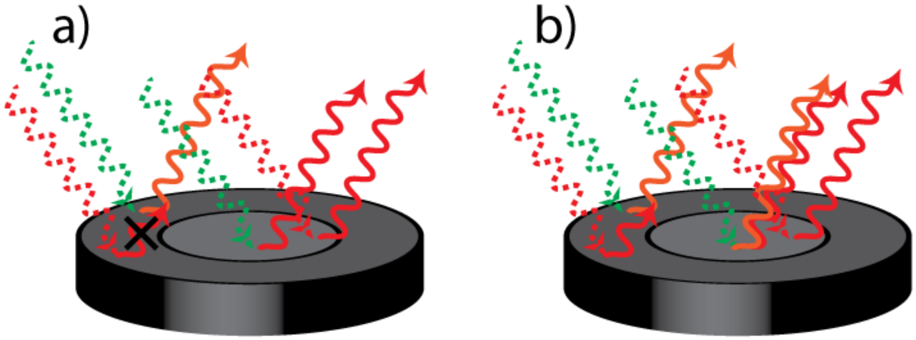

Figure 3-18. Model of spatially inhomogeneous particle emission properties with input (dashed) and output (solid) photons represented as wavy lines. Before photothermal annealing, a), particle rims demonstrate orange (blue satellite) emission upon green excitation, and no emission upon red excitation, while particle centers demonstrate red emission regardless of whether green or red excitation is applied. In contrast, after photothermal annealing, b), particle rims demonstrate orange (blue satellite) emission upon green excitation, and red emission upon red excitation, while particle centers demonstrate red emission with red excitation and both red and orange emission upon green excitation.

aggregation, with no evidence of the blue satellite and dominant emission in the red channel. These behavior are summarized in Figure 3-18a.

Upon exposure to prolonged 532 nm excitation, photobrightening occurs in both larger and smaller nanoparticles. After this process occurs in the larger nanoparticles, the outer rim exhibits a more intense blue satellite when excited at 532 nm, and moderate red emission when excited at 633 nm. Simultaneously, the center shows more intense emission in the red channel when excited at 633 nm, but now shows both blue satellite and main peak emission when excited at 532 nm. The scale in Figure 3-15 can be used to understand this transition. These dynamics are consistent with Ostwald ripening-like behavior, whereby the size distribution of aggregates becomes more extreme over time, previously reported in the synthesis of one-dimensional organic nanorods.[137] Throughout the nanoparticle, mid-sized domains that likely fell in the quenched portion of Figure 3-15c are being photothermally annealed, resulting in rearrangement of dye molecules inside the particle into more small domains that are more strongly H-coupled, as well as more large domains that exhibit weak J- or weak H-coupling. Thus, the main and satellite peaks both become stronger, as observed.

Single-particle emission spectra of small particles show (Figure 3-8) that the appearance of the blue satellite peak is highly dynamic, with the feature blinking and undergoing spectral diffusion or even showing multiple peaks. This observation is consistent with the mechanism above, that photothermal annealing results in domain-shifting structural changes. As the domains change size, their degree of H-coupling changes, moving along the scale in Figure 3-15c, resulting in a peak that changes its spectral location and amplitude. This strong correlation between domain geometry and emission properties then manifests itself in small nanoparticles, where there may only be one strongly H-coupled domain that is emissive, allowing observation of blinking and spectral diffusion (Figure 3-8, orange trace). In larger particles, these dynamics are apparent as brightening and darkening in different spectral channels (Figure 3-10). In single-particle spectra, the role of irreversible photobleaching is also more conspicuous at later times.

3.4.7 Alternative Theories for Blue Satellite Emission

The observations described above are consistent with a mechanism where strongly-coupled H-aggregates are capable of weakly emitting from the upper exciton band. Origins that rely on the presence of an impurity, a photochemical rearrangement, or emission from the lower manifold of states of the H-aggregate have all been ruled out above.

Another possibility is that rather than the blue satellite peak resulting from blue-shifted S_1 emission due to H-aggregation, it is red-shifted S_2 emission due to J-aggregation. This emission, accelerated over internal conversion due to the strong radiative rate enhancement associated with superluminescence,[138] would also manifest itself as a short-lived radiative state. However, we consider this mechanism unlikely, as the S_2 state has extremely small oscillator strength ($f=0.006$), and is blue shifted from the S_1 state by over 3400 cm^{-1} (see original publication), requiring an unphysically large degree of J-coupling in order to form the blue satellite peak.

Another potential explanation of the blue-shifted satellite peak is emission from a higher energy mode in the vibronic progression of the dye. Because the minor peak is blue of the major emission peak and the 0-0 transition of H-aggregates is suppressed,[123] it is tempting to assign the satellite to the 0-0 vibronic relaxation. However emission in this manner would be expected to be commensurate with an excited state lifetime that is similar to or longer than that for the main emission peak, which is not observed.

A final possible explanation considers the role of thermal repopulation of the upper excited state, superficially similar to the phenomenon of thermally activated delayed fluorescence (TADF) where a singlet state is thermally repopulated from a lower lying triplet state.[139] However, gaps of ~1000 cm^{-1} are considerably larger than kT (200 cm^{-1}) at room temperature. But, since excitation is made significantly blue shifted of the absorption peak, a significant amount of local heating will occur, as described above as the origin of the observed photothermal annealing. Thus, immediately after excitation a substantial amount of thermal energy would be available for partially repopulating the upper state. The lifetime of the emission from the upper exciton band would also be limited by the lifetime of this excess thermal energy, predicting a very short excited state lifetime, as observed. This situation is distinct from what is typically observed in TADF or in Bayda's system.[135] In the limit of complete equilibration, smaller energy gaps would also be predicted to be susceptible to this scheme of upper state repopulation, as detailed balance would require that repopulation rate to rise as the rate of depopulation of the upper state, internal conversion, also rises. Since we do not observe emission from species with intermediate gaps, this mechanism can only be valid if full equilibration is not reached and detailed balance is not enforced, leaving smaller gap emissive units effectively non-emissive from the upper state because internal conversation is still too fast. With the available evidence, we cannot eliminate non-equilibrium thermal repopulation as a possible mechanism.

3.5 Conclusions

When a bulky norbornyl alkyl tail is affixed to a spirofluorene-functionalized BODIPY, the resulting self-assembled nanoparticles contain quasi-two-dimensional sheets of chromophores that present a rich example of the complex relationship between structure and photophysical properties. The micromorphology of the domains, in particular the repetition of the unit cell along orthogonal axes, results in qualitatively different photophysical behavior, ranging from weak J-coupling to strong H-coupling. The strongest H-coupled domains have a blue satellite emission peak with picosecond excited-state lifetime consistent with the rare process of emission from the upper exciton level, a process forbidden by Kasha's rule but observable because of the strong H-coupling. Spectrally-resolved imaging, time-resolved fluorescence spectroscopy, photothermal effects, and spectral diffusion at the single-particle level show that these domains are spatially inhomogeneous and temporally dynamic.

The theme of coupling between structure and properties is an important one in organic electronic materials. Here, the availability of a crystal structure, and an unusual co-existence of two extremely different photophysical phenomena, even in the same nanoparticle, allows the unique opportunity to directly map structure from a photophysical observable in an organic nanoparticle, and as that physical structure evolves in space and time, so too does the photophysical behavior. Further, this work demonstrates a striking example of how structural defects can alter emission profiles, with emission from strongly H-aggregated domains providing a potential path for reducing spectral purity, a necessary requirement for OLEDs. Continued efforts at mapping structure and optical properties will reveal more mechanisms for how certain motifs in electronic structure can yield desired properties, whereas others represent pitfalls to be avoided.

3.6 Experimental Procedures

3.6.1 Synthetic Procedures

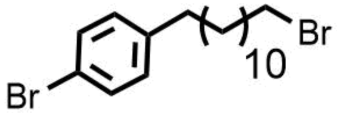

7

7: Compound **7** was synthesized by following a literature procedure. NMR spectra matched the spectra reported in the reference.[102]

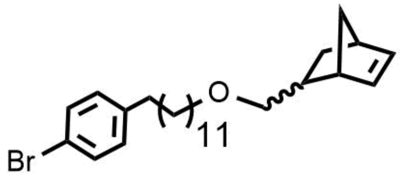

8

8: Compound **8** was synthesized by following a modified procedure.[140] A 50 mL single-neck round-bottom flask was charged with a solution of 5-norbornene-2-methanol (310 mg, 2.5 mmol) in 2 mL dry THF then cooled to 0 °C. Next, sodium hydride (mixture of *endo* and *exo* isomers) (60% in mineral oil, 171 mg, 4.3 mmol) was added and stirred for 30 min at 0 °C. Then, alkyl bromide **7** (1.0 g, 2.5 mmol) was added in 8 mL dry THF slowly at 0 °C. The reaction mixture was refluxed for 1 h and then stirred at room temperature for 24 h. The solution was then washed with deionized water and the mixture was partitioned between 1 M HCl and diethyl ether. The organic phase was washed with saturated sodium bicarbonate, brine, water, and then dried over magnesium sulfate. The mixture was purified via two sequential columns: 1:4 ethyl acetate: hexanes then 3:7 DCM: hexanes to give 414 mg product **8** (37% yield). ^{1}H NMR (400 MHz, $CDCl_3$) (mixture of isomers) δ 7.41 – 7.34 (d, *J* = 8.3 Hz, 2H), 7.07 – 7.01 (d, *J* = 8.3 Hz, 2H), 6.11 - 6.09 (m, 1.07H), 6.06 – 6.04 (m, 0.46H), 5.93 (m, 0.61H), 3.51 – 3.25 (m, 3.61H), 3.13 (m, 0.67H), 3.00 (t, *J* = 9.2 Hz, 0.68H), 2.91 (bs, 0.57H), 2.79 (bs, 1.34H), 2.74 (bs, 0.47H), 2.59 – 2.50 (m, 2.24H), 2.33 (m, 0.62H), 1.81 (m, 0.74H), 1.73 – 1.63 (m, 0.43H), 1.56 (m, 4.96H), 1.41 (m, 0.75H), 1.37 – 1.14 (m, 22H), 1.09 (m, 0.50H), 0.48 (m, 0.67H). ^{13}C NMR (126 MHz, $CDCl_3$) δ 141.84, 137.04, 136.65, 136.59, 132.50, 131.22, 130.16, 119.21, 75.50, 74.51, 71.16, 71.06, 49.40, 44.99, 43.98, 43.69, 42.19, 41.52, 38.87, 38.79, 35.35, 31.33, 29.75, 29.73, 29.71, 29.61, 29.59, 29.58, 29.55, 29.49, 29.45, 29.18, 29.17, 26.19, 26.17.ESI/EMM m/z calculated 464.2523, found 464.2520 $[M+NH_4]^+$.

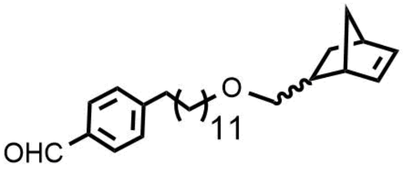

9

9: Compound **9** was synthesized by following a modified procedure as described in the reference.[141] A 50 mL single-neck round bottom flask was charged with **8** (300 mg, 0.67 mmol) and dissolved in 2 mL dry THF then cooled to -78 °C. Next, *n*-butyllithium (400 μL, 1.0 mmol, 2.5 M in hexanes) was added dropwise and the reaction mixture was stirred for 45 minutes at -78 °C. At this time, DMF (112 mg, 118 μL, 1.54 mmol) was added dropwise and the reaction mixture was stirred 45 minutes. Finally, the reaction mixture was warmed to 0 °C and then quenched with deionized water then extracted with diethyl ether (3 x), washed with water (3x) then dried over magnesium sulfate. The crude mixture was purified via column chromatography (1:9 ethyl acetate:hexanes) to furnish 135 mg **9** (51% yield). ^{1}H NMR (500 MHz, $CDCl_3$) (mixture of isomers) δ 9.97 (s, 1H), 7.83 – 7.77 (d, *J* = 8.1 2H), 7.34 (d, *J* = 7.9 Hz, 2H), 6.11 (m, 1.05H), 6.05 (m, 0.23H), 5.92 (m, 0.81H), 3.51 – 3.26 (m, 2.88H), 3.13 (m, 0.84H), 3.00 (m, 0.85H), 2.90 (bs, 0.74H), 2.78 (bs, 0.98H), 2.74 (bs, 0.31H), 2.72 – 2.65 (m, 2.04H), 2.33 (m, 0.85H), 1.81 (m, 0.89H), 1.71 – 1.60 (m, 2.22H), 1.59 – 1.50 (m, 2.99H), 1.41 (m, 0.88H), 1.38 – 1.13 (m, 19H), 1.09 (m, 0.24H), 0.48 (m, 0.83H). ^{13}C NMR (126 MHz, $CDCl_3$) δ 190.52, 149.01, 135.56, 135.16, 135.10, 132.89, 131.01, 128.39, 127.58, 74.02, 73.03, 69.67, 69.56, 47.92, 43.51, 42.50, 42.22, 40.71, 40.05, 37.39, 37.32, 34.74, 29.60, 28.27, 28.25, 28.23, 28.12, 28.09, 28.05, 28.01, 27.96, 27.78, 27.69, 24.71, 24.70. ESI/EMM m/z calculated 397.3101, found 397.3102 $[M+H]^+$.

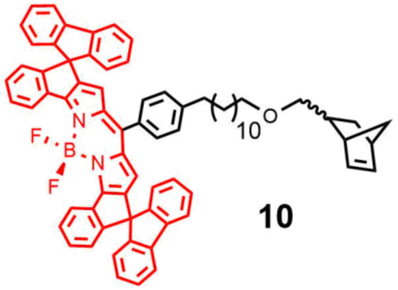

10

10: An oven-dried 50 mL single-neck round bottom flask with stir bar was capped with a septum and charged with aldehyde **9** (135 mg, 0.34 mmol) and pyrrole **3** (217 mg, 0.71 mmol) in dry DCM (10 mL). Next, two drops of trifluoroacetic acid were added and the mixture was stirred 16 h at room temperature under N_2. At this time, the reaction mixture was diluted with dry DCM (10 mL) and 2,3-Dichloro-5,6-dicyano-1,4-benzoquinone (DDQ, 84 mg, 0.37 mmol) was added in one portion as a solid and stirred for 1 hour at room temperature. After this, triethylamine (300 μL, 2.1 mmol) was added and stirred for 30 min at room temperature. Next, boron trifluoride diethyl etherate (46%, 600 μL, 1.8 mmol) was added and the reaction mixture was stirred for 3.5 h at room temperature. At this time, the solvent was removed under reduced pressure to give a dark red, thick, oily residue. The residue was purified via silica column chromatography using 1:1 DCM:hexane to give 179 mg (51% yield). ^{1}H NMR (500 MHz, CD_2Cl_2) (mixture of isomers) δ 8.36 (d, J = 7.7 Hz, 2H), 7.74 (d, J = 7.6 Hz, 4H), 7.45 (m, 2H), 7.29 (m, 4H), 7.23 – 7.19 (d, J = 8.1 Hz, 2H), 7.15 (m, 2H), 7.09 (m, 4H), 6.98 (d, J = 7.9 Hz, 2H), 6.86 (d, J = 7.6 Hz, 4H), 6.54 (d, J = 7.7 Hz, 2H), 6.16 (s, 2H), 6.01 (m, 1.02H), 5.95 (m, 0.44H), 5.82 (m, 0.54H), 3.37 – 3.15 (m, 3.31H), 3.00 (m, 0.56H), 2.88 (m, 0.56H), 2.77 (bs, 0.51H), 2.68 (m, 1.24H), 2.61 (m, 0.46H), 2.40 (m, 2.12H), 2.20 (m, 0.56H), 1.69 (m, 0.60H), 1.58 – 1.50 (m, 0.50H), 1.48 – 1.33 (m, 5.48H), 1.29 (m, 0.57H), 1.25 – 1.07 (m, 26H), 1.01 (m, 0.49H), 0.80 (m, 1.83H), 0.38 (m, 0.58H). Based on the ^{1}H NMR, the ratio of *endo/exo* isomers is 72/28. ^{13}C NMR (126 MHz, CD_2Cl2) δ 161.30, 156.83, 148.09, 145.38, 142.99, 142.71, 141.34, 141.09, 136.90, 136.55, 132.50, 132.41, 131.19, 130.48, 130.32, 128.69, 128.18, 128.04, 127.89, 124.15, 124.03, 123.96, 120.68, 120.12, 75.34, 74.37, 70.98, 70.87, 59.74, 49.28, 44.91, 44.03, 43.77, 42.25, 41.59, 38.96, 38.82, 35.58, 31.32, 29.78, 29.75, 29.69, 29.63, 29.57, 29.52, 29.45, 29.37, 29.20, 29.05, 26.19, 26.17, 22.34, 13.82. MALDI TOF – *m/z* 1034.1 $[M]^+$, 1015.1 $[M-F]^+$

Synthesis of Grubbs Generation III Fast-Initiating Catalyst [(H_2IMes)(3-Br-py)$_2$(Cl)$_2$Ru=CHPh]: Synthesized as described in the reference.[142]

Polymerization: A 5 mL single-neck round bottom flask with stir bar was charged with monomer (10 mg, 9.6 μmol) and chloroform (30 mM in monomer). Next, the reaction flask was cooled to -78 °C and Grubbs generation III catalyst (0.16 mg, 0.2 μmol) was added as a solution in chloroform. The reaction was stirred and slowly warmed to room temperature overnight. At this time, two drops of ethyl vinyl ether were added to quench the reaction and the polymer was precipitated out in methanol. Theoretical M_n = 50 x 10^3 Daltons, Observed (see table below)

M_n (Daltons)	22,240
M_w (Daltons)	38,270
M_z (Daltons)	55,744
M_p (Daltons)	42,961
M_w/M_n	1.721

Synthesis of H_2-monomer (11): In a 10 mL round-bottom flask, 10 mg monomer were dissolved in 1 mL dry THF along with 2 pipet-tips of palladium on carbon. The round-bottom flask was flushed with N_2 and then placed under vacuum to create a pressure differential. Next, a balloon containing H_2 was attached and the reaction was stirred for 1 hour (monitored by TLC). At this time, the reaction mixture was passed through a celite bed and washed with copious amounts of ethyl acetate. The complete disappearance of the alkenyl protons was apparent by ^{1}H-NMR.

Chapter 4

4. Synthetic Progress Toward a FRET-Based High-Throughput Screening Platform for Enantioselective Ring-Opening Reactions

4.1 Abstract

Optical methods for the high-throughput screening of asymmetric reactions offer a promising tool for expediting catalyst discovery and optimization within the synthetic chemistry community. We have designed a system that is based on a fluorophore "trio" using labeled epoxides and a phenol as Phenolic Kinetic Resolution reaction partners. We aim to use the Phenolic Kinetic Resolution reaction as a proof-of-concept that we predict can be extended to other nucleophilic ring-opening reactions and, thus, be a generalizable platform used to rapidly measure the % *ee* of such reactions. The synthetic strategy for obtaining this "trio" of fluorophores currently relies on straightforward and step-efficient chemistry such as cross-metathesis and the Williamson ether synthesis. First-generation adducts have been investigated using UV-Vis and fluorescence spectroscopy to determine their utility as FRET pairs. We have identified perylene as a promising donor in combination with two different BODIPY acceptors to form a functioning "trio".

4.2 Introduction

Many standard techniques for screening reactions are not viable for industrial scale, which has necessitated the use of high-throughput techniques.[143] The need for high-throughput screening technology began in the 1990s due to the rising popularity of combinatorial chemistry and the enormous compound libraries generated in the pharmaceutical industry.[144] After becoming relatively established in the pharmaceutical industry,[145] high-throughput screening has since extended to materials science and catalysis and has been drastically changing how many researchers work in these fields as it has the ability to expedite every step of the process from design to synthesis to evaluation.[145, 146] Combinatorial screening and high-throughput screening together have increased the probabilities and rates at which discoveries and innovations occur, reduced the time it takes for products to reach the market, and decreased costs.[146] High throughput screening techniques can be rapid and efficient and be designed such that there is an easily detectable signal for "hits" involving only a small sample volume and a robust platform.[143]

Asymmetric catalysis constitutes a significant and vital portion of all research in chemistry now, resulting in countless valuable products in many industries including pharmaceuticals, agrochemicals, and flavors and fragrances.[147] Its importance has also been recognized in the form of the Nobel Prize in Chemistry awarded to K. Barry Sharpless, William S. Knowles, and Ryoji Noyori in 2001.[147] The two most common forms of asymmetric catalysis are based on transition-metal reactions and enzymatic catalysis.[147] When chemists develop new asymmetric transition-metal catalyzed reactions, the process is typically based on tuning ligands (often selected from "privileged" classes), mechanistic understanding, computational modeling, and serendipity.[147] Despite considerable efforts and significant progress, it is still not possible to predict *a priori* which organometallic species will result in catalytically active conditions.[148] Moreover, even if a particular species is discovered to be active, it is often still necessary to select the proper solvent/temperature/etc. in addition to making further modifications to the ligand structure.[148] This makes research in the discovery and development in catalysis an expensive and highly empirical effort in most cases.[149]

High-throughput screening techniques have not been as utilized in the area of catalysis as compared to drug discovery in pharmaceutical research as there still exists a need for general methods,[145] but there are an increasing number of reports for methods related to catalysis.[150, 151]

However, methods amongst the more specific are of chiral catalysis are rarer than reports involving achiral or heterogeneous catalysis.[145] In a typical asymmetric reaction performed in the pharmaceutical industry, the optical purity of the product of the reaction is calculated by separating the enantiomers of the mixture using chiral HPLC and GC and calculating the excess after separation.[152] Calculating % *ee* by chiral GC and HPLC is limited to just dozens of determinations per day.[152] Combinatorial chemistry has increased the number of drug targets produced significantly, while analysis remains the bottleneck in the process – an issue many researchers are addressing through high-throughput screening.[153]

The traditional methods for analyzing the enantioselectivity of catalytic reactions of organic molecules are based on chromatography, NMR, and mass spec, with HPLC being the method of choice on industrial scales.[154] Many new techniques are being developed are based on optical methods.[154] Even though optical methods are usually less accurate than HPLC,[154] they can increase the number of samples being screened to as many as 1,000 per day.[152] One reason for this is that optical methods are amenable to being carried out in well plates.[154] Most of the optical methods for *ee* determination developed so far are based on are circular dichroism, UV-Vis absorbance, and fluorescence.[154] These methods are noted for being fast, operationally simple, and relatively inexpensive.[154]

A great deal of the pioneering work in optical high-throughput screening methods for catalysis has been made by the Hartwig group (Figure 4-1).[148, 155, 156] Two reports from the group are both based on a FRET-based fluorescence quenching optical process.[155, 156] The FRET donor-acceptor pair used in both studies relies on a dansyl dye as the donor and an azodye as the acceptor.[155, 156] When the dyes are covalently attached to reactive partners in cross-coupling reactions, product formation places them close enough in space for the donor emission to be quenched.[155, 156] From this, product formation can be correlated with donor emission intensity.[155, 156] The group has used this approach for the screening of room-temperature Heck coupling reactions as well as the arylation of amines.[155, 156]

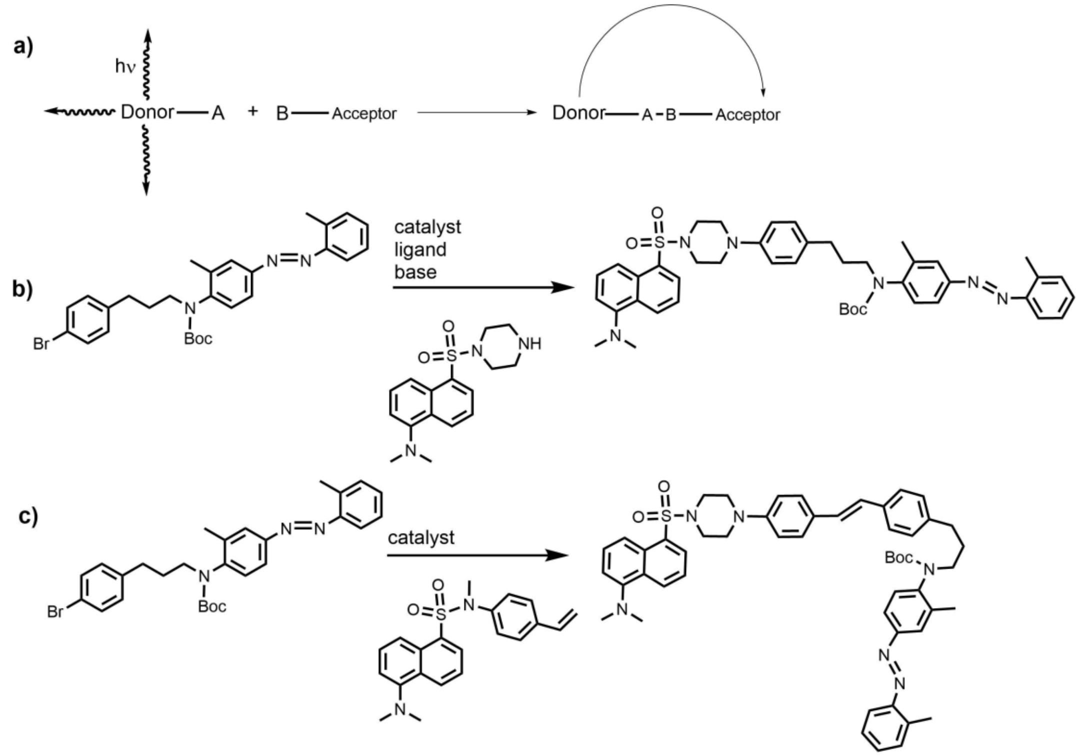

Figure 4-1. Hartwig Strategy for FRET-based high-throughput screening. a) General schematic of the basis for the FRET quenching strategy. b) System used for the high-throughput screening of catalyst-ligand combinations for the arylation of amines. c) System used for the high-throughput screening of room temperature Heck reactions. Figure adapted from references 148 and 155-156.

Some more recent examples which showcase the potential for optical methods in the determination of the *ee* of crude reaction mixtures have been developed for the Sharpless asymmetric dihyroxylation (SAAD).[154] A great deal of the pioneering work was made by the Anslyn group in 2009 (Figure 4-2).[157] A UV-Vis based enantioselective indicator displacement assay was performed based on the SAAD reaction of *trans*-stilbene.[157] The resulting product was isolated and subjected to an indicator displacement assay using the boronic acid hosts pictured (Figure 4-2) along with the indicator pyrocatechol violet (PV).[157] These assays are based on the difference in the absorbance spectrum before and after addition of hydrobenzoin due to the hydrobenzoin displacing the indicator from the host.[157] The reaction was carried out in a 96 well plate using two different ligands ($(DHQD)_2PHAL$ and (DHAD)CLB) and the UV-Vis absorption data was analyzed using an artificial neural network.[157] The absolute errors were only ±2.4 % for the reported *ee* values.[157]

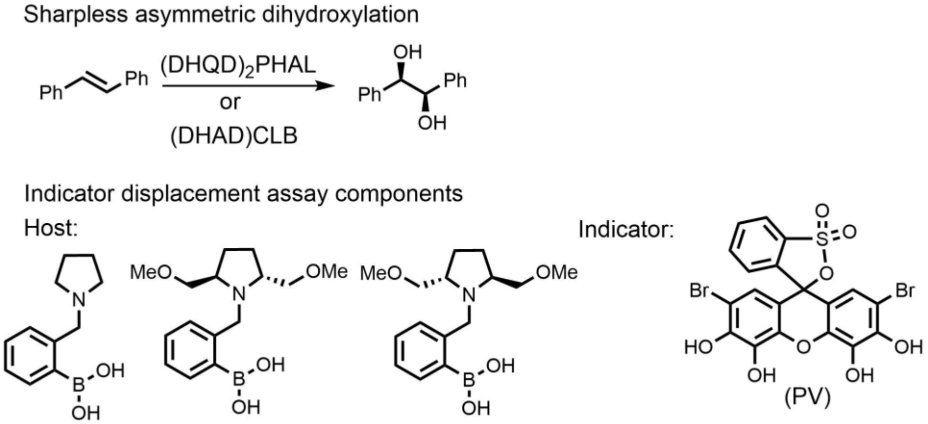

Figure 4-2. Indicator displacement assay-based system for the high-throughput screening of the SAAD reaction. Figure adapted from reference 154.

The Wolf group also reported on similar screening work using the SAAD reaction in 2016.[158] Their sensing was performed using only milligram scale crude reaction mixtures.[158] Their method is very simple and straightforward operationally.[158] The assay is based on a stereodynamic circular dichroism (CD) sensor.[158] Their sensor is a titanium-based sensor which binds to the chiral diol product generated from the SAAD reaction, importantly, as a crude reaction mixture.[158] In the report, the authors rigorously compare their method to using traditional methods based on chromatography.[158] The authors convincingly argue that their CD sensing method significantly reduces the solvent waste and total time.[158] It is crucial to point out the methods described in Figure 4-2 and Figure 4-3 were also both used to determine absolute configuration as well as yield in addition to *ee*, which highlights the utility of optical methods in high throughput screening.

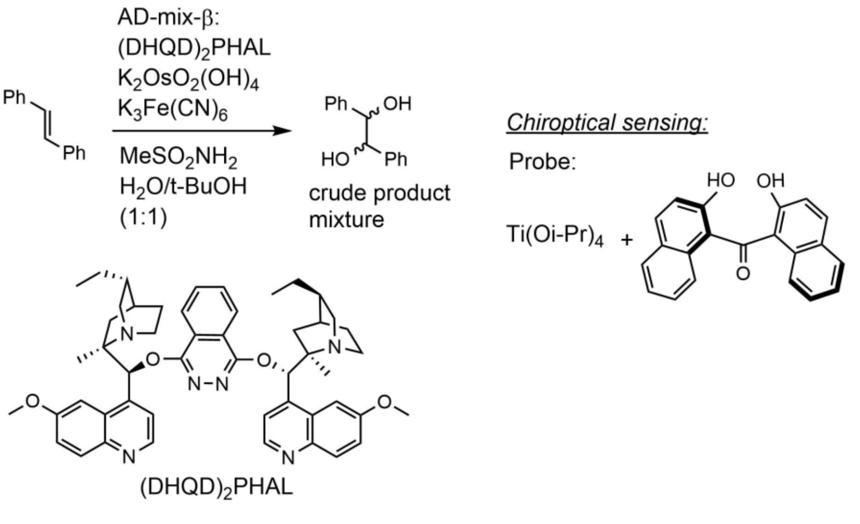

Figure 4-3. High-throughput screening technology developed by the Wolf group for the screening of the SAAD reaction. Figure adapted from reference 154.

4.3 Results

We aimed to develop a general platform for the high-throughput screening of enantioselective nucleophilic ring-opening reactions (Figure 4-4). For this, we used the Phenolic Kinetic Resolution (PKR) reaction developed by the Jacobsen group as a proof-of-concept.[159] The kinetic resolution of epoxides has been employed in the synthesis of several natural products[160] and is used in industry to manufacture tens of tons of enantiomerically pure epichlorohydrin annually,[161] albeit typically as a hydrolytic kinetic resolution (HKR) – a variant which was also developed by the Jacobsen lab. As seen in Figure 4-4, the system involves two different pseudoenantiomers of epoxides labeled with acceptor dyes A_1 and A_2 along with a donor dye attached to a phenol. After reaction with (salen) catalysts (catalyst identity, ligand identity, solvent, etc. could be screened), the well plates will have varying degrees of emission from the wavelength of each acceptor chromophore, corresponding to a different

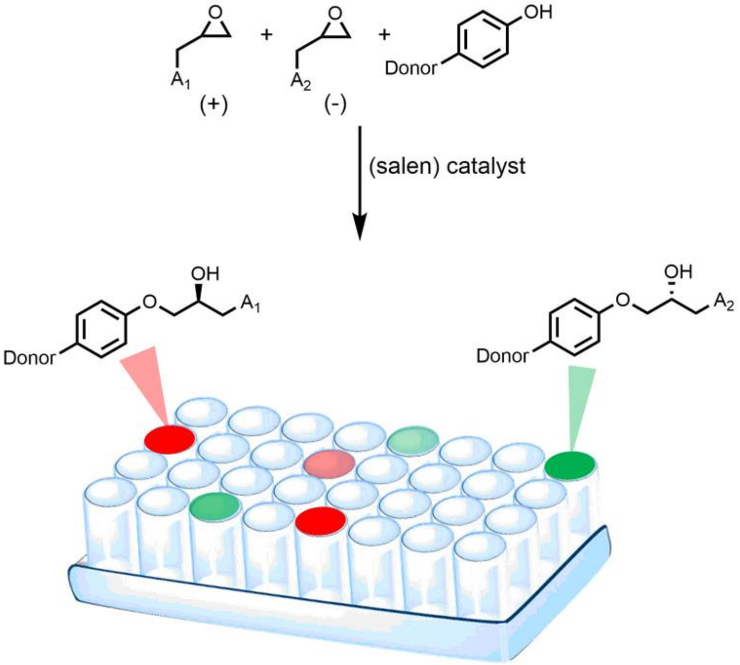

Figure 4-4. Cartoon of the proposed high-throughput screening platform.

enantiomer of epoxide reacted. Therefore, we expect this to give a method for the rapid estimation of enantiomeric excess.

The proposed strategy is in some sense a combination of the reports described in the introduction. It combines the covalently attached FRET-based strategy employed by the Hartwig lab (albeit, in a "turn on" sense, rather than quenching) with previous reports involving asymmetric catalysis. However, the target system involves the addition of a third fluorophore, to form a "trio" of fluorophores, which adds complexity to the design, synthesis, and analysis.

4.4 Convergent Synthesis of a "First Generation" PKR Adduct FRET Cassette

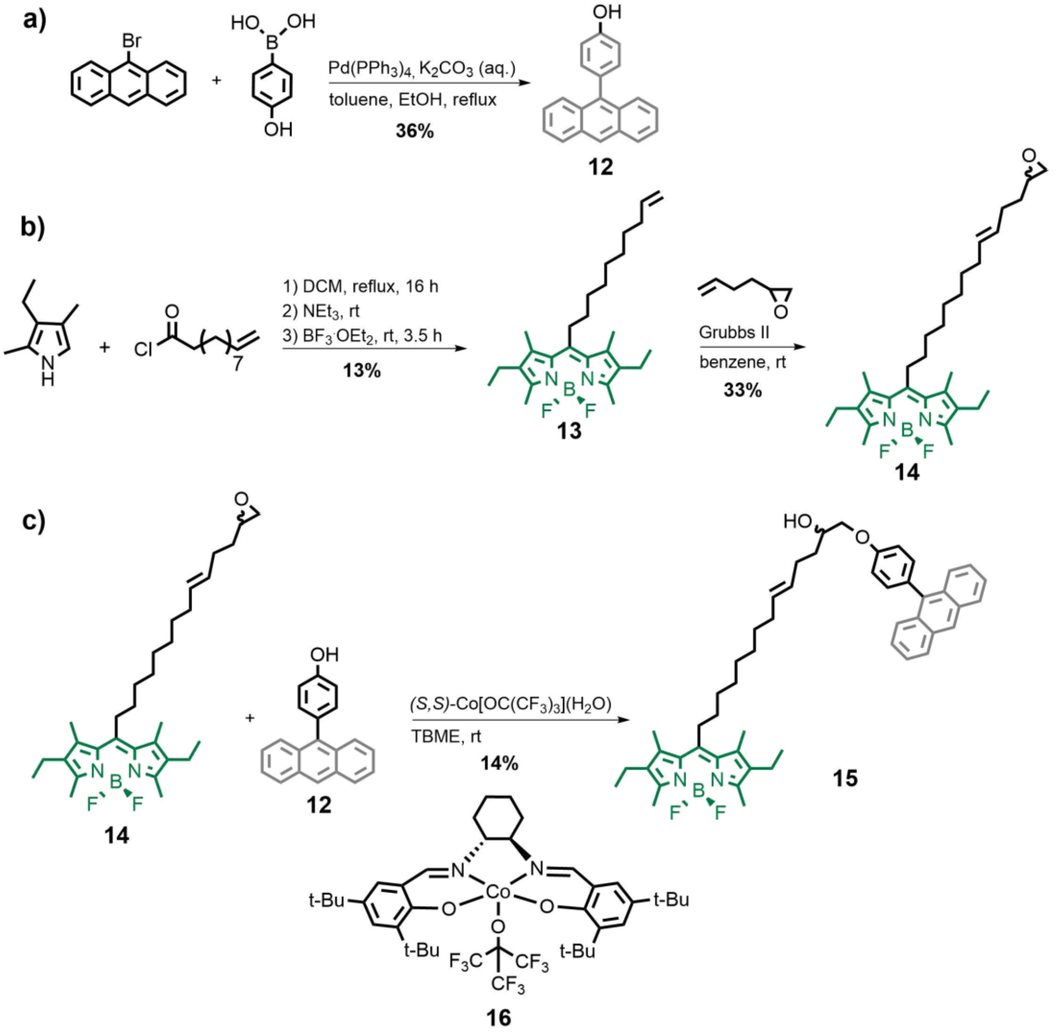

Figure 4-5. Synthetic scheme for the convergent synthesis of the green BODIPY-anthracene adduct. a) Synthesis of the anthracene phenol. b) Synthesis of the green BODIPY-labeled epoxide. c) PKR reaction to produce the final adduct.

A convergent synthetic scheme was devised for synthesizing terminal epoxides labeled with BODIPYs, a fluorescent phenol donor, and adducts thereof in a straightforward manner. The phenol donor is furnished in one simple step by a Suzuki coupling reaction (Figure 4-5a). Anthracene was selected as the donor chromophore due to its blue fluorescence emission being near the absorption of the green BODIPY dye previously employed by our group. In addition, polycyclic aromatic hydrocarbons such as anthracene are relatively easy to derivatize.[162] Syntheses of their derivatives are typically employed by halogenation followed by cross-coupling reactions such as Suzuki and Ullman type couplings or reactions with organolithium reagents.[162, 163]

The synthesis of BODIPY-labeled terminal epoxides is modular and can be performed in two steps (Figure 4-5b). In the first step, the green BODIPY functionalized alkene with a long alkyl linker was synthesized from a pyrrole and acyl chloride which are both commercially available. Next, the terminal epoxide was synthesized in one step via cross-metathesis. Thus far, only racemic epoxide has been used. However, it should be noted that the cross-metathesis should not result in epimerization as it has been applied in the synthesis of many natural products bearing multiple stereocenters.[164] In addition, the red BODIPY-labeled terminal alkene has previously been synthesized in our lab, which could serve as the third chromophore in the FRET "trio" upon cross-metathesis with an alkene bearing a terminal epoxide.

The final step of the scheme (Figure 4-5c) involves the synthesis of the FRET pair adduct via the PKR reaction. The reaction was performed using the perfluoro *tert*-butoxide counterion of the cobalt (salen) catalyst developed in the Jacobsen lab.[159] After synthesizing, the adduct, its UV-Vis and fluorescence spectra were analyzed and the adduct was evaluated as a functioning FRET pair (Figure 4-5). The spectra were taken in *tert*-butyl methyl ether (TBME) as it was the solvent used by the Jacobsen lab for running PKR reactions.[159] Unfortunately, it was determined that the molar extinction coefficient for anthracene is too small relative to that of the green BODIPY. Because of this, the anthracene moiety's absorption features are "buried" in the higher energy transitions of the BODIPY, which resulted in direct excitation (a false positive) for the green BODIPY.

4.5 Redesign of the Donor and Progress toward a "Second Generation" PKR Adduct FRET Cassette

Based on the optical results of the previous FRET cassette, it was decided to switch to a different chromophore. It is well-known that extending the number of rings in conjugated chromophore systems results in a larger molar extinction coefficient due to the increase in the molecular orbital size. Perylene was selected as the chromophore due to its higher molar extinction coefficient compared to anthracene (38,500 ε/M^{-1} cm^{-1} in cyclohexane[165] and 9,700 ε/M^{-1} cm^{-1} in $CHCl_3$[166], respectively). In addition, the target molecule was designed such that the phenol moiety is separated from the perylene chromophore through a short alkyl ether linker. There is evidence that phenols substituted with non-bulky groups have much higher reactivity in the PKR reaction compared to those with bulky substituents, such as naphthalene.[159]

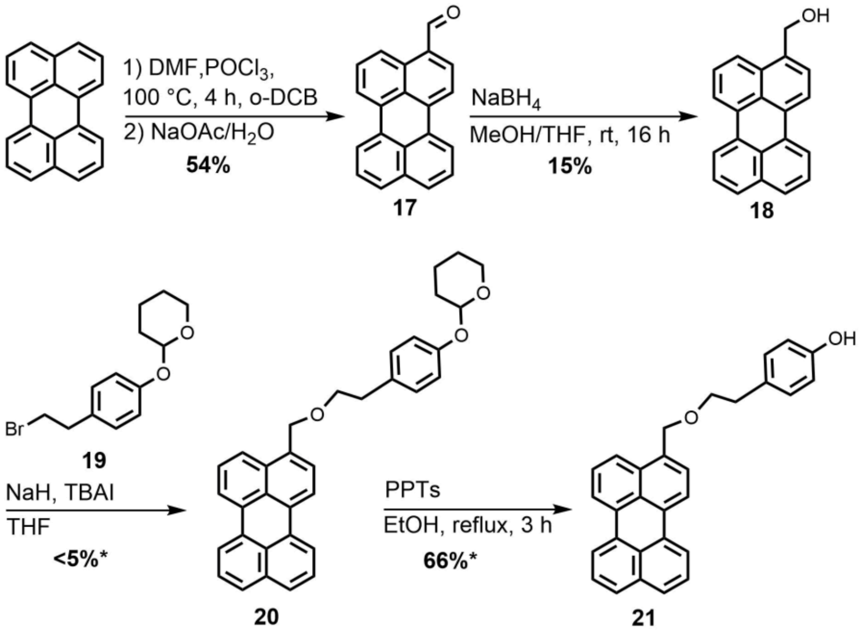

*Resulting materials not 100% pure. Yields reported are only estimates.

Figure 4-6. Synthetic scheme for the perylene phenol adduct.

The synthetic scheme for the perylene phenol target proceeded with a longest linear sequence of four steps (Figure 4-6). In the first step, a Vilsmeier–Haack reaction of perylene was peformed to furnish the aldehyde-functionalized perylene. The next step in the synthesis was the sodium borohydride reduction of the aldehyde to the corresponding alcohol. The phenol was attached to the alcohol-substituted perylene via a Williamson Ether Synthesis using a THP protected phenol. The THP protected phenol was furnished in one step with an excellent yield. Protecting group chemistry was used to avoid nucleophilic substitution from a free phenoxide ion. The THP protecting group was selected due to its compatibility with installation in the presence of an alkyl bromide and because its installation and removal are simple (mainly a matter of switching solvents). Next, the Williamson Ether Synthesis was preformed using sodium hydride along with tetrabutylammonium iodide as a phase transfer catalyst. Finally, the THP ether was removed by refluxing in ethanol.

4.6 Discussion and Conclusions

Arguably the most difficult aspect of this project is in selecting the appropriate "trio", which must fit certain parameters. They must be soluble in *tert*-butyl methyl ethers (perhaps other ether solvents such as diethyl ether or THF could be used as well). In addition, the fluorophores must form a set, or "trio", such that the donor emits where both acceptors absorb (a requirement for FRET), but the fluorescence emission wavelengths from the two donors must be separable (filters could be used if needed) so that the optical readout is different for the reaction of the two different pseudoenantiomeric epoxides. The synthetic scheme for the "trio" must also not be prohibitively step-intensive. The current scheme is straightforward. It involves using cross-metathesis to synthesize the fluorophore-labeled epoxides and the synthesis of the labeled phenol relies on a Williamson ether Synthesis reaction combined with well-known protecting group chemistry.

4.7 Future Work

The first portion of the continuation of this project relies on optimizing the synthesis and purification of perylene derivatives. The yields for several of these reactions can be improved by taking proper precautions. For several of the reactions reported, the literature values exceed those of the work in this thesis. Therefore, with repeated runs and added familiarity with perylene chemistry, it is expected that many of the yields can be increased. With increased yields, screening of steps within the scheme can be performed more readily and each step could, in theory, be optimized to become convenient as each step relies on relatively established reactions. Perylene still holds promise as a donor chromophore for the proposed FRET trio due to its relatively high extinction coefficient and wavelength of maximum absorption. It should also be added that perylene, like BODIPY dyes, bears less coordinating groups which could interfere with catalysts in future single-molecule experiments. Unfortunately, one issue with perylene discovered during this project is its poor solubility in most organic solvents. However, perylene and the derivatives in this report were found to be more soluble in tetrahydrofuran than toluene and halogenated solvents such as dichloromethane and chloroform. In addition, most of the literature seems to indicate that the solvent of choice for reactions involving perylene derivatives are performed in tetrahydrofuran. This works as an advantage for utilizing the proposed FRET trio in the Jacobsen PKR reaction as the literature precedent for the solvent used is TBME – a similar ether solvent in terms of functionality. It is not certain that switching to a different chromophore scaffold would be compatible with the PKR reaction since organic chromophores are known to often have solubility issues in general and some are more soluble in certain types of solvents as compared to others.

After synthesizing the target perylene-labeled phenol on a tenable scale, the next step is to complete the synthesis of each molecule needed for the screening reaction and control experiments.

For instance, the PKR adduct should be formed between the perylene phenol (Figure 4-6) donor and the green epoxide (Figure 4-5). The other proposed acceptor is the red BODIPY dye utilized extensively in the Goldsmith lab. The terminal alkene functionalized red BODIPY has been synthesized. The next step necessary is then to do the cross-metathesis reaction as has been performed with the green BODIPY analog. Even though a long alkyl linker was used in the syntheses of these molecules, control experiments should be performed to ensure that labeling with different BODIPY dyes does not affect the reactivity of the epoxides. Therefore, a set of four molecules should be synthesized comprising the red BODIPY with each enantiomer of epoxide as well as the two with the green BODIPY as the label. Perhaps the most straightforward way to accomplish this is to perform the cross-metathesis reaction with enantiomerically pure epoxide, which is commercially available, but often expensive.

With each molecule in hand, the major predicted difficulties of the project are expected to be tackled. The next step is to perform the screening reaction in 96 well plates using the PKR reaction as a proof-of-concept. Operationally, there is precedence by Hartwig for performing the reactions at a synthetically tenable concentration and then diluting by a specified factor before examining the fluorescence spectra, presumably to avoid the false positive signal which would be generated by collisional FRET.[155, 156] After testing this fluorophore "trio" kit using the PKR reaction, it would then be interesting, exciting, and challenging to extend this kit to other enantioselective ring-opening reactions. For instance, one could envision screening aziridine or cyclopropane ring-opening reactions using the modular nature of this kit. We are enthusiastic that this would then open the door for a new method to expedite the discovery and development of new enantioselective reactions.

4.8 Experimental Procedures

4.8.1 Synthetic Procedures

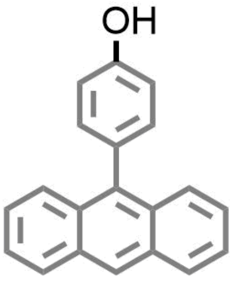

12

12: Compound **12** was synthesized according to a modified procedure.[167] A 100 mL two-neck RBF was charged with 9-bromoanthracene (1.0 g, 3.9 mmol, 1.0 eq), 4-hydroxyphenylboronic acid (590 mg, 4.3 mmol, 1.1 eq), potassium carbonate (1.0 g, 7.8 mmol, 2.0 eq), and $Pd(PPh_3)_4$ (224 mg, 0.19 mmol, 5 mol %) and was dried under vacuum and evacuated with N_2 3x and then ethanol (10 mL) and toluene (40 mL) were de-gassed with bubbling N_2 then added to the reaction flask. The reaction mixture was refluxed at 110 °C for 24 h. After this period, brine was added, and the mixture was extracted with ethyl acetate 3x and dried with $MgSO_4$ and concentrated under vacuum. The crude mixture was purified via column chromatography using 3:7 EtOAc:hexane and then flushed with 1:20 MeOH:EtOAc. The crude material was then washed with hexanes and recrystallized using ethyl acetate to give the product as a pale grey solid (370 mg, 36 %). $R_f = 0.30$ (20% EtOAc/hexanes), ^1H NMR (500 MHz, Chloroform-*d*) δ 8.48 (s, 1H), 8.04 (d, *J* = 8.4 Hz, 2H), 7.71 (d, *J* = 8.8 Hz, 2H), 7.45 (dd, *J* = 8.3, 6.6, 1.2 Hz, 2H), 7.38 – 7.33 (m, 2H), 7.33 – 7.28 (d, *J* = 8.4 Hz, 2H), 7.08 – 7.01 (d, *J* = 8.4 Hz,2H), 4.96 – 4.74 (m, 1H). ^{13}C NMR (126 MHz, $CDCl_3$) δ 154.91, 136.64, 132.51, 131.39, 131.07, 130.51, 128.33, 126.85, 126.43, 125.26, 125.07, 115.29. ESI-MS m/z calculated 269.0972, found 269.0971 $[M-H]^-$, 0.4 ppm.

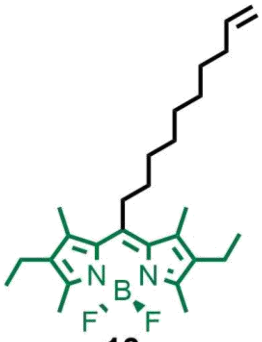

13

13: Compound **13** was synthesized according to a modified procedure.[168] A 250 mL two-neck RBF was charged 10-Undecenoyl chloride (486 mg, 2.4 mmol, 1.0 eq), 3-Ethyl-2,4-dimethylpyrrole (598 mg, 4.9 mmol, 2.1 eq) and 60 mL dichloromethane and refluxed for 16 hours at 42 °C. After this time, the reaction mixture was cooled to room temperature and then triethylamine (2.0 mL, 14.3 mmol, 6 eq) was added and stirred for 30 minutes followed by boron trifluoride diethyl etherate (4.0 mL, 46%, 12.0 mmol, 5 eq) and the reaction was stirred at room temperature for 3.5 hours. The solvent was removed, and the crude reaction mixture was purified directly by column chromatography using 3:5 DCM/hexanes to give the product as a dark reddish oil (150 mg, 13%). ^{1}H NMR (400 MHz, Chloroform-*d*) δ 5.81 (ddt, *J* = 16.9, 10.2, 6.7 Hz, 1H), 5.07 – 4.86 (m, 2H), 3.02 – 2.91 (m, 2H), 2.49 (s, 5H), 2.40 (q, *J* = 7.6 Hz, 4H), 2.33 (s, 6H), 2.05 (m, 2H), 1.70 – 1.18 (m, 13H), 1.05 (t, *J* = 7.5 Hz, 6H). ^{13}C NMR (126 MHz, $CDCl_3$) δ 152.00, 151.98, 151.97, 145.01, 139.11, 135.65, 132.51, 130.94, 114.23, 33.76, 31.84, 30.34, 29.44, 29.40, 29.06, 28.89, 28.57, 17.20, 14.84, 13.34, 12.40. MALDI-TOF m/z - 442.4 $[M]^+$.

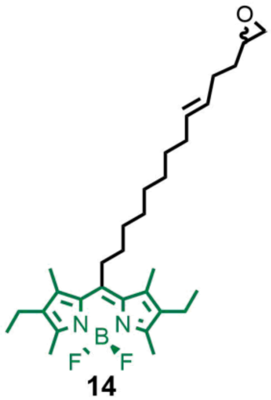

14

14: Compound **14** was synthesized according a modified literature procedure.[44] A 50 mL round bottom flask was charged with **13** (113 mg, 0.3 mmol, 1.0 eq), 1,2-Epoxy-5-hexene (125 mg, 144 μL, 1.3 mmol, 5.0 eq) and benzene (12.5 mL) and the mixture was de-gassed with bubbling N_2. Next, Grubbs generation II catalyst (25 mg, 0.03 mmol, 10 mol%) was added and the reaction mixture was again de-gassed briefly with bubbling N_2. The reaction mixture was stirred vigorously under N_2 for 20 hours at room temperature and then quenched with ethyl vinyl ether (1 mL). The crude mixture was purified via preparative TLC (1:1 DCM/hexanes) and the bottom band was isolated to give the product (50 mg, 33%). This yield was calculating based on pure material, but the NMR spectra indicate the presence of a fluorine-containing impurity which is particularly noticeable in the ^{13}C and ^{19}F NMR spectra. ^{1}H NMR (400 MHz, Chloroform-d) δ 5.61 – 5.33 (m, 2H), 3.07 – 2.87 (m, 3H), 2.75 (t, *J* = 4.5 Hz, 1H), 2.49 (s, 6H), 2.40 (q, *J* = 7.6 Hz, 4H), 2.33 (s, 6H), 2.23 – 2.10 (m, 2H), 2.08 – 1.92 (m, 2H), 1.70 – 1.54 (m, 5H), 1.48 (m, 2H), 1.32 (m, 9H), 1.05 (t, *J* = 7.6 Hz, 6H). ^{13}C NMR (126 MHz, CDCl3) δ 151.99, 145.00, 135.64, 132.51, 131.32, 130.94, 128.91, 51.96, 47.20, 32.54, 32.51, 31.84, 30.37, 29.50, 29.47, 29.43, 29.11, 29.03, 28.57, 17.20, 14.84, 13.34, 12.40. ^{11}B NMR (128 MHz, Chloroform-d) δ 0.62 (t, *J* = 33.7 Hz). ^{19}F NMR (377 MHz, Chloroform-d) δ -146.00 (*apparent* dd, *J* = 61.1, 31.9 Hz). Actual spectrum probably two overlapping quartets. MALDI-TOF $[M]^+$ 512.34.

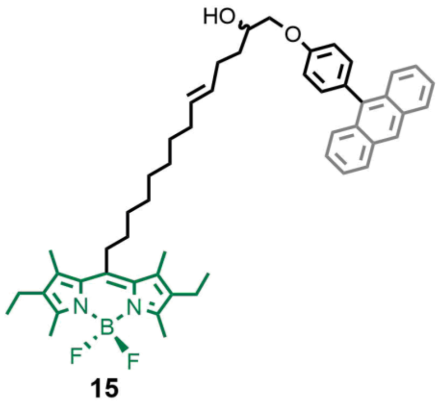

15

15: Compound **15** was synthesized according to a modified literature procedure.[159] A 4 mL vial (1 dram) was charged with **14** (50 mg, 0.1 mmol, 1 eq) and **12** (12 mg, 0.045 mmol, 0.45 eq), and (*S,S*)-(salen)Co[OC(CF_3)$_3$](H_2O) (4 mg, 4.4 μmol, 10 mol%) and 500 μL tert-butyl methyl ether (TBME). The reaction was stirred at room temperature 16 hours and then concentrated. The crude mixture was purified via preparative TLC multiple times (first 3:7 EtOAc/hexanes followed by 100% $CHCl_3$) to obtain **D** (5 mg, 14% yield). This yield was calculating based on the material being 100% pure, however, some grease is evident in the NMR spectra. ^{1}H NMR (500 MHz, Chloroform-*d*) δ 8.48 (s, 1H), 8.03 (d, *J* = 8.4 Hz, 2H), 7.73 – 7.65 (d, *J* = 9.3 Hz, 2H), 7.48 – 7.41 (m, 2H), 7.39 – 7.30 (m, 4H), 7.16 – 7.09 (d, *J* = 8.6 Hz, 2H), 5.58 – 5.39 (m, 2H), 4.17 – 4.08 (m, 2H), 4.03 – 3.94 (m, 1H), 3.02 – 2.91 (m, 2H), 2.49 (s, 6H), 2.43 – 2.34 (m, 4H), 2.32 (d, *J* = 6.7 Hz, 6H), 2.02 (q, *J* = 6.7 Hz, 1H), 1.78 – 1.66 (m, 1H), 1.62 (m, 1H), 1.52 – 1.44 (m, 1H), 1.44 – 1.18 (m, 24H), 1.04 (*apparent* td, *J* = 7.6, 2.3 Hz, 6H). ^{13}C NMR (126 MHz, $CDCl_3$) δ 158.08, 151.99, 145.00, 136.63, 135.65, 132.51, 132.39, 131.46, 131.41, 131.36, 130.94, 130.51, 129.33, 128.36, 126.83, 126.47, 125.27, 125.07, 114.48, 72.28, 69.78, 33.00, 32.58, 31.83, 30.38, 29.56, 29.50, 29.43, 29.16, 28.63, 28.57, 17.19, 14.84, 13.34, 12.40. MALDI-TOF m/z – observed 782.6 $[M]^+$, 763.6 $[M-F]^+$.

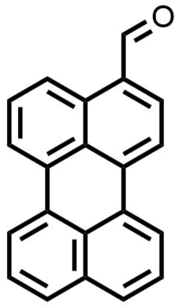

17

17: Compound **17** was synthesized according to a modified literature procedure.[169] A 100 mL two-neck RBF was charged with perylene (2.52 g, 10 mmol, 1 eq), anhydrous *ortho*-dichlorobenzene (5 mL), and anhydrous DMF (4.75 g, 5.1 mL, 65 mmol, 6.5 eq) and the reaction mixture was heated to 100 °C. Next, $POCl_3$ (3.07 g, 20 mmol, 2 eq) was added dropwise and the reaction mixture was heated and stirred for 4 hours. The reaction mixture turned a deep reddish purple. After this period, the reaction mixture was cooled to room temperature then added to a beaker containing 500 mL H_2O and neutralized with sodium acetate. Next, the solution was cooled to 0 °C then filtered and washed with water. The resulting crude yellow solid was then purified via recrystallization using 80 mL of toluene heated to 70 °C to give the product **E** as a yellow solid (1.5 g, 54%). This yield was calculated based on the assumption that the product is 100% pure, however, a significant amount of unreacted perylene starting material is present in the ^{1}H-NMR. The ^{1}H-NMR was compared to that reported in the literature and all the diagnostic peaks were found.[169] R_f = 0.57 (100% DCM). ^{1}H NMR (400 MHz, Chloroform-*d*) δ 10.33 (s, 1H), 9.18 (d, *J* = 8.5 Hz, 1H), 8.30 (m, 4H), 8.18 (d, *J* = 7.5 Hz, 3H), 7.95 (d, *J* = 7.8 Hz, 1H), 7.82 (d, *J* = 8.1 Hz, 1H), 7.76 (d, *J* = 8.1 Hz, 1H), 7.69 (m, 5H), 7.59 – 7.43 (m, 5H).

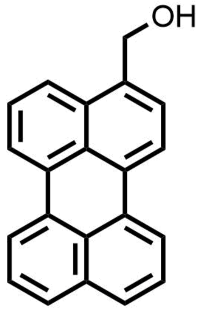

18

18: Compound **18** was synthesized according to a modified literature procedure.[169] A 250 mL single-neck round-bottom flask was charged with **17** (1.5 g, 5.4 mmol, 1 eq) and dissolved in THF/MeOH (2:1, 150 mL) and stirred for about 5 minutes to ensure the starting material dissolved. Next, $NaBH_4$ (608 mg, 16 mmol, 3 eq) was crushed with a mortar and pestle and added portion-wise with the round-bottom flask open to air until the bubbling stopped. After this, the reaction mixture was stirred under N_2 for 16 hours. The reaction mixture was concentrated and then purified via column chromatography (100% DCM) to obtain the product as a yellow solid (230 mg, 15%). $R_f = 0.17$ (100% DCM). ^1H NMR (400 MHz, Chloroform-*d*) δ 8.21 (m, 4H), 7.96 (d, *J* = 8.4 Hz, 1H), 7.70 (d, *J* = 8.1 Hz, 2H), 7.61 – 7.43 (m, 4H), 5.11 (d, *J* = 5.3 Hz, 2H), 1.73 (t, *J* = 5.8 Hz, 1H).

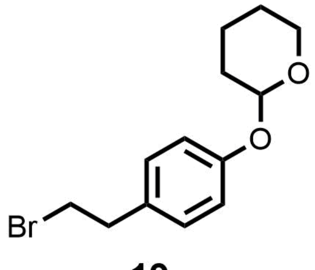

19

19: Compound **19** was synthesized according to a literature procedure.[170] A single-neck 15 mL round-bottom flask was charged with *p*-Hydroxyphenethyl bromide (600 mg, 3 mmol), 3,4-Dihydro-2H-pyran (411 μL, 4.5 mmol), and dichloromethane (5 mL). Next, Pyridinium *p*-toluenesulfonate (PPTs, 75 mg, 0.3 mmol) was added and the reaction mixture was stirred at room temperature for 16 hours under N_2. At this time, the reaction mixture was diluted with DCM and extracted with DCM/brine (3x), dried with Na_2SO_4, and concentrated. The crude product was purified via column chromatography (1:20 EtOAc/hexanes → 1:9 EtOAc/hexanes gradient) to give compound **19** (763 mg, 90%) as a colorless liquid. ^{1}H NMR (400 MHz, Chloroform-*d*) δ 7.12 (d, *J* = 8.6 Hz, 2H), 7.00 (d, *J* = 7.6 Hz, 2H), 5.39 (t, *J* = 3.3 Hz, 1H), 3.91 (m, 1H), 3.60 (m, 1H), 3.52 (t, *J* = 7.7 Hz, 2H), 3.10 (t, *J* = 7.7 Hz, 2H), 2.09 – 1.92 (m, 1H), 1.85 (m, 2H), 1.76 – 1.51 (m, 3H). ^{13}C NMR (126 MHz, $CDCl_3$) δ 156.04, 131.96, 129.59, 116.58, 96.40, 62.06, 38.72, 33.28, 30.37, 25.21, 18.80. ASAP-MS m/z calculated 285.0458, found 285.0483 $[M+H]^+$, 0.7 ppm

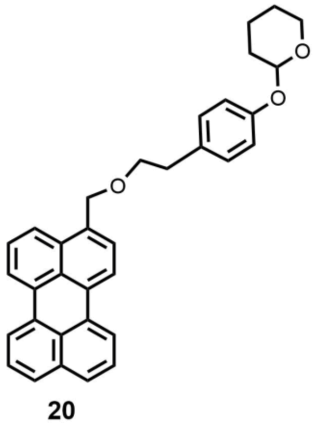

20

20: A 15 mL 2-neck oven-dried round-bottom flask was charged with **18** (200 mg, 0.7 mmol) and dry THF (5 mL). Next, sodium hydride (60% in mineral oil, 33 mg, 0.84 mg) was added at 0 °C and gradually warmed to room temperature while stirring overnight. After this, **19** (240 mg, 0.84 mmol) was added in THF (2 mL) dropwise and the reaction mixture was refluxed for 16 hours. The reaction mixture was quenched with sat. NH_4Cl and then extracted with EtOAc/H_2O then washed with brine and dried with $MgSO_4$. The crude material was concentrated to give a yellow solid (14 mg, <5%). R_f = 0.39 (100% $CHCl_3$) ^{1}H NMR of the crude material (400 MHz, Chloroform-*d*) δ 8.75 (d, *J* = 8.6 Hz, 1H), 8.31 – 8.05 (m, 6H), 7.74 (dd, *J* = 17.9, 8.1 Hz, 2H), 7.62 – 7.43 (m, 4H), 7.24 (d, *J* = 2.1 Hz, 1H), 7.18 – 6.92 (m, 5H), 5.40 (dm, 2H), 4.60 (t, *J* = 7.0 Hz, 2H), 4.24 (t, *J* = 7.1 Hz, 1H), 3.92 (m, 2H), 3.60 (m, 2H), 3.10 (t, *J* = 7.0 Hz, 2H), 2.87 (t, *J* = 7.1 Hz, 1H), 2.28 (t, *J* = 7.5 Hz, 1H), 2.11 – 1.92 (m, 3H), 1.86 (m, 4H), 1.76 – 1.51 (m, 7H), 0.73 (m, 2H).

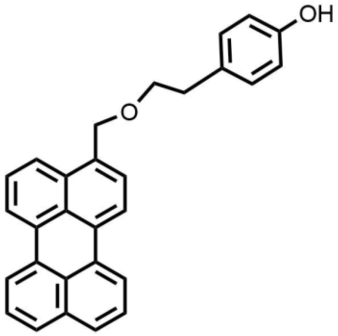

21

21: Compound **21** was synthesized according to a modified literature procedure.[171] A 10 mL single-neck round-bottom flask was charged with crude **20** (14 mg, 0.03 mmol), Pyridinium *p*-toluenesulfonate (8 mg, 0.03 mmol), and ethanol (HPLC grade, 5 mL) and the reaction mixture was refluxed at 80 °C for 16 hours. The reaction was worked up by removing the ethanol then extracting with $CHCl_3/H_2O$ (3x) and drying the combined organic layer with Na_2SO_4. The crude mixture was concentrated and purified via preparative TLC (100% $CHCl_3$) to give **21** (10 mg, 66%). R_f = 0.11 (100% $CHCl_3$). ^{1}H NMR (400 MHz, Chloroform-*d*) δ 8.74 (d, *J* = 8.6 Hz, 1H), 8.25 (t, *J* = 6.8 Hz, 3H), 8.18 (d, *J* = 8.0 Hz, 1H), 8.10 (d, *J* = 8.0 Hz, 1H), 7.75 (dd, *J* = 17.9, 8.1 Hz, 2H), 7.62 – 7.49 (m, 3H), 7.24 – 7.18 (m, 2H), 7.08 (d, *J* = 8.4 Hz, 1H), 6.86 – 6.80 (m, 2H), 6.77 (d, *J* = 8.4 Hz, 1H), 4.60 (t, *J* = 6.9 Hz, 2H), 4.24 (t, *J* = 7.1 Hz, 1H), 3.09 (t, *J* = 6.9 Hz, 2H). ^{13}C NMR (126 MHz, $CDCl_3$) δ 167.39, 154.29, 135.74, 134.44, 133.02, 131.25, 131.02, 130.28, 130.16, 129.21, 128.11, 128.03, 127.98, 126.11, 125.75, 121.86, 115.51, 115.37, 115.24, 65.81, 64.93, 34.41, 34.28, 31.94, 29.72, 29.67, 29.38, 26.72, 22.71. ESI/MS, calculated, 401.1547, found 401.1548 $[M-H]^-$, 0.2 ppm.

4.8.2 UV-Vis and Fluorescence Spectra

Compound **15** absorbance spectrum in TBME

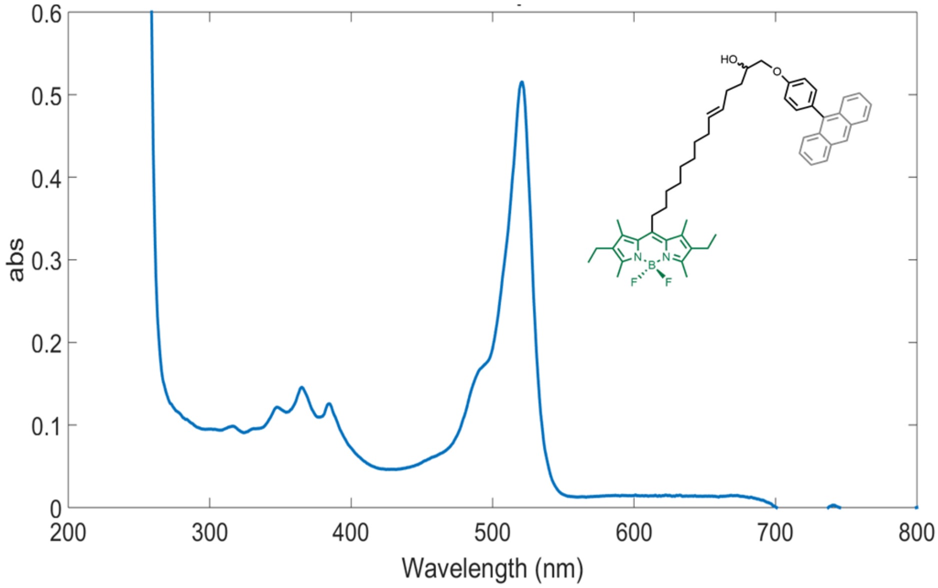

Compound **15** fluorescence emission spectrum, excitation at 367 nm in TBME

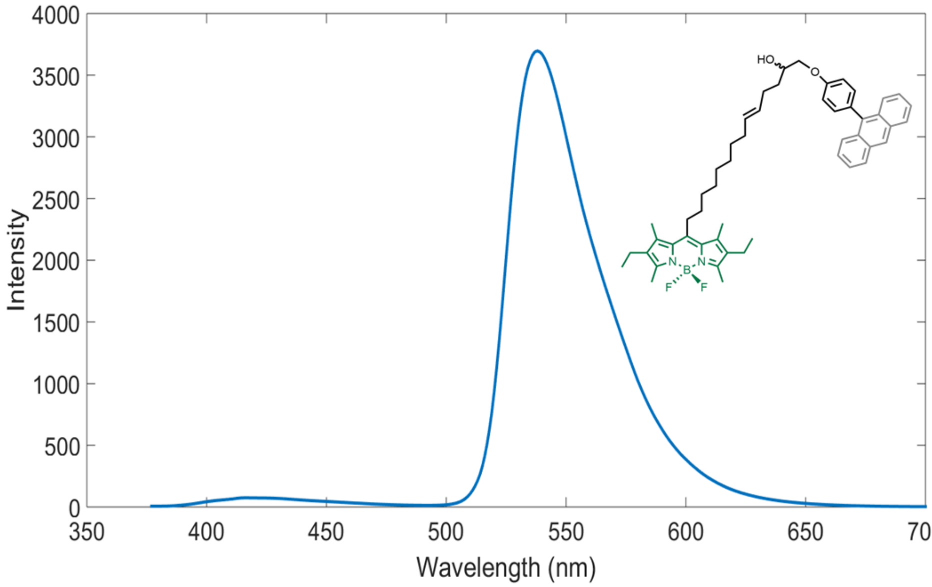

"Methyl green" BODIPY fluorescence emission spectrum, excitation at 367 nm in $CHCl_3$

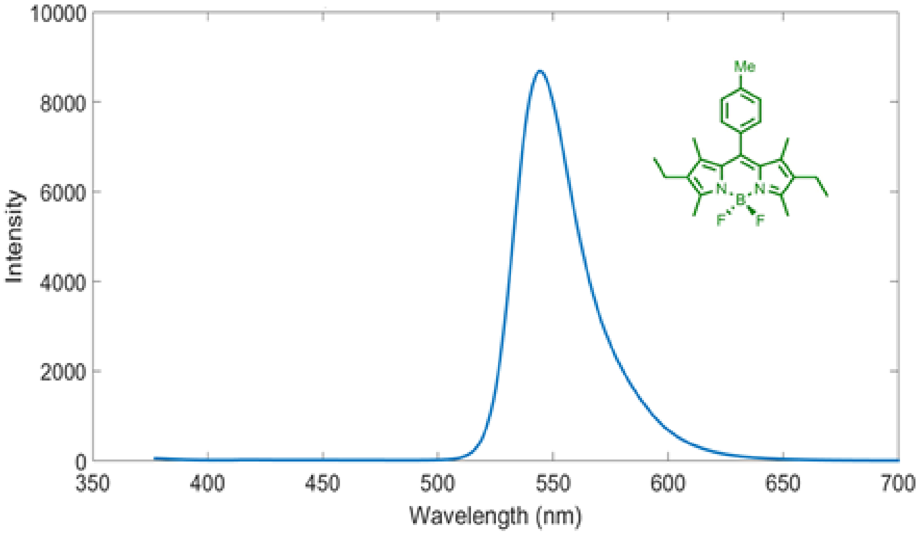

References

1. English, B. P.; Min, W.; van Oijen, A. M.; Lee, K. T.; Luo, G.; Sun, H.; Cherayil, B. J.; Kou, S. C.; Xie, X. S., Ever-Fluctuating Single Enzyme Molecules: Michaelis-Menten Equation Revisited. *Nature Chem. Bio.* **2006,** *2* (2), 87-94.

2. Velonia, K.; Flomenbom, O.; Loos, D.; Masuo, S.; Cotlet, M.; Engelborghs, Y.; Hofkens, J.; Rowan, A. E.; Klafter, J.; Nolte, R. J. M.; de Schryver, F. C., Single-Enzyme Kinetics of CALB-Catalyzed Hydrolysis. *Angew. Chem.* **2005,** *117* (4), 566-570.

3. Lu, H. P.; Xun, L.; Xie, X. S., Single-Molecule Enzymatic Dynamics. *Science* **1998,** *282*, 1877-1882.

4. Smiley, R. D.; Hammes, G. G., Single Molecule Studies of Enzyme Mechanisms. *Chem. Rev.* **2006,** *106*, 3080-3094.

5. Roeffaers, M. B. J.; De Cremer, G.; Uji-i, H.; Muls, B.; Sels, B. F.; Jacobs, P. A.; De Schryver, F. C.; De Vos, D. E.; Hofkens, J., Single-Molecule Fluorescence Spectroscopy in (Bio)Catalysis. *Proc. Natl. Acad. Sci. U. S. A.* **2007,** *104* (31), 12603-12609.

6. Xu, W.; Kong, J. S.; Yeh, Y. T.; Chen, P., Single-Molecule Nanocatalysis Reveals Heterogeneous Reaction Pathways and Catalytic Dynamics. *Nature Mat.* **2008,** *7* (12), 992-6.

7. Roeffaers, M. B.; Sels, B. F.; Uji, I. H.; De Schryver, F. C.; Jacobs, P. A.; De Vos, D. E.; Hofkens, J., Spatially Resolved Observation of Crystal-Face-Dependent Catalysis by Single Turnover Counting. *Nature* **2006,** *439* (7076), 572-5.

8. Roeffaers, M. B. J.; Cremer, G. D.; Libeert, J.; Ameloot, R.; Dedecker, P.; Bons, A.-J.; Martens, J. A.; Sels, B. F.; De Vos, D. E.; Hofkens, J., Super-Resolution Reactivity Mapping of Nanostructured Catalyst Particles. *Angew. Chem. Int. Ed.* **2009,** *48*, 9285-9289.

9. Ameloot, R.; Roeffaers, M.; Baruah, M.; Cremer, G. D.; Sels, B.; De Vos, D.; Hofkens, J., Towards Direct Monitoring of Discrete Events in a Catalytic Cycle at the Single Molecule Level. *Photochem. Photobiol. Sci.* **2009,** *8*, 453-456.

10. Xu, W.; Kong, J.; Chen, P., Probing the Catalytic Activity and Heterogeneity of Au-Nanoparticles at the Single-Molecule Level. *Phys. Chem. Chem. Phys.* **2009,** *11* (15), 2767-2778.

11. Zou, N.; Zhou, X.; Chen, G.; Andoy, N. M.; Jung, W.; Liu, G.; Chen, P., Cooperative Communication within and between Single Nanocatalysts. *Nat. Chem.* **2018,** *10*, 607-614.

12. Andoy, N. M.; Zhou, X.; Choudhary, E.; Shen, H.; Liu, G.; Chen, P., Single-Molecule Catalysis Mapping Quantifies Site-Specific Activity and Uncovers Radial Activity Gradient on Single 2D Nanocrystals. *J. Am. Chem. Soc.* **2013,** *135*, 1845-1852.

13. Zhou, X.; Andoy, N. M.; Liu, G.; Choudhary, E.; Han, K.-S.; Shen, H.; Chen, P., Quantitative Super-Resolution Imaging Uncovers Reactivity Patterns on Single Nanocatalysts. *Nature Nanotech.* **2012,** *7*, 237-241.

14. Shen, H.; Zhou, X.; Zou, N.; Chen, P., Single-Molecule Kinetics Reveals a Hidden Surface Reaction Intermediate in Single-Nanoparticle Catalysis. *J. Phys. Chem. C* **2014,** *118* (46), 26902-26911.

15. Han, K. S.; Liu, G.; Zhou, X.; Medina, R. E.; Chen, P., How Does a Single Pt Nanocatalyst Behave in Two Different Reactions? A Single-Molecule Study. *Nano. Lett.* **2012,** *12* (3), 1253-1259.

16. Zhou, X.; Choudhary, E.; Andoy, N.; Zou, N.; Chen, P., Scalable Parallel Screening of Catalyst Activity at the Single-Particle Level and Subdiffraction Resolution. *ACS Catalysis* **2013,** *3* (7), 1448-1453.

17. Decan, M. R.; Impellizzeri, S.; Marin, M. L.; Scaiano, J. C., Copper Nanoparticle Heterogeneous Catalytic 'Click' Cycloaddition Confirmed by Single-Molecule Spectroscopy. *Nat. Commun.* **2014,** *5*, 4612.

18. Wang, B.; Durantini, J.; Decan, M. R.; Nie, J.; Lanterna, A. E.; Scaiano, J. C., From the Molecule to the Mole: Improving Heterogeneous Copper Catalyzed Click Chemistry Using Single Molecule Spectroscopy. *Chem. Comm.* **2017,** *53* (2), 328-331.

19. Kiel, A.; Kovacs, J.; Mokhir, A.; Krämer, R.; Herten, D.-P., Direct Monitoring of Formation and Dissociation of Individual Metal Complexes by Single-Molecule Fluorescence Spectroscopy. *Angew. Chem. Int. Ed.* **2007,** *46*, 3363-3366.

20. Esfandiari, N.; Wang, Y.; McIntire, T.; Blum, S., Real-Time Imaging of Platinum-Sulfur Ligand Exchange Reactions at the Single-Molecule Level Via a General Chemical Technique. *Organometallics* **2011,** *30* (11), 2901-2907.

21. Esfandiari, N. M.; Wang, Y.; Bass, J. Y.; Cornell, T. P.; Otte, D. A. L.; Cheng, M. H.; Hemminger, J. C.; McIntire, T. M.; Mandelshtam, V. A.; Blum, S. A., Single-Molecule Imaging of Platinum Ligand Exchange Reaction Reveals Reactivity Distribution. *J. Am. Chem. Soc.* **2010,** *132* (43), 15167-15169.

22. Esfandiari, N. M.; Wang, Y.; Bass, J. Y.; Blum, S. A., Deconvoluting Subensemble Chemical Reaction Kinetics of Platinum-Sulfur Ligand Exchange Detected with Single-Molecule Fluorescence Microscopy. *Inorg. Chem.* **2011,** *50* (19), 9201-3.

23. Feng, C.; Easter, Q. T.; Blum, S. A., Structure–Reactivity Studies, Characterization, and Transformation of Intermediates by Lithium Chloride in the Direct Insertion of Alkyl and Aryl Iodides to Metallic Zinc Powder. *Organometallics* **2017,** *36* (13), 2389-2396.

24. Feng, C.; Cunningham, D. W.; Easter, Q. T.; Blum, S. A., Role of LiCl in Generating Soluble Organozinc Reagents. *J. Am. Chem. Soc.* **2016,** *138* (35), 11156-11159.

25. Habuchi, S.; Onda, S.; Vacha, M., Molecular Weight Dependence of Emission Intensity and Emitting Sites Distribution within Single Conjugated Polymer Molecules. *Phys. Chem. Chem. Phys.* **2011,** *13* (5), 1743-1753.

26. Habuchi, S.; Onda, S.; Vacha, M., Mapping the Emitting Sites within a Single Conjugated Polymer Molecule. *Chem. Comm.* **2009,** (32), 4868-4870.

27. Habuchi, S.; Satoh, N.; Yamamoto, T.; Tezuka, Y.; Vacha, M., Multimode Diffusion of Ring Polymer Molecules Revealed by a Single-Molecule Study. *Angew. Chem.* **2010,** *122* (8), 1460-1463.

28. Habuchi, S.; Vacha, M., Conformation and Physics of Polymer Chains: A Single-Molecule Perspective. *NPG Asia Mater.* **2010,** *2* (4), 134-142.

29. Habuchi, S.; Fujiwara, S.; Yamamoto, T.; Vacha, M.; Tezuka, Y., Single-Molecule Study on Polymer Diffusion in a Melt State: Effect of Chain Topology. *Anal. Chem.* **2013,** *85* (15), 7369-7376.

30. Habuchi, S.; Fujita, H.; Michinobu, T.; Vacha, M., Twist Angle Plays an Important Role in Photophysical Properties of a Donor–Acceptor-Type Conjugated Polymer: A Combined Ensemble and Single-Molecule Study. *J. Phys. Chem. B* **2011,** *115* (49), 14404-14415.

31. Honmou, Y.; Hirata, S.; Komiyama, H.; Hiyoshi, J.; Kawauchi, S.; Iyoda, T.; Vacha, M., Single-Molecule Electroluminescence and Photoluminescence of Polyfluorene Unveils the Photophysics Behind the Green Emission Band. *Nat. Commun.* **2014,** *5*, 4666.

32. Sugimoto, T.; Ebihara, Y.; Ogino, K.; Vacha, M., Structure-Dependent Photophysics Studied in Single Molecules of Polythiophene Derivatives. *Chem. Phys. Chem.* **2007,** *8* (11), 1623-1628.

33. Bout, D. A. V.; Yip, W.-T.; Hu, D.; Fu, D.-K.; Swager, T. M.; Barbara, P. F., Discrete Intensity Jumps and Intramolecular Electronic Energy Transfer in the Spectroscopy of Single Conjugated Polymer Molecules. *Science* **1997,** *277* (5329), 1074-1077.

34. Gavranovic, G. T.; Csihony, S.; Bowden, N. B.; Hawker, C. J.; Waymouth, R. M.; Moerner, W. E.; Fuller, G. G., Well-Controlled Living Polymerization of Perylene-Labeled Polyisoprenes and Their Use in Single-Molecule Imaging. *Macromolecules* **2006,** *39* (23), 8121-8127.

35. Wöll, D.; Uji-i, H.; Schnitzler, T.; Hotta, J. i.; Dedecker, P.; Herrmann, A.; De Schryver, F. C.; Müllen, K.; Hofkens, J., Radical Polymerization Tracked by Single Molecule Spectroscopy. *Angew. Chem. Int. Ed.* **2008,** *47* (4), 783-787.

36. Tenopala-Carmona, F.; Fronk, S.; Bazan, G. C.; Samuel, I. D. W.; Penedo, J. C., Real-Time Observation of Conformational Switching in Single Conjugated Polymer Chains. *Science* **2018,** *4* (2).

37. Liu, C.; Kubo, K.; Wang, E.; Han, K.-S.; Yang, F.; Chen, G.; Escobedo, F. A.; Coates, G. W.; Chen, P., Single Polymer Growth Dynamics. *Science* **2017,** *358*, 352-355.

38. Esfandiari, N. M.; Blum, S. A., Homogeneous Vs Heterogeneous Polymerization Catalysis Revealed by Single-Particle Fluorescence Microscopy. *J. Am. Chem. Soc.* **2011,** *133* (45), 18145-18147.

39. Easter, Q. T.; Blum, S. A., Evidence for Dynamic Chemical Kinetics at Individual Molecular Ruthenium Catalysts. *Angew. Chem. Int. Ed.* **2018,** *57*, 1572-1575.

40. Easter, Q. T.; Blum, S. A., Kinetics of the Same Reaction Monitored over Nine Orders of Magnitude in Concentration: When Are Unique Subensemble and Single-Turnover Reactivity Displayed? *Angew. Chem. Int. Ed.* **2018,** *57*, 12027-12032.

41. Cordes, T.; Blum, S. A., Opportunities and Challenges in Single-Molecule and Single-Particle Fluorescence Microscopy for Mechanistic Studies of Chemical Reactions. *Nat. Chem.* **2013,** *5* (12), 993-9.

42. Jung, C.; Ruthardt, N.; Lewis, R.; Michaelis, J.; Sodeik, B.; Nolde, F.; Peneva, K.; Müllen, K.; Bräuchle, C., Photophysics of New Water-Soluble Terrylenediimide Derivatives and Applications in Biology. *Chem. Phys. Chem.* **2009,** *10*, 180-190.

43. Margineanu, A.; Hofkens, J.; Cotlet, M.; Habuchi, S.; Stefan, A.; Qu, J.; Kohl, C.; Müllen, K.; Vercammen, J.; Engelborghs, Y.; Gensch, T.; De Schryver, F. C., Photophysics of a Water-Soluble Rylene Dye: Comparison with Other Fluorescent Molecules for Biological Applications. *J. Phys. Chem. B* **2004,** *108*, 12242-12251.

44. Hensle, E.; Esfandiari, N.; Lim, S.; Blum, S., BODIPY Fluorophore Toolkit for Probing Chemical Reactivity and for Tagging Reactive Functional Groups. *Eur. J. Org. Chem.* **2014,** *2014* (16), 3347-3354.

45. Canham, S.; Bass, J.; Navarro, O.; Lim, S.; Das, N.; Blum, S., Toward the Single-Molecule Investigation of Organometallic Reaction Mechanisms: Single-Molecule Imaging of Fluorophore-Tagged Palladium(II) Complexes. *Organometallics* **2008,** *27* (10), 2172-2175.

46. Rybina, A.; Lang, C.; Wirtz, M.; Grussmayer, K.; Kurz, A.; Maier, F.; Schmitt, A.; Trapp, O.; Jung, G.; Herten, D.-P., Distinguishing Alternative Reaction Pathways by Single-Molecule Fluorescence Spectroscopy. *Angew. Chemie., Int. Ed.* **2013,** *52* (24), 6322-6325.

47. Upadhyay, S. P.; Lupo, K. M.; Marquard, A. N.; Ng, J. D.; Bates, D. M.; Goldsmith, R. H., Fluorescent Dendrimeric Molecular Catalysts Demonstrate Unusual Scaling Behavior at the Single-Molecule Level. *J. Phys. Chem. C* **2015,** *119* (34), 19703-19714.

48. Ng, J. D.; Upadhyay, S. P.; Marquard, A. N.; Lupo, K. M.; Hinton, D. A.; Padilla, N. A.; Bates, D. M.; Goldsmith, R. H., Single-Molecule Investigation of Initiation Dynamics of an Organometallic Catalyst. *J. Am. Chem. Soc.* **2016,** *138* (11), 3876-3883.

49. Lupo, K. M.; Hinton, D. A.; Ng, J. D.; Padilla, N. A.; Goldsmith, R. H., Probing Heterogeneity and Bonding at Silica Surfaces through Single-Molecule Investigation of Base-Mediated Linkage Failure. *Langmuir* **2016,** *32*, 9171-9179.

50. Hinton, D. A.; Ng, J. D.; Sun, J.; Lee, S.; Saikin, S. K.; Logsdon, J.; White, D. S.; Marquard, A. N.; Cavell, A. C.; Krasecki, V. K.; Knapper, K. A.; Lupo, K. M.; Wasielewski, M. R.; Aspuru-Guzik, A.; Biteen, J. S.; Gopalan, P.; Goldsmith, R. H., Mapping Forbidden Emission to Structure in Self-Assembled Organic Nanoparticles. *J. Am. Chem. Soc.* **2018,** *140* (46), 15827-15841.

51. Loudet, A.; Burgess, K., BODIPY Dyes and Their Derivatives: Syntheses and Spectroscopic Properties. *Chem. Rev.* **2007,** *107* (11), 4891-4932.

52. Ulrich, G.; Ziessel, R.; Harriman, A., The Chemistry of Fluorescent BODIPY Dyes: Versatility Unsurpassed. *Angew. Chemie., Int. Ed.* **2008,** *47* (7), 1184-1201.

53. Buschmann, V.; Weston, K. D.; Sauer, M., Spectroscopic Study and Evaluation of Red-Absorbing Fluorescent Dyes. *Bioconj. Chem.* **2003,** *14*, 195-204.

54. Guan, J.; Zhang, F.; Zhang, Y.; Liu, Z.; Wu, Y.; Xia, D., Synthesis, Structure and Optoelectronic Properties of Rigid 3D Tetraindeno-Fused Spirofluorene with Thioxanthene or Dioxothioxanthene Substitutes. *CrystEngComm* **2017,** *19*, 6752-6757.

55. Kowada, T.; Yamaguchi, S.; Ohe, K., Highly Fluorescent BODIPY Dyes Modulated with Spirofluorene Moieties. *Org. Lett.* **2010,** *12* (2), 296-299.

56. Simmons, H. E.; Fukunaga, T., Spiroconjugation. *J. Am. Chem. Soc.* **1967,** *89* (20), 5208-5215.

57. Hernan, P.; Delpino, C.; Ruizhitzky, E., Rhodium Complexes with Nitrogen-Donor Ligands Anchored on Silic Supports .1. Synthesis and Characterization. *Chem. Mater.* **1992,** *4* (1), 49-55.

58. Tamaki, R.; Chujo, Y., Synthesis of Poly(Vinyl Alcohol) Silica Gel Polymer Hybrids by In-Situ Hydrolysis Method. *Appl. Organomet. Chem.* **1998,** *12* (10-11), 755-762.

59. Brunel, D.; Cauvel, A.; Di Renzo, F.; Fajula, F.; Fubini, B.; Onida, B.; Garrone, E., Preferential Grafting of Alkoxysilane Coupling Agents on the Hydrophobic Portion of the Surface of Micelle-Templated Silica. *New J. Chem.* **2000,** *24* (10), 807-813.

60. Waddell, T. G.; Leyden, D. E.; Debello, M. T., The Nature of Organosilane to Silica-Surface Bonding. *J. Am. Chem. Soc.* **1981,** *103* (18), 5303-5307.

61. O'Brien, C. J.; Kantchev, E. A. B.; Valente, C.; Hadei, N.; Chass, G. A.; Lough, A.; Hopkinson, A. C.; Organ, M. G., Easily Prepared Air- and Moisture-Stable Pd-NHC (NHC = N-Heterocyclic Carbene) Complexes: A Reliable, User-Friendly, Highly Active Palladium Precatalyst for the Suzuki-Miyaura Reaction. *Chem. Eur. J.* **2006,** *12* (18), 4743-4748.

62. Schunk, T. C.; Burke, M. F., Bonded Phase Conformation and Solvation Effects on the Stationary-Phase Structure in Reversed-Phase Liquid-Chromatography. *J. Chromatogr. A* **1993,** *656* (1-2), 289-316.

63. Vandenberg, E. T.; Bertilsson, L.; Liedberg, B.; Uvdal, K.; Erlandsson, R.; Elwing, H.; Lundstrom, I., Structure of 3-Aminopropyl Triethoxy Silane on Silicon-Oxide. *J. Colloid Interface Sci.* **1991,** *147* (1), 103-118.

64. Witucki, G. L., A Silane Primer: Chemistry and Applications of Alkoxy Silanes. *J. Coat. Technol. Res.* **1993,** *65*, 57-57.

65. Nasielski, J.; Hadei, N.; Achonduh, G.; Kantchev, E. A.; O'Brien, C. J.; Lough, A.; Organ, M. G., Structure-Activity Relationship Analysis of Pd-PEPPSI Complexes in Cross-Couplings: A Close Inspection of the Catalytic Cycle and the Precatalyst Activation Model. *Chem. Eur. J.* **2010,** *16* (35), 10844-53.

66. Dash, C.; Shaikh, M. M.; Ghosh, P., Fluoride-Free Hiyama and Copper- and Amine-Free Sonogashira Coupling in Air in a Mixed Aqueous Medium by a Series of PEPPSI-Themed Precatalysts. *Eur. J. Inorg. Chem.* **2009,** *2009* (12), 1608-1618.

67. Kirschning, A.; Mennecke, K., Immobilization of Nhc-Bearing Palladium Catalysts on Polyvinylpyridine; Applications in Suzuki-Miyaura and Hartwig-Buchwald Reactions under Batch and Continuous-Flow Conditions. *Synthesis* **2008,** *2008* (20), 3267-3272.

68. Organ, M. G.; Abdel-Hadi, M.; Avola, S.; Dubovyk, I.; Hadei, N.; Kantchev, E. A.; O'Brien, C. J.; Sayah, M.; Valente, C., Pd-Catalyzed Aryl Amination Mediated by Well Defined, N-Heterocyclic Carbene (NHC)-Pd Precatalysts, Peppsi. *Chem. Eur. J.* **2008,** *14* (8), 2443-52.

69. Sayah, M.; Organ, M. G., Carbon-Sulfur Bond Formation of Challenging Substrates at Low Temperature by Using Pd-PEPPSI-Ipent. *Chem. Eur. J.* **2011,** *17* (42), 11719-22.

70. Larrosa, I.; Somoza, C.; Banquy, A.; Goldup, S. M., Two Flavors of PEPPSI-Ipr: Activation and Diffusion Control in a Single Nhc-Ligated Pd Catalyst? *Org. Lett.* **2011,** *31* (1), 146-149.

71. Phan, N. T. S.; Van Der Sluys, M.; Jones, C. W., On the Nature of the Active Species in Palladium Catalyzed Mizoroki–Heck and Suzuki–Miyaura Couplings – Homogeneous or Heterogeneous Catalysis, a Critical Review. *Adv. Synth. Catal.* **2006,** *348* (6), 609-679.

72. Martin-Fernandez, M. L.; Tynan, C. J.; Webb, S. E., A 'Pocket Guide' to Total Internal Reflection Fluorescence. *J. Microsc.* **2013,** *252* (1), 16-22.

73. Bigi, M. A.; White, M. C., Terminal Olefins to Linear Alpha,Beta-Unsaturated Ketones: Pd(II)/Hypervalent Iodine Co-Catalyzed Wacker Oxidation-Dehydrogenation. *J. Am. Chem. Soc.* **2013,** *135* (21), 7831-4.

74. Allen, D. P.; Wingerden, M. M. V.; Grubbs, R. H., Well-Defined Silica-Supported Olefin Metathesis Catalysts. *Org. Lett.* **2009,** *11* (6), 1261-1264.

75. Coperet, C.; Chabanas, M.; Saint-Arroman, R. P.; Basset, J.-M., Homogeneous and Heterogeneous Catalysis: Bridging the Gap through Surface Organometallic Chemistry. *Angew. Chem. Int. Ed.* **2003,** *42* (2), 156-181.

76. Bakker, J. M.; Langford, S. J.; Latter, M. J.; Lee, K. A.; Woodward, C. P., Template-Directed Assembly of a Macrocyclic Porphyrin Tetramer Using Olefin Metathesis. *Aust. J. Chem.* **2005,** *58*, 757-761.

77. Haedler, A. T.; Kreger, K.; Issac, A.; Wittmann, B.; Kivala, M.; Hammer, N.; Köhler, J.; Schmidt, H.-W.; Hildner, R., Long-Range Energy Transport in Single Supramolecular Nanofibres at Room Temperature. *Nature* **2015,** *523*, 196.

78. Caram, J. R.; Doria, S.; Eisele, D. M.; Freyria, F. S.; Sinclair, T. S.; Rebentrost, P.; Lloyd, S.; Bawendi, M. G., Room-Temperature Micron-Scale Exciton Migration in a Stabilized Emissive Molecular Aggregate. *Nano. Lett.* **2016,** *16* (11), 6808-6815.

79. Spano, F. C.; Mukamel, S., Superradiance in Molecular Aggregates. *J. Chem. Phys.* **1989,** *2*, 683-700.

80. Upadhyay, S. P.; Lupo, K. M.; Marquard, A. N.; Ng, J. D.; Bates, D. M.; Goldsmith, R. H., Fluorescent Dendrimeric Molecular Catalysts Demonstrate Unusual Scaling Behavior at the Single-Molecule Level. *J. Phys. Chem. C* **2015,** *119*, 19703-19714.

81. Hofkens, J.; Maus, M.; Gensch, T.; Vosch, T.; Cotlet, M.; Köhn, F.; Herrmann, A.; Müllen, K.; Schryver, F. D., Probing Photophysical Processes in Individual Multichromophoric Dendrimers by Single-Molecule Spectroscopy. *J. Am. Chem. Soc.* **2000,** *122*, 9278-9288.

82. Cotlet, M.; Gronheid, R.; Habuchi, S.; Stefan, A.; Barbafina, A.; Müllen, K.; Hofkens, J.; Schryver, F. C. D., Intramolecular Directional Förster Resonance Energy Transfer at the Single-Molecule Level in a Dendritic System. *J. Am. Chem. Soc.* **2003,** *125*, 13609-13617.

83. Wasielewski, M. R., Self-Assembly Strategies for Integrating Light Harvesting and Charge Separation in Artificial Photosynthetic Systems. *Acc. Chem. Res.* **2009,** *42* (12), 1910-1921.

84. Liess, A.; Lv, A.; Arjona-Esteban, A.; Bialas, D.; Krause, A.-M.; Stepanenko, V.; Stolte, M.; Würthner, F., Exciton Coupling of Merocyanine Dyes from H- to J-Type in the Solid State by Crystal Engineering. *Nano. Lett.* **2017,** *17* (3), 1719-1726.

85. Wu, H.; Xue, L.; Shi, Y.; Chen, Y.; Li, X., Organogels Based on J- and H-Type Aggregates of Amphiphilic Perylenetetracarboxylic Diimides. *Langmuir* **2011,** *27* (6), 3074-3082.

86. Turro, N. J.; Ramamurthy, V.; Scaiano, J. C., *Principles of Molecular Photochemistry*. University Science Books: Sausalito, California, 2009.

87. Peng, H.-S.; Chiu, D. T., Soft Fluorescent Nanomaterials for Biological and Biomedical Imaging. *Chem. Soc. Rev.* **2015,** *44*, 4699-4722.

88. Wu, C.; Jin, Y.; Schneider, T.; Burnham, D. R.; Smith, P. B.; Chiu, D. T., Ultrabright and Bioorthogonal Labeling of Cellular Targets Using Semiconducting Polymer Dots and Click Chemistry. *Angew. Chem. Int. Ed.* **2010,** *49*, 9436 –9440.

89. O'Neill, M.; Kelly, S. M., Ordered Materials for Organic Electronics and Photonics. *Adv. Mater.* **2011,** *23* (5), 566-84.

90. Babu, S. S.; Prasanthkumar, S.; Ajayaghosh, A., Self-Assembled Gelators for Organic Electronics. *Angew. Chem. Int. Ed.* **2012,** *51* (8), 1766-76.

91. Morseth, Z. A.; Wang, L.; Puodziukynaite, E.; Leem, G.; Gilligan, A. T.; Meyer, T. J.; Schanze, K. S.; Reynolds, J. R.; Papanikolas, J. M., Ultrafast Dynamics in Multifunctional Ru(II)-Loaded Polymers for Solar Energy Conversion. *Acc. Chem. Res.* **2015,** *48*, 818-827.

92. Schwartz, E.; Le Gac, S.; Cornelissen, J. J. L. M.; Nolte, R. J. M.; Rowan, A. E., Macromolecular Multi-Chromophoric Scaffolding. *Chem. Soc. Rev.* **2010,** *39*.

93. Trenor, S. R.; Shultz, A. R.; Love, B. J.; Long, T. E., Coumarins in Polymers: From Light Harvesting to Photo-Cross-Linkable Tissue Scaffolds. *Chem. Rev.* **2004,** *104*, 3059-3077.

94. Rong, Y.; Wu, C.; Yu, J.; Zhang, X.; Ye, F.; Zeigler, M.; Gallina, M. E.; Wu, I. C.; Zhang, Y.; Chan, Y.-H.; Sun, W.; Uvdal, K.; Chiu, D. T., Multicolor Fluorescent Semiconducting Polymer Dots with Narrow Emissions and High Brightness. *ACS Nano* **2013,** *7* (1), 376-384.

95. Alemdaroglu, F. E.; Alexander, S. C.; Ji, D.; Prusty, D. K.; Börsch, M.; Herrmann, A., Poly(BODIPY)s: A New Class of Tunable Polymeric Dyes. *Macromolecules* **2009,** *42*, 6529–6536.

96. Nagai, A.; Chujo, Y., Aromatic Ring-Fused Bodipy-Based Conjugated Polymers Exhibiting Narrow near-Infrared Emission Bands. *Macromolecules* **2009,** *43*, 193-200.

97. Thivierge, C.; Loudet, A.; Burgess, K., Brilliant Bodipy-Fluorene Copolymers with Dispersed Absorption and Emission Maxima. *Macromolecules* **2011,** *44*, 4012-4015.

98. Peterson, J. J.; Krauss, T. D., Photobrightening and Photodarkening in PbS Quantum Dots. *Phys. Chem. Chem. Phys.* **2006,** *8* (33), 3851.

99. Tice, D. B.; Frederick, M. T.; Chang, R. P. H.; Weiss, E. A., Electron Migration Limits the Rate of Photobrightening in Thin Films of CdSe Quantum Dots in a Dry N_2(g) Atmosphere. *J. Phys. Chem. C* **2011,** *115* (9), 3654-3662.

100. Banal, J. L.; White, J. M.; Ghiggino, K. P.; Wong, W. W. H., Concentrating Aggregation-Induced Fluorescence in Planar Waveguides: A Proof-of-Principle. *Sci. Rep.* **2014,** *4*, 5.

101. Choi, T.-L.; Grubbs, R. H., Controlled Living Ring-Opening-Metathesis Polymerization by a Fast-Initiating Ruthenium Catalyst. *Angew. Chem. Int. Ed.* **2003,** *42* (15), 1743-1746.

102. Parry, A. V. S.; Lu, K.; Tate, D. J.; Urasinska-Wojcik, B.; Quintero, D. C.-.; Majewski, L. A.; Turner, M. L., Trichlorosilanes as Anchoring Groups for Phenylene-Thiophene Molecular Monolayer Field Effect Transistors. *Adv. Func. Mater.* **2014,** *24* (42), 6677-6683.

103. Horak, E. H.; Rea, M. T.; Heylman, K. D.; Gelbwaser-Klimovsky, D.; Saikin, S. K.; Thompson, B. J.; Kohler, D. D.; Knapper, K. A.; Wei, W.; Pan, F.; Gopalan, P.; Wright, J. C.; Aspuru-Guzik, A.; Goldsmith, R. H., Exploring Electronic Structure and Order in Polymers Via Single-Particle Microresonator Spectroscopy. *Nano. Lett.* **2018,** *18* (3), 1600-1607.

104. Vogelsang, J.; Adachi, T.; Brazard, J.; Vanden Bout, D. A.; Barbara, P. F., Self-Assembly of Highly Ordered Conjugated Polymer Aggregates with Long-Range Energy Transfer. *Nature Mat.* **2011,** *10* (12), 942-6.

105. Bolinger, J. C.; Traub, M. C.; Brazard, J.; Adachi, T.; Barbara, P. F.; Vanden Bout, D. A., Conformation and Energy Transfer in Single Conjugated Polymers. *Acc. Chem. Res.* **2012,** *45* (11), 1992-2001.

106. Vogelsang, J.; Lupton, J. M., Solvent Vapor Annealing of Single Conjugated Polymer Chains: Building Organic Optoelectronic Materials from the Bottom Up. *J. Phys. Chem. Lett.* **2012,** *3*, 1503-1513.

107. Weston, K. D.; Dyck, M.; Tinnefeld, P.; Müller, C.; Herten, D. P.; Sauer, M., Measuring the Number of Independent Emitters in Single-Molecule Fluorescence Images and Trajectories Using Coincident Photons. *Anal. Chem.* **2002,** *74* (20), 5342-5349.

108. De Schryver, F. C.; Vosch, T.; Cotlet, M.; Van der Auweraer, M.; Müllen, K.; Hofkens, J., Energy Dissipation in Multichromophoric Single Dendrimers. *Acc. Chem. Res.* **2005,** *38* (7), 514-522.

109. Yang, J.; Cho, S.; Yoo, H.; Park, J.; Li, W.-S.; Aida, T.; Kim, D., Control of Molecular Structures and Photophysical Properties of Zinc(II) Porphyrin Dendrimers Using Bidentate Guests: Utilization of Flexible Dendrimer Structures as a Controllable Mold. *J. Phys. Chem. A.* **2008,** *112* (30), 6869-6876.

110. Noriega, R.; Barnard, E. S.; Ursprung, B.; Cotts, B. L.; Penwell, S. B.; Schuck, P. J.; Ginsberg, N. S., Uncovering Single-Molecule Photophysical Heterogeneity of Bright, Thermally Activated Delayed Fluorescence Emitters Dispersed in Glassy Hosts. *J. Am. Chem. Soc.* **2016,** *138* (41), 13551-13560.

111. Cotlet, M.; Gronheid, R.; Habuchi, S.; Stefan, A.; Barbafina, A.; Müllen, K.; Hofkens, J.; De Schryver, F. C., Intramolecular Directional Förster Resonance Energy Transfer at the Single-Molecule Level in a Dendritic System. *J. Am. Chem. Soc.* **2003,** *125* (44), 13609-17.

112. Huser, T.; Yan, M.; Rothberg, L. J., Single Chain Spectroscopy of Conformational Dependence of Conjugated Polymer Photophysics. *Proc. Natl. Acad. Sci. U. S. A.* **2000,** *97* (21), 11187-11191.

113. Ebihara, Y.; Vacha, M., Relating Conformation and Photophysics in Single MEH-PPV Chains. *J. Phys. Chem. B* **2008,** *112*, 12575-12578.

114. Barbara, P. F.; Gesquiere, A. J.; Park, S.-J.; Lee, Y. J., Single-Molecule Spectroscopy of Conjugated Polymers. *Acc. Chem. Res.* **2005,** *38* (7), 602-610.

115. Van Munster, E. B.; Kremers, G. J.; Adjobo-Hermans, M. J. W.; Gadella Jr, T. W. J., Fluorescence Resonance Energy Transfer (FRET) Measurement by Gradual Acceptor Photobleaching. *J. Microsc.* **2005,** *218* (3), 253-262.

116. Wang, X.; Groff, L. C.; McNeill, J. D., Photoactivation and Saturated Emission in Blended Conjugated Polymer Nanoparticles. *Langmuir* **2013,** *29* (45), 13925-31.

117. Huisgen, R.; Ooms, P. H. J.; Mingin, M.; Allinger, N. L., Exceptional Reactivity of the Bicyclo[2.2.1]Heptene Double Bond. *J. Am. Chem. Soc.* **1980,** *102*, 3951-3953.

118. Rondan, N. G.; Paddon-Row, M. N.; Caramella, P.; Mareda, J.; Mueller, P. H.; Houk, K. N., Origin of Huisgen's Factor "X": Staggering of Allylic Bonds Promotes Anomalously Rapid Exo Attack on Norbornenes. *J. Am. Chem. Soc.* **1982,** *104* (18), 4974-4976.

119. Braun, M.; Christl, M.; Peters, E.-M.; Peters, K., Photochemical Reactions of Chloranil with Norbornene,† Bicyclo[2.1.1]Hex-2-Ene and Cyclopentene. A Novel Intermolecular Photocycloaddition. *J. Chem. Soc., Perkins Trans. 1* **1999**, 2813-2820.

120. Saikin, S. K.; Eisfeld, A.; Valleau, S.; Aspuru-Guzik, A., Photonics Meets Excitonics: Natural and Artificial Molecular Aggregates. *Nanophotonics* **2013,** *2* (1).

121. Saikin, S. K.; Shakirov, M. A.; Kreisbeck, C.; Peskin, U.; Proshin, Y. N.; Aspuru-Guzik, A., On the Long-Range Exciton Transport in Molecular Systems: The Application to H-Aggregated Heterotriangulene Chains. *J. Phys. Chem. C* **2017,** *121* (45), 24994-25002.

122. Spano, F. C., The Spectral Signatures of Frenkel Polarons in H- and J-Aggregates. *Acc. Chem. Res.* **2010,** *43* (3), 429-439.

123. Spano, F. C.; Silva, C., H- and J-Aggregate Behavior in Polymeric Semiconductors. *Ann. Rev. Phys. Chem.* **2014,** *65*, 477-500.

124. Panzer, F.; Sommer, M.; Bässler, H.; Thelakkat, M.; Köhler, A., Spectroscopic Signature of Two Distinct H-Aggregate Species in Poly(3-Hexylthiophene). *Macromolecules* **2015,** *48* (5), 1543-1553.

125. Clark, J.; Silva, C.; Friend, R. H.; Spano, F. C., Role of Intermolecular Coupling in the Photophysics of Disordered Organic Semiconductors: Aggregate Emission in Regioregular Polythiophene. *Phys. Rev. Lett.* **2007,** *98* (20), 206406.

126. Rösch, U.; Yao, S.; Wortmann, R.; Würthner, F., Fluorescent H-Aggregates of Merocyanine Dyes. *Angew. Chem.* **2006,** *118* (42), 7184-7188.

127. Peyratout, C.; Daehne, L., Aggregation of Thiacyanine Derivatives on Polyelectrolytes. *Phys. Chem. Chem. Phys.* **2002,** *4* (13), 3032-3039.

128. Chakraborty, S.; Debnath, P.; Dey, D.; Bhattacharjee, D.; Hussain, S. A., Formation of Fluorescent H-Aggregates of a Cyanine Dye in Ultrathin Film and Its Effect on Energy Transfer. *J. Photochem. Photobiol. A* **2014,** *293*, 57-64.

129. Chaudhuri, D.; Li, D.; Che, Y.; Shafran, E.; Gerton, J. M.; Zang, L.; Lupton, J. M., Enhancing Long-Range Exciton Guiding in Molecular Nanowires by H-Aggregation Lifetime Engineering. *Nano. Lett.* **2011,** *11* (2), 488-92.

130. Margulies, E. A.; Shoer, L. E.; Eaton, S. W.; Wasielewski, M. R., Excimer Formation in Cofacial and Slip-Stacked Perylene-3,4:9,10-Bis(Dicarboximide) Dimers on a Redox-Inactive Triptycene Scaffold. *Phys. Chem. Chem. Phys.* **2014,** *16* (43), 23735-42.

131. Mandal, A. K.; Pal, M. K., Strong Fluorescence Emissions by H-Aggregates of the Dye Thiacyanine in the Presence of the Surfactant Aerosol-OT. *Chem. Phys.* **2000,** *253* (1), 115-124.

132. Hirose, T.; Tsunoi, Y.; Fujimori, Y.; Matsuda, K., Fluorescence Enhancement of Covalently Linked 1-Cyano-1,2-Diphenylethene Chromophores with Naphthalene-1,8-Diyl Linker Units: Analysis Based on Kinetic Constants. *Chem. Eur. J.* **2015,** *21* (4), 1637-44.

133. Verma, P.; Pal, H., Intriguing H-Aggregate and H-Dimer Formation of Coumarin-481 Dye in Aqueous Solution as Evidenced from Photophysical Studies. *J. Phys. Chem. A.* **2012,** *116* (18), 4473-84.

134. Qian, H.; Cousins, M. E.; Horak, E. H.; Wakefield, A.; Liptak, M. D.; Aprahamian, I., Suppression of Kasha's Rule as a Mechanism for Fluorescent Molecular Rotors and Aggregation-Induced Emission. *Nat. Chem.* **2017,** *9* (1), 83-87.

135. Bayda, M.; Dumoulin, F.; Hug, G. L.; Koput, J.; Gorniak, R.; Wojcik, A., Fluorescent H-Aggregates of an Asymmetrically Substituted Mono-Amino Zn(II) Phthalocyanine. *Dalton Trans.* **2017,** *46* (6), 1914-1926.

136. Itoh, T., Fluorescence and Phosphorescence from Higher Excited States of Organic Molecules. *Chem. Rev.* **2012,** *112* (8), 4541-68.

137. Mahesh, S.; Gopal, A.; Thirumalai, R.; Ajayaghosh, A., Light-Induced Ostwald Ripening of Organic Nanodots to Rods. *J. Am. Chem. Soc.* **2012,** *134* (17), 7227-30.

138. Lim, S. H.; Bjorklund, T. G.; Spano, F. C.; Bardeen, C. J., Exciton Delocalization and Superradiance in Tetracene Thin Films and Nanoaggregates. *Phys. Rev. Lett.* **2004,** *92* (10), 107402.

139. Yang, Z.; Mao, Z.; Xie, Z.; Zhang, Y.; Liu, S.; Zhao, J.; Xu, J.; Chi, Z.; Aldred, M. P., Recent Advances in Organic Thermally Activated Delayed Fluorescence Materials. *Chem. Soc. Rev.* **2017,** *46* (3), 915-1016.

140. Shufang Liu, Y. C., Xiaohui He, Lie Chen, Weihua Zhou, Stable Crosslinked Vinyl-Addition-Type Polynorbornene Graft Copolymer Proton-Exchange Membranes. *J. Appl. Polym. Sci.* **2011,** *121*, 1166-1175.

141. Jacinta M. Bakker, S. J. L., Melissa J. Latter, Katrina A. Lee, Clint P.Woodward, Template-Directedassembly of a Macrocyclic Porphyrintetramer Using Olefin Metathesis. *Aust. J. Chem.* **2005,** *58*, 757-761.

142. Kendra Getty, M. U. D.-J., Pierre Kennepohl, Assignment of Pre-Edge Features in the Ru K-Edge X-Ray Absorption Spectra of Organometallic Ruthenium Complexes. *Inorg. Chim. Acta* **2008,** *361* (4), 1059-1065.

143. Zhang, J.-H.; Chung, T. D. Y.; Oldenburg, K. R., A Simple Statistical Parameter for Use in Evaluation and Validation of High Throughput Screening Assays. *J. Biomol. Screen.* **1999,** *4* (2), 67-73.

144. Inglese, J.; Auld, D. S.; Jadhav, A.; Johnson, R. L.; Simeonov, A.; Yasgar, A.; Zheng, W.; Austin, C. P., Quantitative High-Throughput Screening: A Titration-Based Approach That Efficiently Identifies Biological Activities in Large Chemical Libraries. *Proc. Natl. Acad. Sci. U. S. A.* **2006,** *103* (31), 11473-11478.

145. Reetz, M. T.; Becker, M. H.; Klein, H.-W.; Stöckigt, D., A Method for High-Throughput Screening of Enantioselective Catalysts. *Angew. Chem. Int. Ed.* **1999,** *38* (12), 1758-1761.

146. Murphy, V.; Volpe Jr., A. F.; Weinberg, W. H., High-Throughput Approaches to Catalyst Discovery. *Curr. Opin. Chem. Biol.* **2003,** *7*, 427-433.

147. Reetz, M. T., New Methods for the High-Throughput Screening of Enantioselective Catalysts and Biocatalysts. *Angew. Chem. Int. Ed.* **2002,** *41* (8), 1335-1338.

148. Shaughnessy, K. H.; Kim, P.; Hartwig, J. F., A Fluorescence-Based Assay for High-Throughput Screening of Coupling Reactions. Application to Heck Chemistry. *J. Am. Chem. Soc.* **1999,** *121*, 2123-2132.

149. Boussie, T. R.; Diamond, G. M.; Goh, C.; Hall, K. A.; LaPointe, A. M.; Leclerc, M.; Lund, C.; Murphy, V.; Shoemaker, J. A. W.; Tracht, U.; Turner, H.; Zhang, J.; Uno, T.; Rosen, R. K.; Stevens, J. C., A Fully Integrated High-Throughput Screening Methodology for the Discovery of New Polyolefin Catalysts: Discovery of a New Class of High Temperature Single-Site Group (IV) Copolymerization Catalysts. *J. Am. Chem. Soc.* **2003,** *125*, 4306-4317.

150. Krska, S. W.; DiRocco, D. A.; Dreher, S. D.; Shevlin, M., The Evolution of Chemical High-Throughput Experimentation to Address Challenging Problems in Pharmaceutical Synthesis. *Acc. Chem. Res.* **2017,** *50*, 2976-2985.

151. Shevlin, M., Practical High-Throughput Experimentation for Chemists. *ACS Med. Chem. Lett.* **2017,** *8*, 601-607.

152. Reetz, M. T.; Kühling, K. M.; Deege, A.; Hinrichs, H.; Belder, D., Super-High-Throughput Screening of Enantioselective Catalysts by Using Capillary Array Electrophoresis. *Angew. Chem. Int. Ed.* **2000,** *39* (21), 3891-3893.

153. Zhong, L., *High Throughput Analysis in Support of Process Chemistry and Formulation Research and Development in the Pharmaceutical Industry*. CRC Press: Boca Raton, FL, 2009.

154. Herrera, B. T.; Pilicer, S. L.; Anslyn, E. V.; Joyce, L. A.; Wolf, C., Optical Analysis of Reaction Yield and Enantiomeric Excess: A New Paradigm Ready for Prime Time. *J. Am. Chem. Soc.* **2018,** *140*, 10385-10401.

155. Stambuli, J. P.; Stauffer, S. R.; Shaughnessy, K. H.; Hartwig, J. F., Screening of Homogeneous Catalysts by Fluorescence Resonance Energy Transfer. Identification of Catalysts for Room-Temperature Heck Reactions. *J. Am. Chem. Soc.* **2001,** *123*, 2677-2678.

156. Stauffer, S. R.; Hartwig, J. F., Fluorescence Resonance Energy Transfer (FRET) as a High-Throughput Assay for Coupling Reactions. Arylation of Amines as a Case Study. *J. Am. Chem. Soc.* **2003,** *125*, 6977-6985.

157. Shabbir, S. H.; Regan, C. J.; Anslyn, E. V., A General Protocol for Creating High-Throughput Screening Assays for Reaction Yield and Enantiomeric Excess Applied to Hydrobenzoin. *Proc. Natl. Acad. Sci. U. S. A.* **2009,** *106* (26), 10487–10492.

158. Bentley, K. W.; Zhang, P.; Wolf, C., Miniature High-Throughput Chemosensing of Yield, Ee, and Absolute Configuration from Crude Reaction Mixtures. *Sci. Adv.* **2016,** *2* (2), 1-8.

159. Ready, J. M.; Jacobsen, E. N., Asymmetric Catalytic Synthesis of α-Aryloxy Alcohols: Kinetic Resolution of Terminal Epoxides Via Highly Enantioselective Ring Opening with Phenols. *J. Am. Chem. Soc.* **1999,** *121*, 6086-6087.

160. Zweig, J. E.; Kim, D. E.; Newhouse, T. R., Methods Utilizing First-Row Transition Metals in Natural Product Total Synthesis. *Chem. Rev.* **2017,** *117*, 11680-11752.

161. Rouhi, A. M., Chiral Chemistry. *C&EN News* 2004, pp 47-62.

162. Huang, J.; Su, J.-H.; Tian, H., The Development of Anthracene Derivatives for Organic Light-Emitting Diodes. *J. Mater. Chem.* **2012**, 10977-10989.

163. Hein, S. J.; Lehnerr, D.; Arslan, H.; Uribe-Romo, F. J.; Dichtel, W. R., Alkyne Benzannulation Reactions for the Synthesis of Novel Aromatic Architectures. *Acc. Chem. Res.* **2017,** *50*, 2776-2788.

164. Connon, S. J.; Blechert, S., Recent Developments in Olefin Cross-Metathesis. *Angew. Chem. Int. Ed.* **2003,** *42*, 1900-1923.

165. Berlman, I. B., *Handbook of Fluorescence Spectra of Aromatic Molecules*. Elsevier: N.Y., 1971.

166. Suzaki, Y.; Tsuchido, Y.; Osakada, K., Tweezers-Like Aromatic Molecules and Their Luminescent Properties Depending on the Structures. *Tetrahedron Lett.* **2011,** *52*, 3883–3885.

167. Hu, J.-Y.; Pu, Y.-J.; Satoh, F.; Kawata, S.; Katagiri, H.; Sasabe, H.; Kido, J., Bisanthracene-Based Donor–Acceptor-Type Light-Emitting Dopants: Highly Effi Cient Deep-Blue Emission in Organic Light-Emitting Devices *Adv. Func. Mater.* **2014,** *24*, 2064-2071.

168. Amat-Guerri, F.; Liras, M.; Carrascoso, M. L.; Sastre, R., Methacrylate-Tethered Analogs of the Laser Dye PM567—Synthesis, Copolymerization with Methyl Methacrylate and Photostability of the Copolymers. *Photochem. Photobiol.* **2003,** *77* (6), 577-584.

169. Mahmood, Z.; Zhao, J., Thiol-Activatable Triplet−Triplet Annihilation Upconversion with Maleimide-Perylene as the Caged Triplet Acceptor/Emitter. *J. Org. Chem.* **2016,** *81*, 587-594.

170. Wee, X. K.; Yeo, W. K.; Zhang, B.; Tan, V. B. C.; Lim, K. M.; Tay, T. E.; Go, M.-L., Synthesis and Evaluation of Functionalized Isoindigos as Antiproliferative Agents. *Bioorganic Med. Chem.* **2009,** *17*, 7562-7671.

171. Goh, M.; Park, J.; Han, Y.; Ahn, S.; Akagi, K., Chirality Transfer from Atropisomeric Chiral Inducers to Nematic and Smectic Liquid Crystals – Synthesis and Characterization of Di- and Tetra-Substituted Axially Chiral Binaphthyl Derivatives. *J. Mater. Chem.* **2012,** *22* 25011-25018.

NMR Spectra

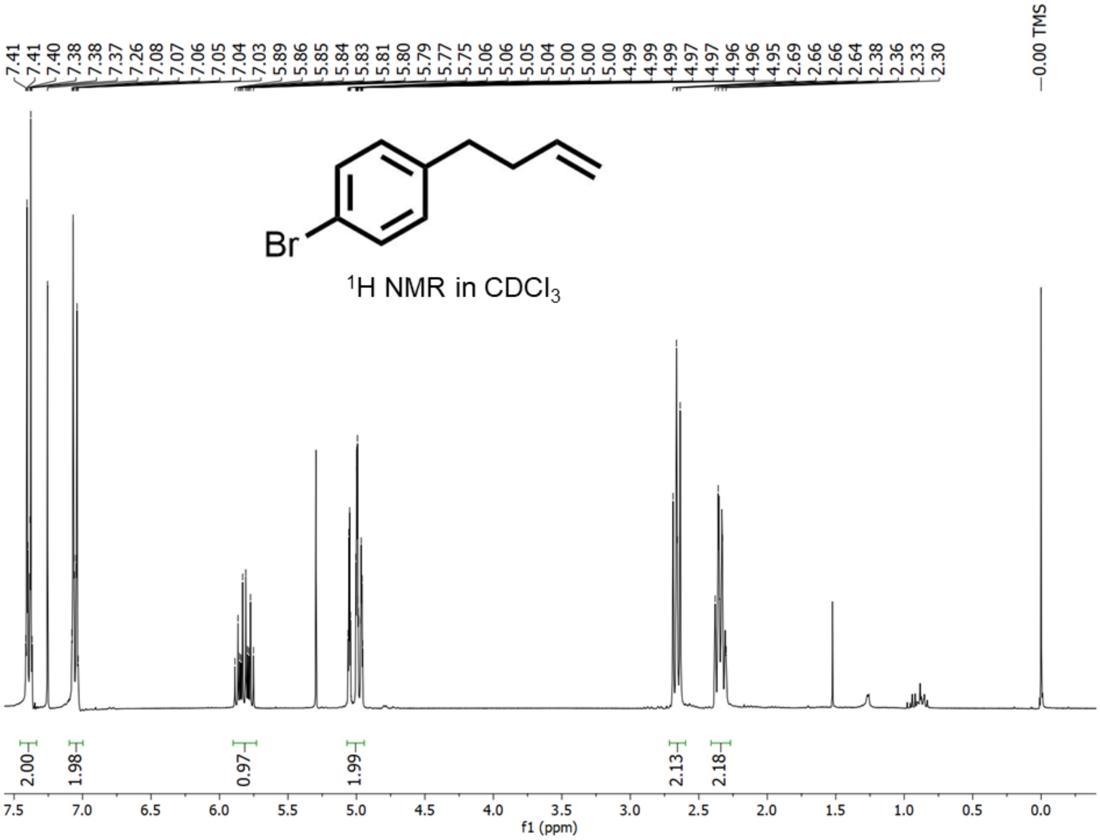
7.41
7.41
7.40
7.38
7.38
7.37
7.26
7.08
7.07
7.06
7.05
7.04
7.03
5.89
5.86
5.85
5.84
5.83
5.81
5.80
5.79
5.77
5.75
5.06
5.06
5.05
5.04
5.00
5.00
4.99
4.99
4.99
4.97
4.97
4.96
4.95
2.69
2.66
2.66
2.64
2.38
2.36
2.33
2.30
−0.00 TMS
Br
^{1}H NMR in CDCl$_3$
2.00
1.98
0.97
1.99
2.13
2.18
7.5
7.0
6.5
6.0
5.5
5.0
4.5
4.0
3.5
3.0
2.5
2.0
1.5
1.0
0.5
0.0
f1 (ppm)

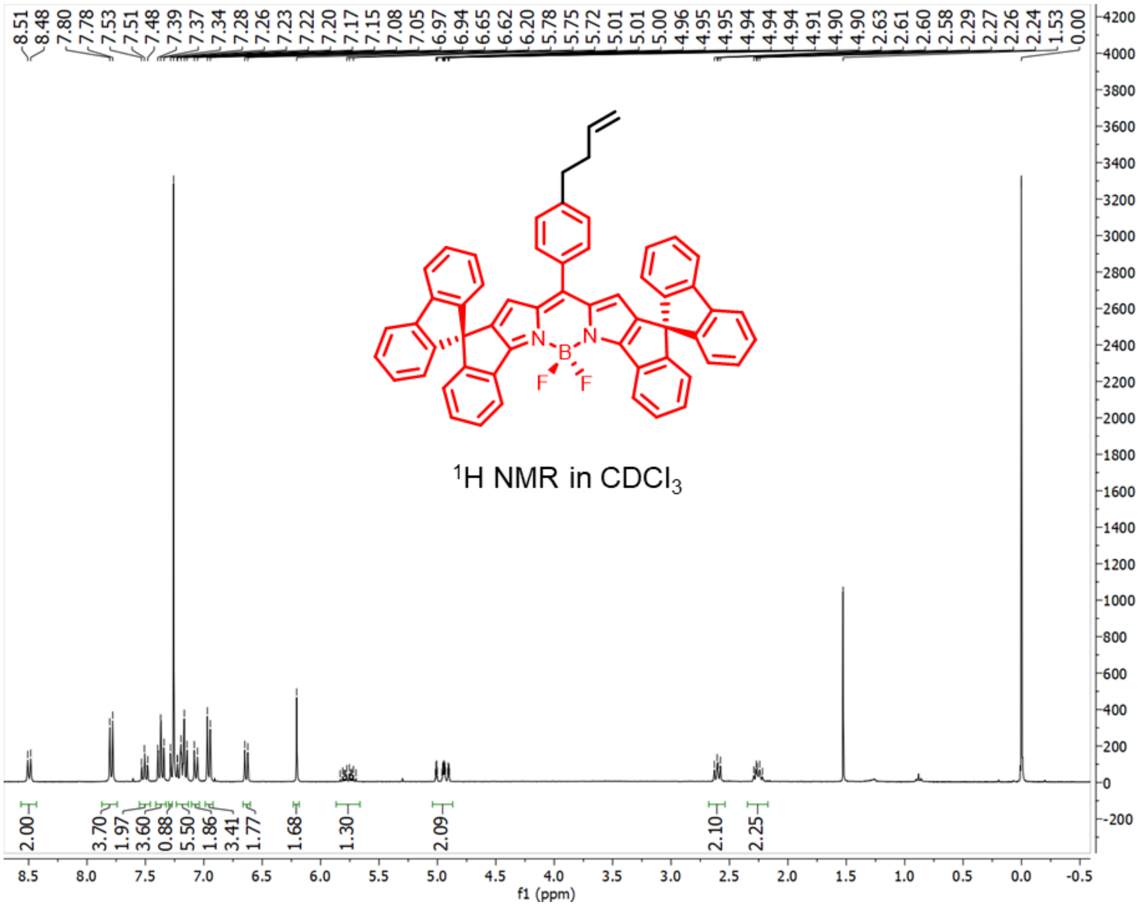
8.51
8.48
7.80
7.78
7.53
7.51
7.48
7.39
7.37
7.34
7.28
7.26
7.23
7.22
7.20
7.17
7.15
7.08
7.05
6.97
6.94
6.65
6.62
6.20
5.78
5.75
5.72
5.01
5.00
4.96
4.95
4.95
4.94
4.94
4.94
4.91
4.90
2.63
2.61
2.60
2.58
2.29
2.27
2.26
2.24
1.53
0.00
N
B
N
F
F
^{1}H NMR in CDCl$_3$
2.00
3.70
1.97
3.60
0.88
5.50
1.86
3.41
1.77
1.68
1.30
2.09
2.10
2.25
f1 (ppm)

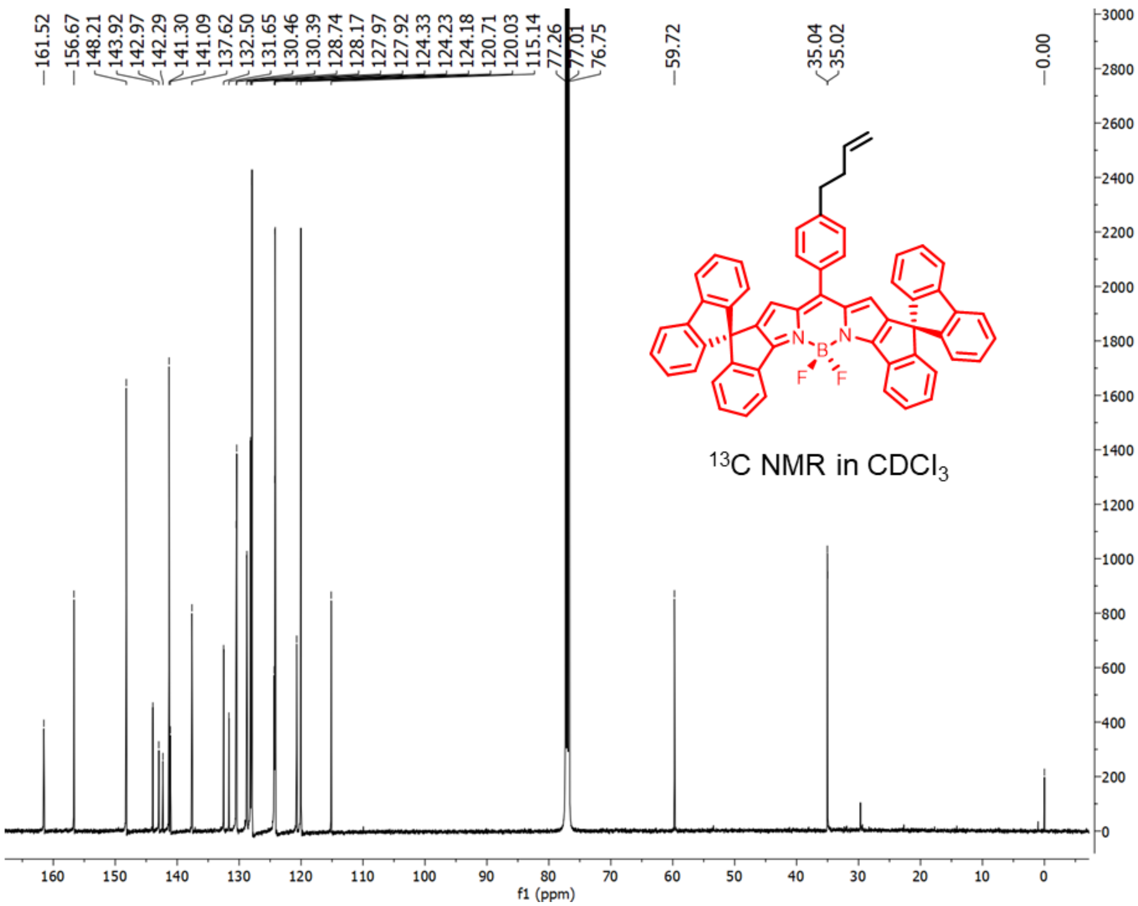
161.52
156.67
148.21
143.92
142.97
142.29
141.30
141.09
137.62
132.50
131.65
130.46
130.39
128.74
128.17
127.97
127.92
124.33
124.23
124.18
120.71
120.03
115.14
77.26
77.01
76.75
59.72
35.04
35.02
0.00
N
B
N
F
F
^{13}C NMR in CDCl$_3$
3000
2800
2600
2400
2200
2000
1800
1600
1400
1200
1000
800
600
400
200
0
160
150
140
130
120
110
100
90
80
70
60
50
40
30
20
10
0
f1 (ppm)

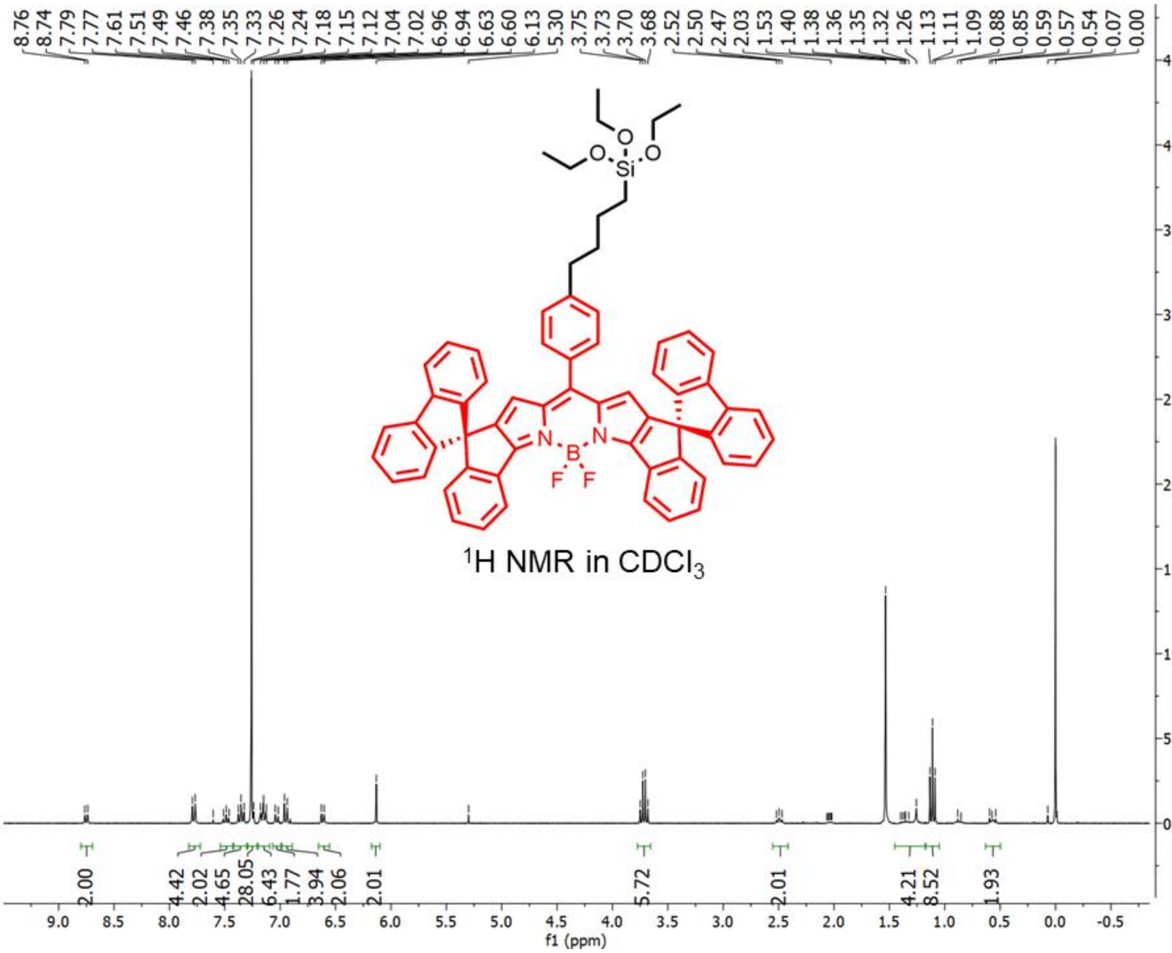
8.76
8.74
7.79
7.77
7.61
7.51
7.49
7.46
7.38
7.35
7.33
7.26
7.24
7.18
7.15
7.12
7.04
7.02
6.96
6.94
6.63
6.60
6.13
5.30
3.75
3.73
3.70
3.68
2.52
2.50
2.47
2.03
1.53
1.40
1.38
1.36
1.35
1.32
1.26
1.13
1.11
1.09
0.88
0.85
0.59
0.57
0.54
0.07
0.00
Si
O
N
B
F
¹H NMR in CDCl₃
4500
4000
3500
3000
2500
2000
1500
1000
500
0
2.00
4.42
2.02
4.65
28.05
6.43
1.77
3.94
2.06
2.01
5.72
2.01
4.21
8.52
1.93
9.0
8.5
8.0
7.5
7.0
6.5
6.0
5.5
5.0
4.5
4.0
3.5
3.0
2.5
2.0
1.5
1.0
0.5
0.0
-0.5
f1 (ppm)

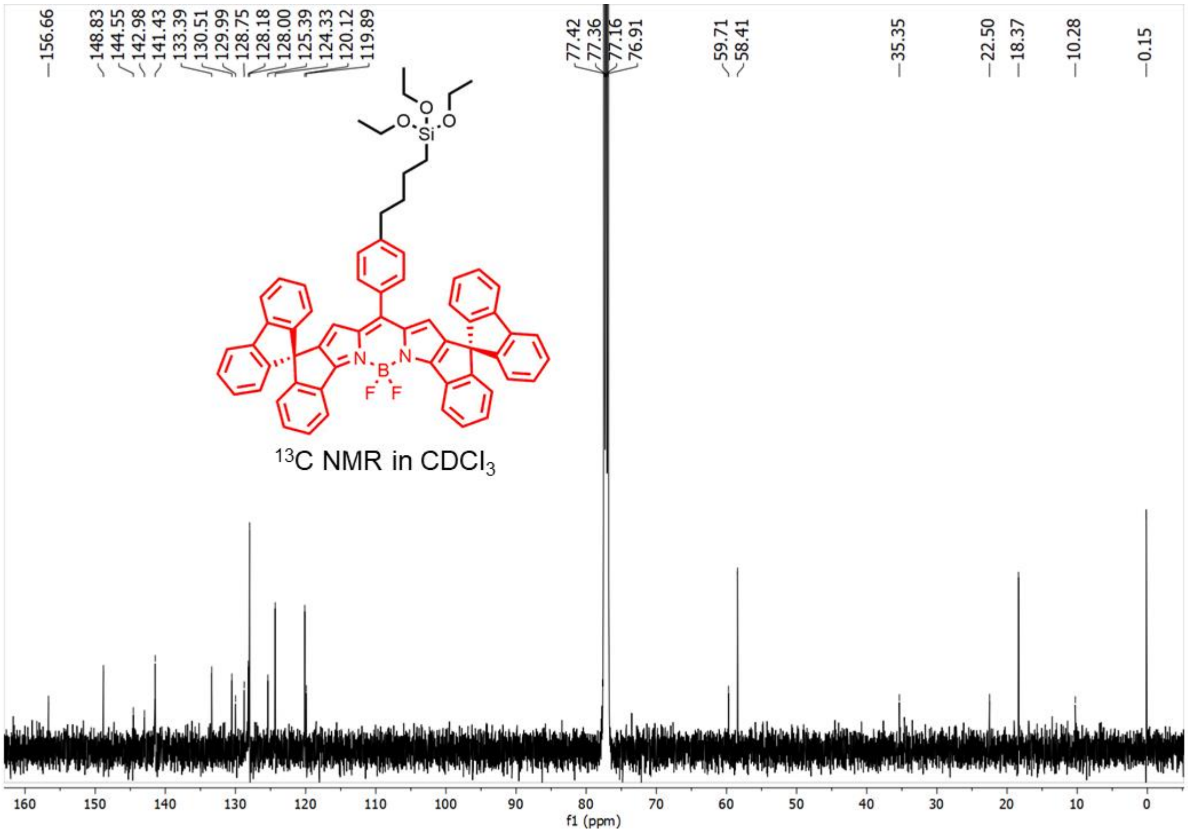
156.66
148.83
144.55
142.98
141.43
133.39
130.51
129.99
128.75
128.18
128.00
125.39
124.33
120.12
119.89
77.42
77.36
77.16
76.91
59.71
58.41
35.35
22.50
18.37
10.28
0.15
O
O
O
Si
N
B
N
F
F
^{13}C NMR in CDCl$_3$
160
150
140
130
120
110
100
90
80
70
60
50
40
30
20
10
0
f1 (ppm)

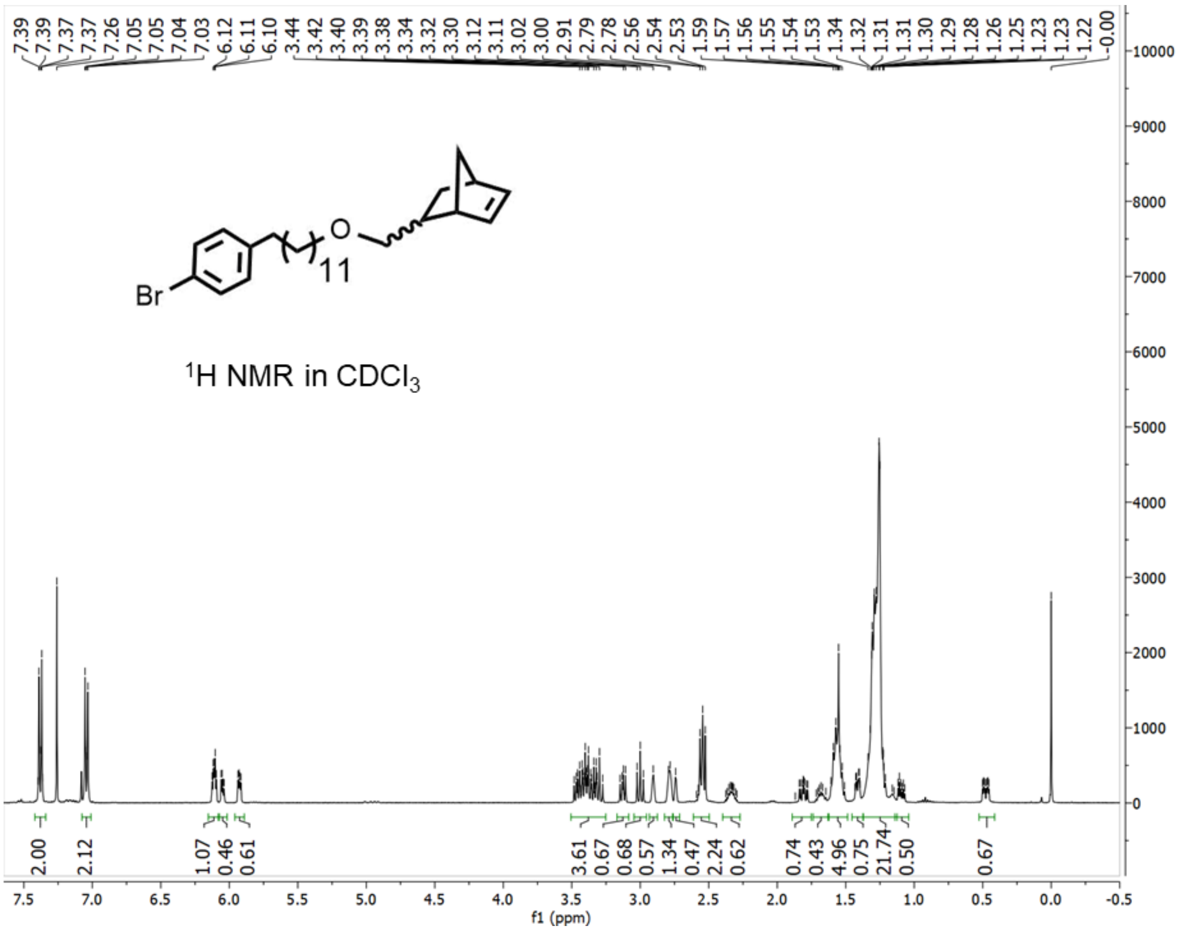
7.39
7.39
7.37
7.37
7.26
7.05
7.05
7.04
7.03
6.12
6.11
6.10
3.44
3.42
3.40
3.39
3.38
3.34
3.32
3.30
3.12
3.11
3.02
3.00
2.91
2.79
2.78
2.56
2.54
2.53
1.59
1.57
1.56
1.55
1.54
1.53
1.34
1.32
1.31
1.31
1.30
1.29
1.28
1.26
1.25
1.23
1.23
1.22
-0.00
Br
O
11
^{1}H NMR in CDCl$_3$
10000
9000
8000
7000
6000
5000
4000
3000
2000
1000
0
2.00
2.12
1.07
0.46
0.61
3.61
0.67
0.68
0.57
1.34
0.47
2.24
0.62
0.74
0.43
4.96
0.75
21.74
0.50
0.67
7.5
7.0
6.5
6.0
5.5
5.0
4.5
4.0
3.5
3.0
2.5
2.0
1.5
1.0
0.5
0.0
-0.5
f1 (ppm)

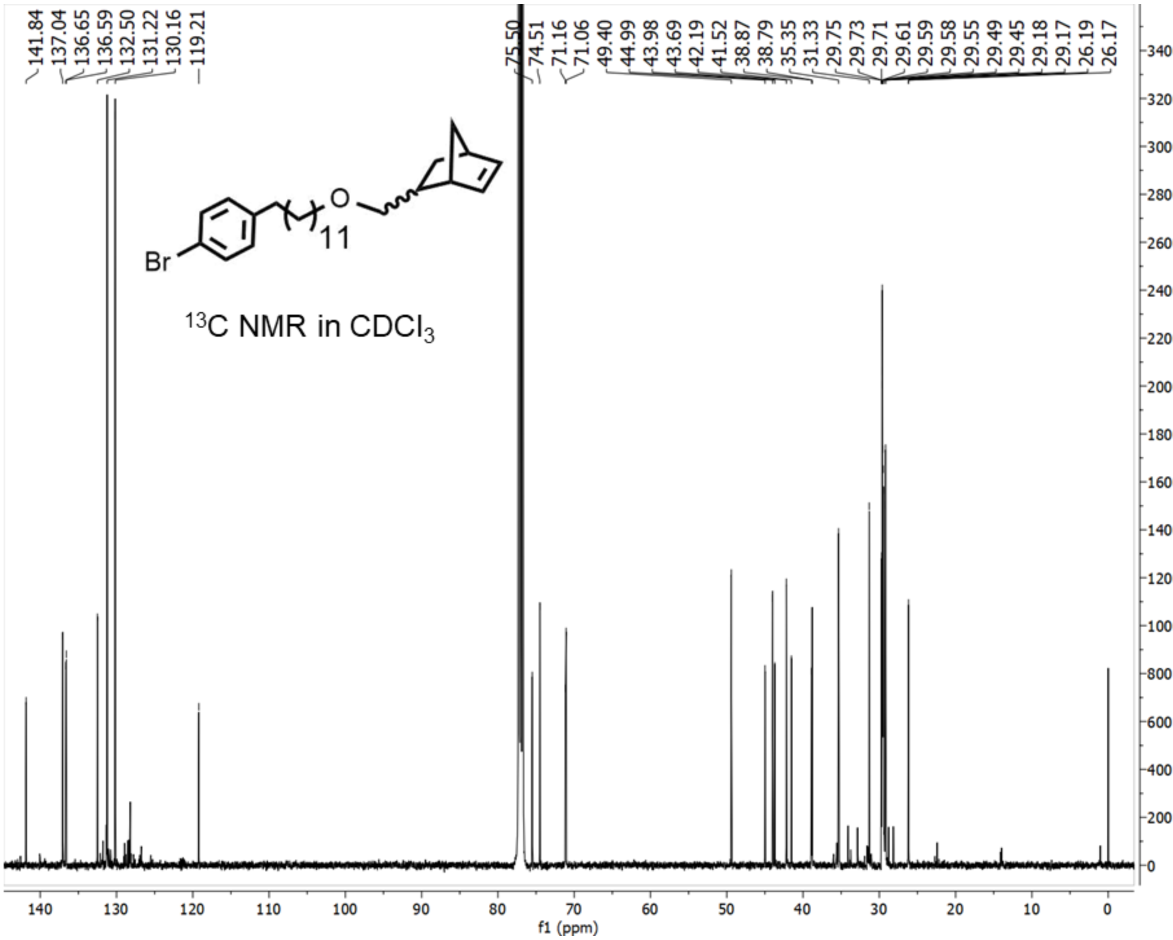
141.84
137.04
136.65
136.59
132.50
131.22
130.16
119.21
75.50
74.51
71.16
71.06
49.40
44.99
43.98
43.69
42.19
41.52
38.87
38.79
35.35
31.33
29.75
29.73
29.71
29.61
29.59
29.58
29.55
29.49
29.45
29.18
29.17
26.19
26.17
Br
O
11
^{13}C NMR in CDCl$_3$
3400
3200
3000
2800
2600
2400
2200
2000
1800
1600
1400
1200
1000
800
600
400
200
0
140
130
120
110
100
90
80
70
60
50
40
30
20
10
0
f1 (ppm)

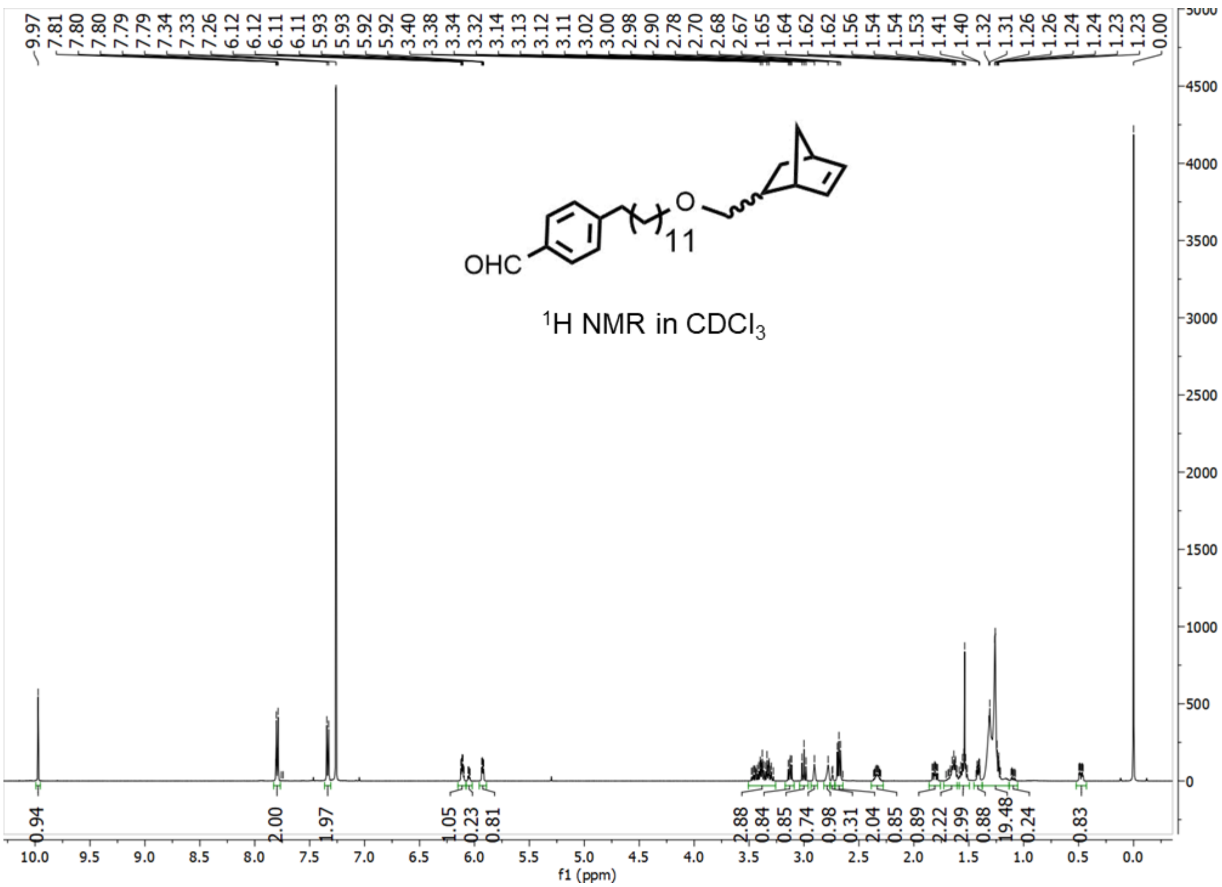
OHC
O
11
^{1}H NMR in CDCl$_3$
9.97
7.81
7.80
7.80
7.79
7.79
7.34
7.33
7.26
6.12
6.12
6.11
6.11
5.93
5.93
5.92
5.92
3.40
3.38
3.34
3.32
3.14
3.13
3.12
3.11
3.02
3.00
2.98
2.90
2.78
2.70
2.68
2.67
1.65
1.64
1.62
1.62
1.56
1.54
1.54
1.53
1.41
1.40
1.32
1.31
1.26
1.26
1.24
1.24
1.23
1.23
0.00
0.94
2.00
1.97
1.05
0.23
0.81
2.88
0.84
0.85
0.74
0.98
0.31
2.04
0.85
0.89
2.22
2.99
0.88
19.48
0.24
0.83
5000
4500
4000
3500
3000
2500
2000
1500
1000
500
0
10.0
9.5
9.0
8.5
8.0
7.5
7.0
6.5
6.0
5.5
5.0
4.5
4.0
3.5
3.0
2.5
2.0
1.5
1.0
0.5
0.0
f1 (ppm)

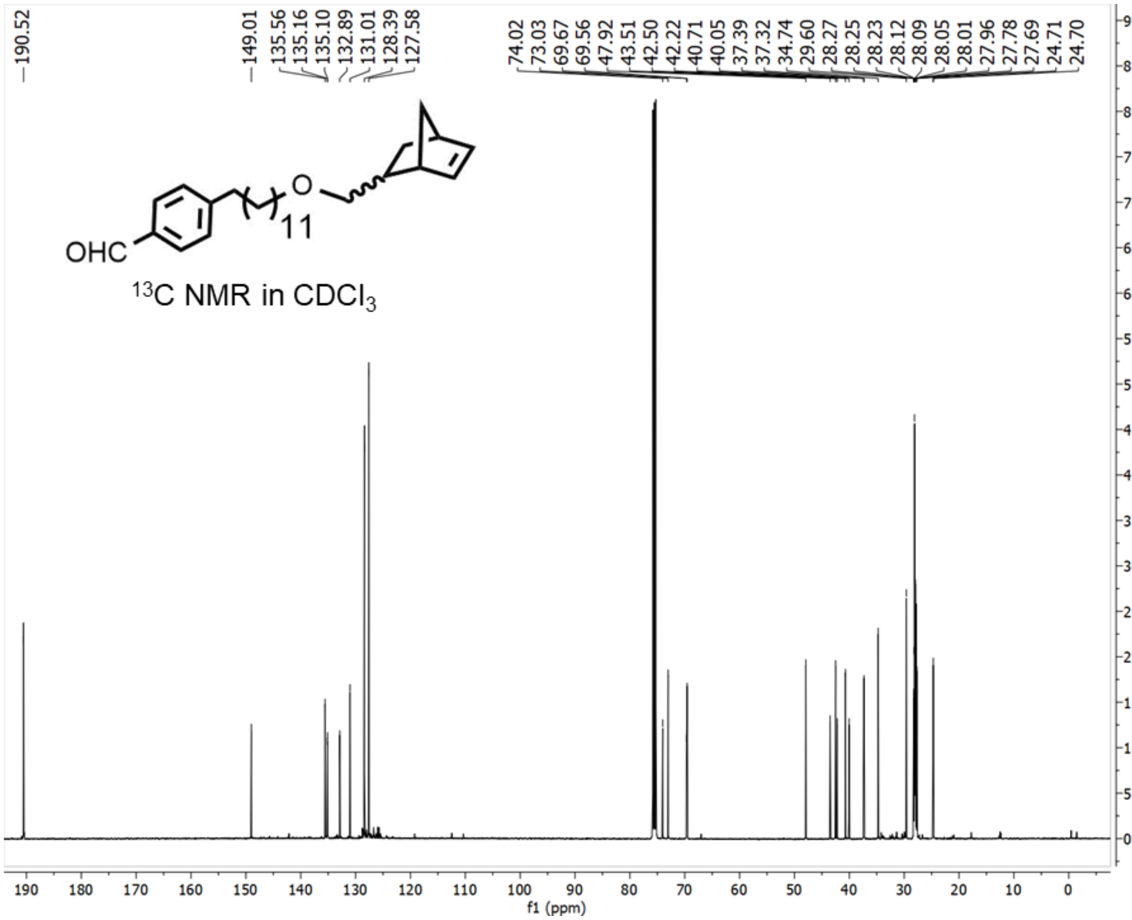
190.52
149.01
135.56
135.16
135.10
132.89
131.01
128.39
127.58
74.02
73.03
69.67
69.56
47.92
43.51
42.50
42.22
40.71
40.05
37.39
37.32
34.74
29.60
28.27
28.25
28.23
28.12
28.09
28.05
28.01
27.96
27.78
27.69
24.71
24.70
OHC
O
11
13C NMR in CDCl3
f1 (ppm)

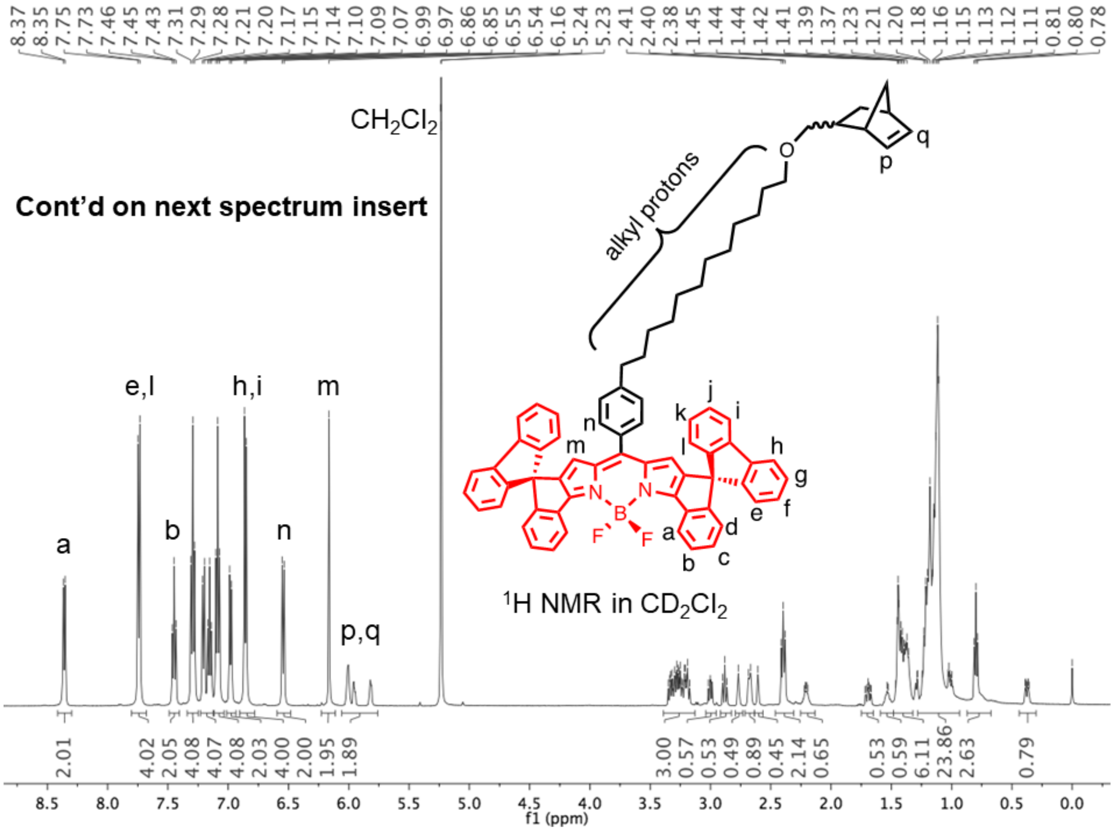

Cont’d on next spectrum insert

^1H NMR in CD_2Cl_2

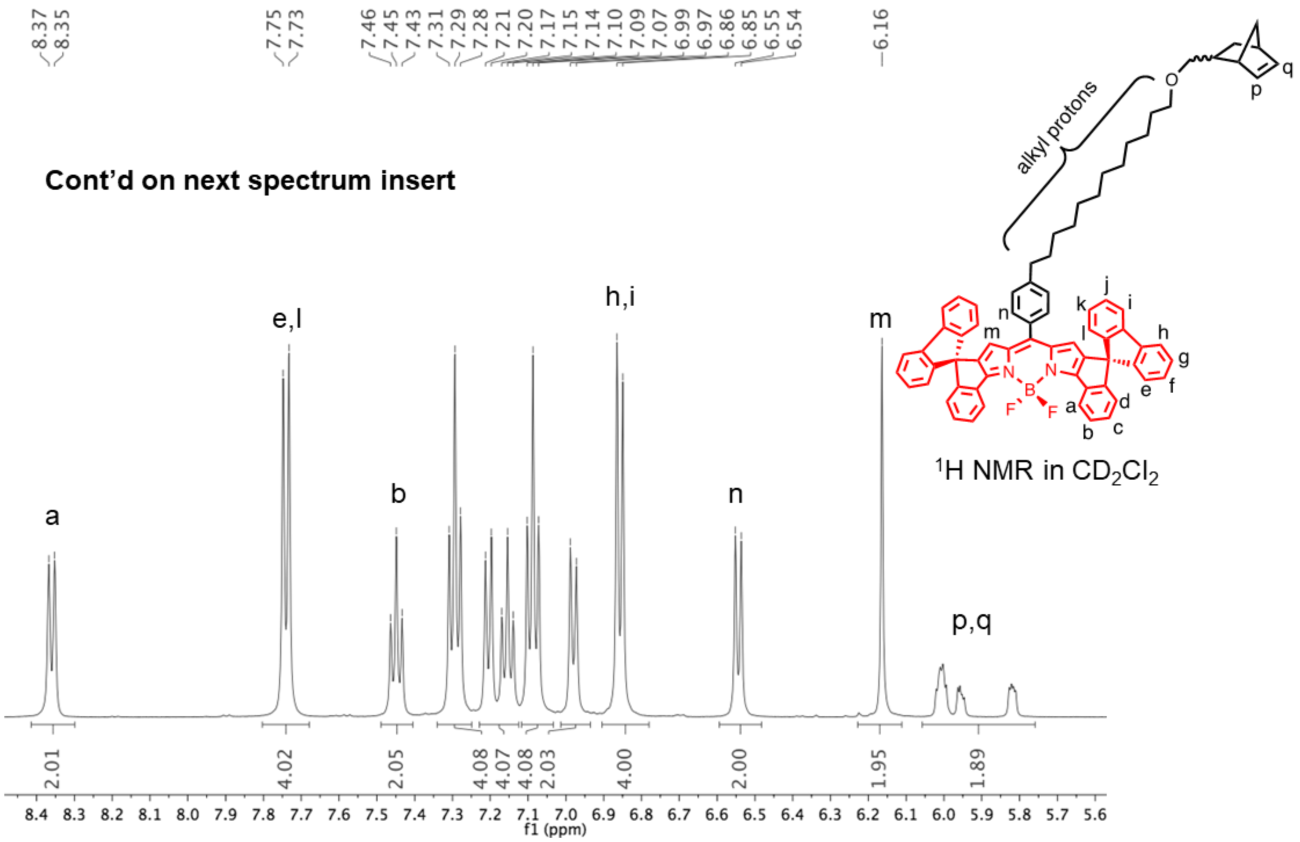
8.37
8.35
7.75
7.73
7.46
7.45
7.43
7.31
7.29
7.28
7.21
7.20
7.17
7.15
7.14
7.10
7.09
7.07
6.99
6.97
6.86
6.85
6.55
6.54
6.16
Cont'd on next spectrum insert
alkyl protons
O
q
p
n
m
k
j
i
l
h
g
e
f
N
B
N
F
F
a
d
b
c
^{1}H NMR in CD_2Cl_2
a
e,l
b
h,i
n
m
p,q
2.01
4.02
2.05
4.08
4.07
4.08
2.03
4.00
2.00
1.95
1.89
8.4
8.3
8.2
8.1
8.0
7.9
7.8
7.7
7.6
7.5
7.4
7.3
7.2
7.1
7.0
6.9
6.8
6.7
6.6
6.5
6.4
6.3
6.2
6.1
6.0
5.9
5.8
5.7
5.6
f1 (ppm)

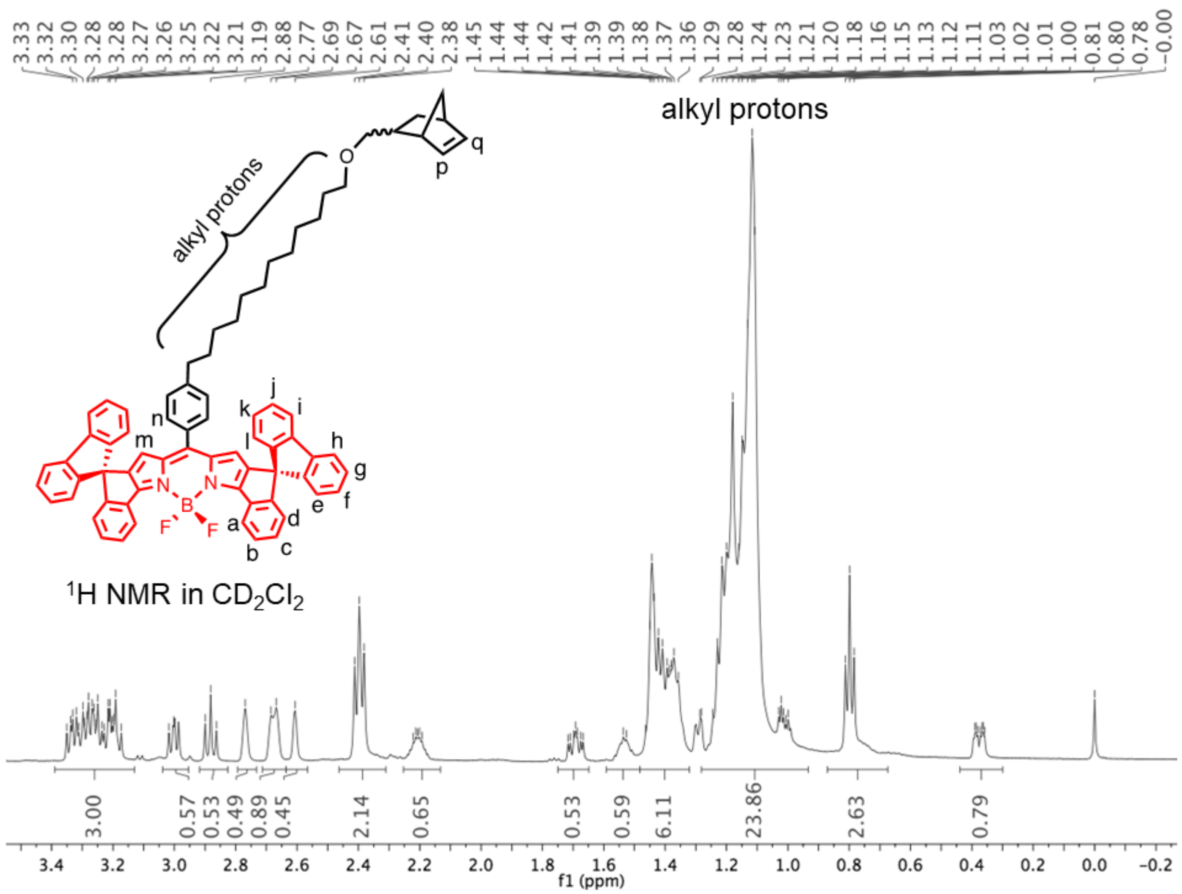
3.33
3.32
3.30
3.28
3.28
3.27
3.26
3.25
3.22
3.21
3.19
2.88
2.77
2.69
2.67
2.61
2.41
2.40
2.38
1.45
1.44
1.42
1.41
1.39
1.39
1.38
1.37
1.36
1.29
1.28
1.24
1.23
1.21
1.20
1.18
1.16
1.15
1.13
1.12
1.11
1.03
1.02
1.01
1.00
0.81
0.80
0.78
-0.00
alkyl protons
alkyl protons
O
p
q
n
m
k
j
i
l
h
g
N
B
N
F
F
a
d
e
f
b
c
^{1}H NMR in CD_2Cl_2
3.00
0.57
0.53
0.49
0.89
0.45
2.14
0.65
0.53
0.59
6.11
23.86
2.63
0.79
3.4
3.2
3.0
2.8
2.6
2.4
2.2
2.0
1.8
1.6
1.4
1.2
1.0
0.8
0.6
0.4
0.2
0.0
-0.2
f1 (ppm)

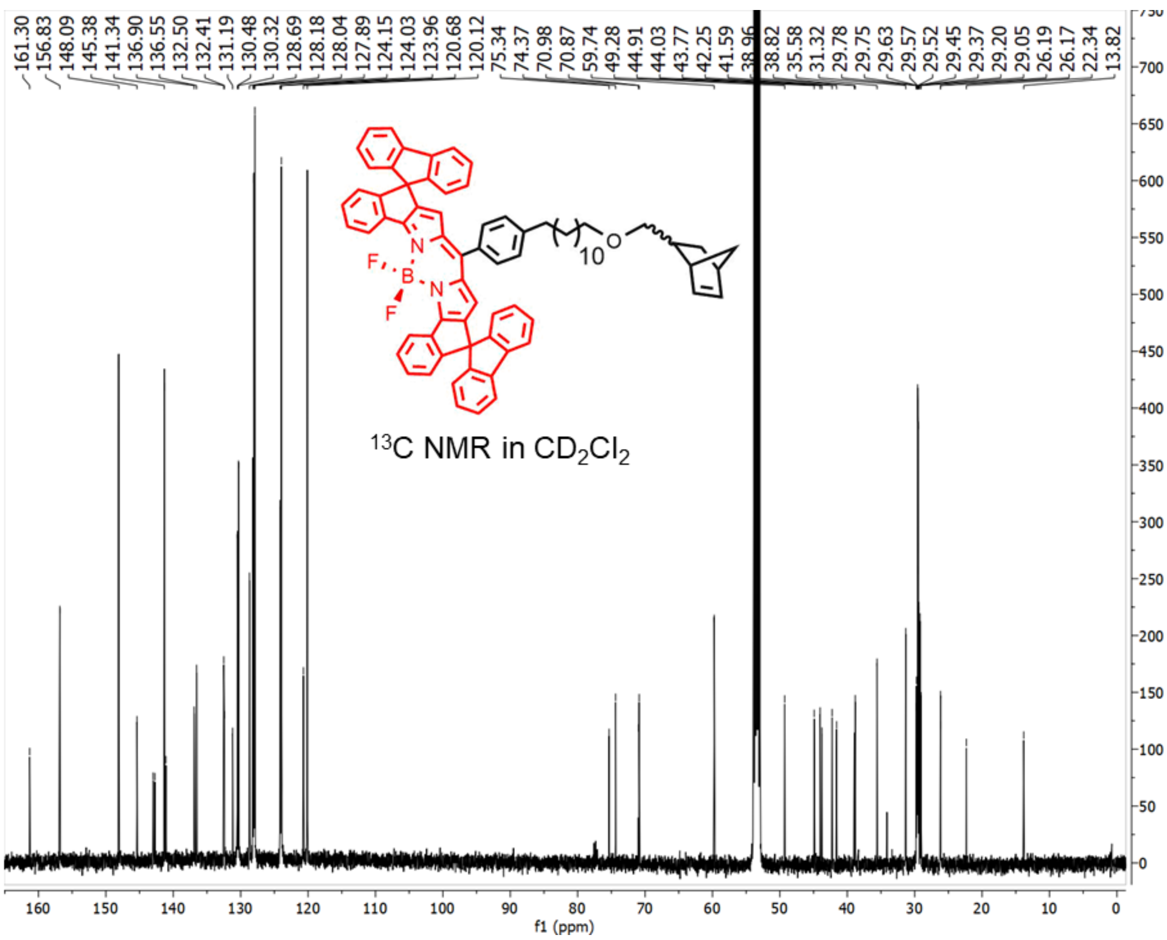
161.30
156.83
148.09
145.38
141.34
136.90
136.55
132.50
132.41
131.19
130.48
130.32
128.69
128.18
128.04
127.89
124.15
124.03
123.96
120.68
120.12
75.34
74.37
70.98
70.87
59.74
49.28
44.91
44.03
43.77
42.25
41.59
38.96
38.82
35.58
31.32
29.78
29.75
29.63
29.57
29.52
29.45
29.37
29.20
29.05
26.19
26.17
22.34
13.82
F
B
F
N
N
10
O
^{13}C NMR in CD_2Cl_2
750
700
650
600
550
500
450
400
350
300
250
200
150
100
50
0
160
150
140
130
120
110
100
90
80
70
60
50
40
30
20
10
0
f1 (ppm)

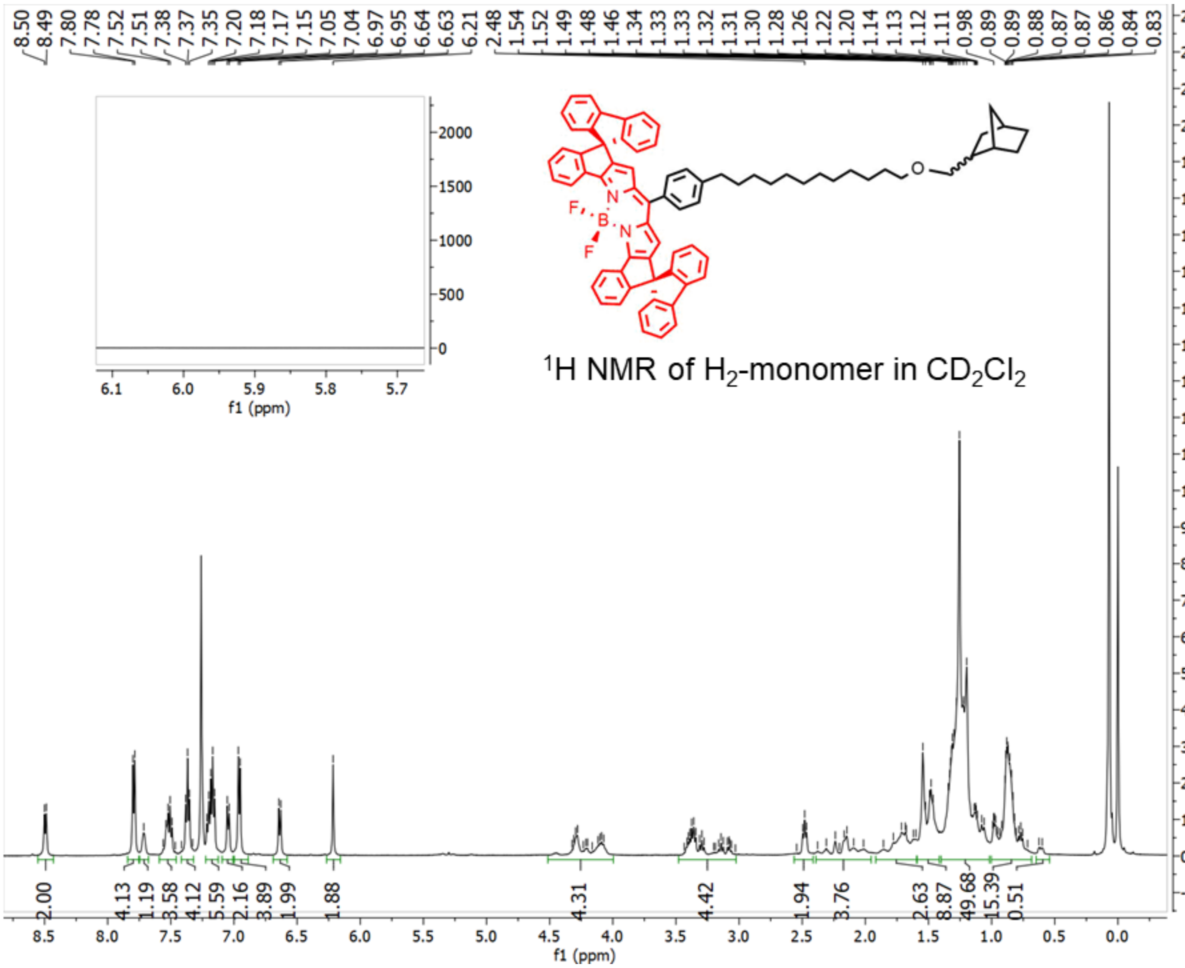

^{1}H NMR of H_2-monomer in CD_2Cl_2

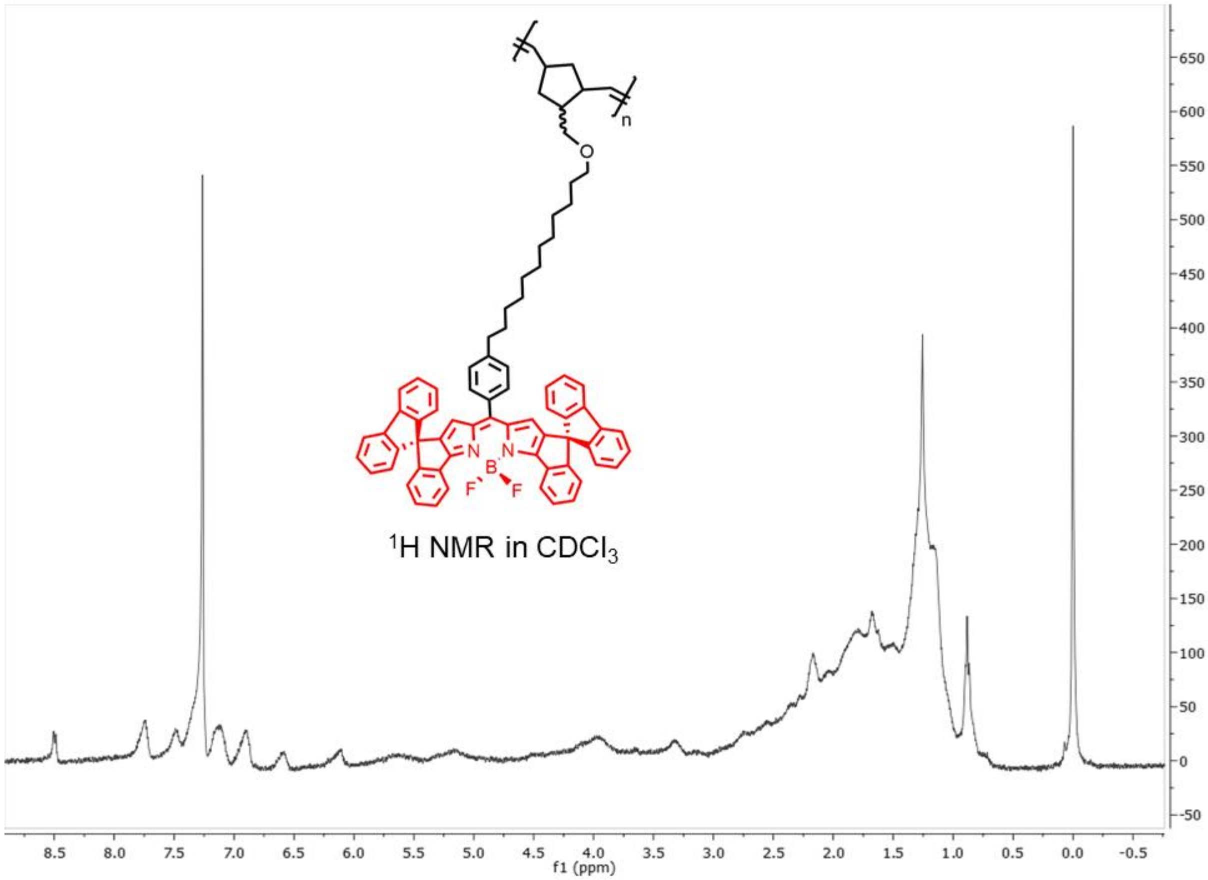
n
O
N
B
N
F
F
^{1}H NMR in CDCl$_3$
650
600
550
500
450
400
350
300
250
200
150
100
50
0
-50
8.5
8.0
7.5
7.0
6.5
6.0
5.5
5.0
4.5
4.0
3.5
3.0
2.5
2.0
1.5
1.0
0.5
0.0
-0.5
f1 (ppm)

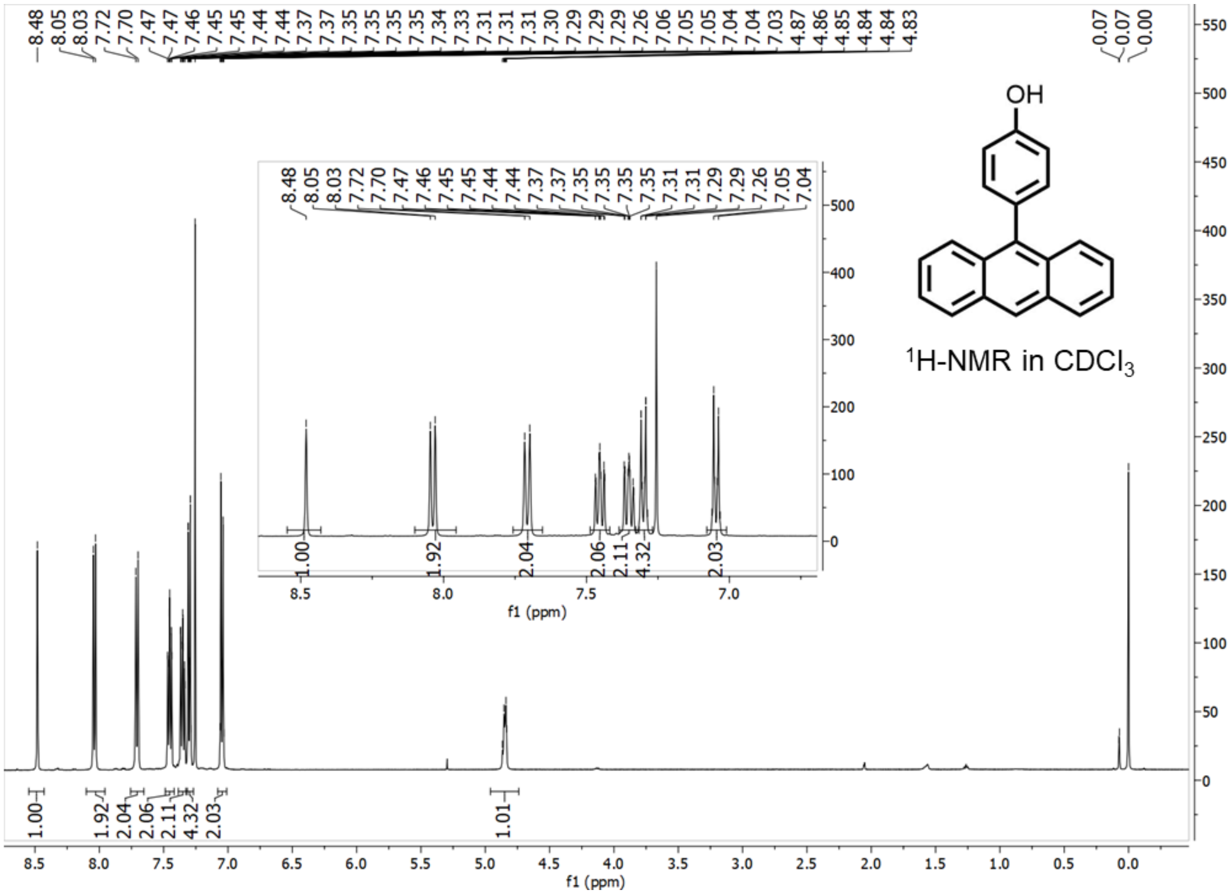
8.48
8.05
8.03
7.72
7.70
7.47
7.47
7.46
7.45
7.45
7.44
7.44
7.37
7.37
7.35
7.35
7.35
7.35
7.34
7.33
7.31
7.31
7.30
7.29
7.29
7.29
7.26
7.06
7.05
7.05
7.04
7.04
7.03
4.87
4.86
4.85
4.84
4.84
4.83
0.07
0.07
0.00
OH
^{1}H-NMR in CDCl$_3$
1.00
1.92
2.04
2.06
2.11
4.32
2.03
1.01
f1 (ppm)

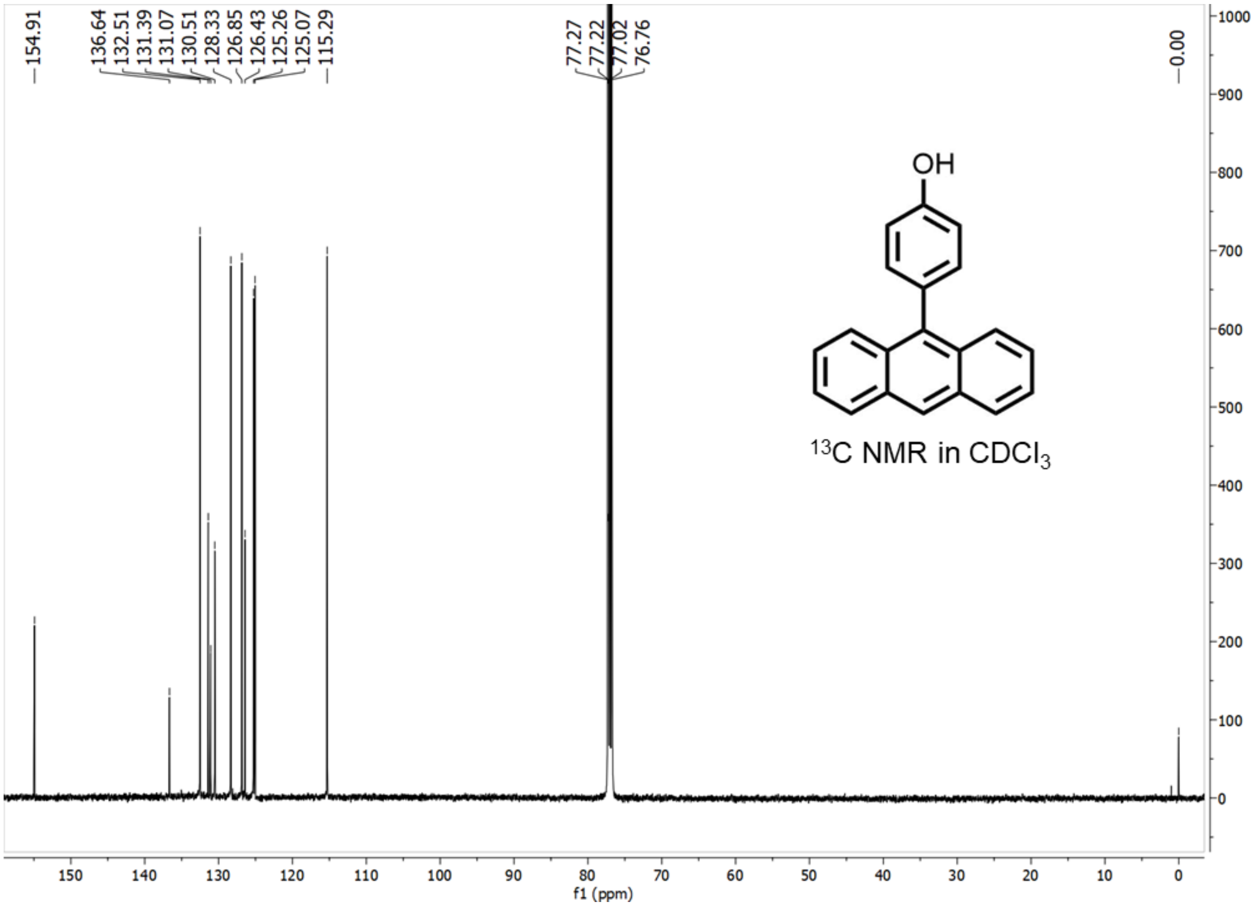
154.91
136.64
132.51
131.39
131.07
130.51
128.33
126.85
126.43
125.26
125.07
115.29
77.27
77.22
77.02
76.76
0.00
OH
^{13}C NMR in CDCl$_3$
1000
900
800
700
600
500
400
300
200
100
0
150
140
130
120
110
100
90
80
70
60
50
40
30
20
10
0
f1 (ppm)

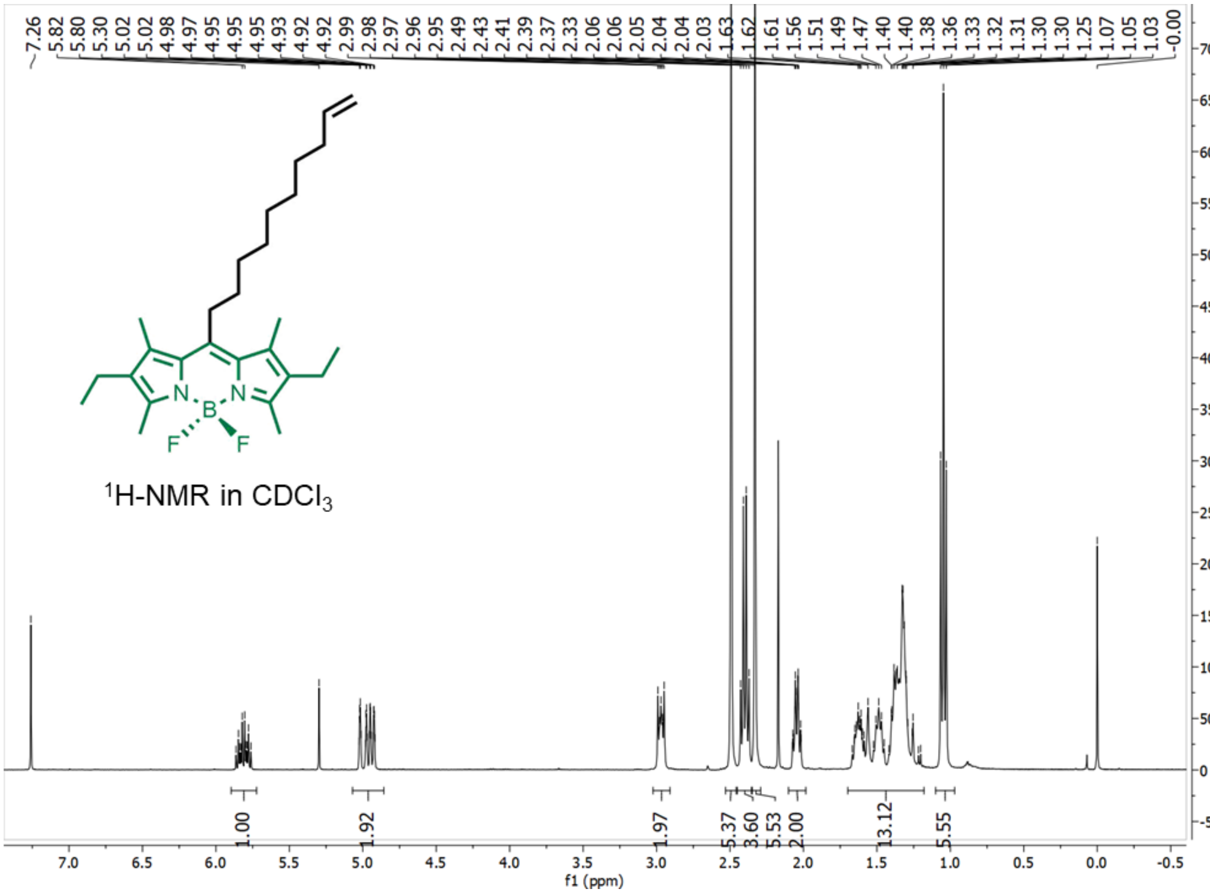
7.26
5.82
5.80
5.30
5.02
5.02
4.98
4.97
4.95
4.95
4.95
4.93
4.92
4.92
2.99
2.98
2.97
2.96
2.95
2.49
2.43
2.41
2.39
2.37
2.33
2.06
2.06
2.05
2.04
2.04
2.03
1.63
1.62
1.61
1.56
1.51
1.49
1.47
1.40
1.40
1.38
1.36
1.33
1.32
1.31
1.30
1.30
1.25
1.07
1.05
1.03
-0.00
N
B
N
F
F
^{1}H-NMR in $CDCl_3$
1.00
1.92
1.97
5.37
3.60
5.53
2.00
13.12
5.55
7.0
6.5
6.0
5.5
5.0
4.5
4.0
3.5
3.0
2.5
2.0
1.5
1.0
0.5
0.0
-0.5
f1 (ppm)
7000
6500
6000
5500
5000
4500
4000
3500
3000
2500
2000
1500
1000
500
0
-500

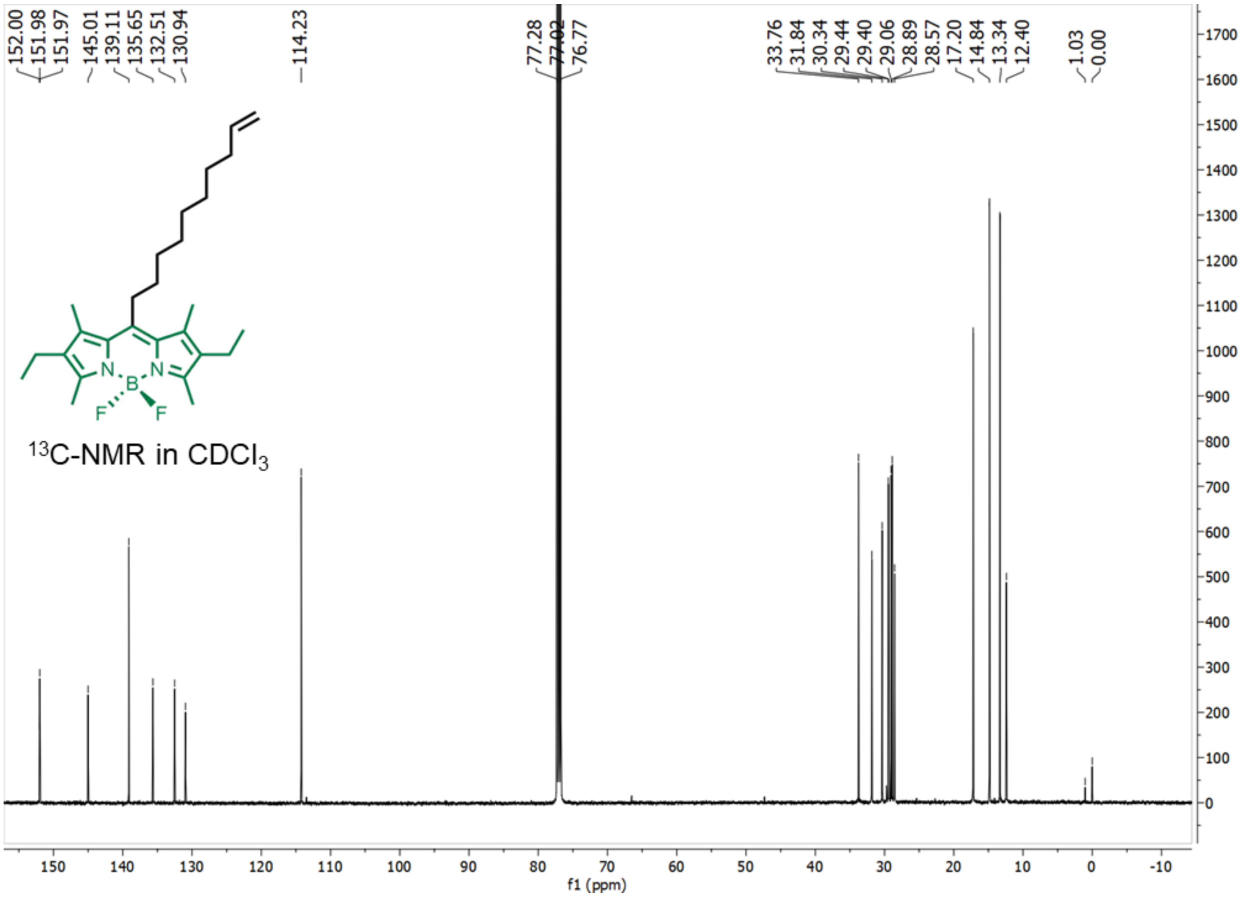
152.00
151.98
151.97
145.01
139.11
135.65
132.51
130.94
114.23
77.28
77.02
76.77
33.76
31.84
30.34
29.44
29.40
29.06
28.89
28.57
17.20
14.84
13.34
12.40
1.03
0.00
N
B
N
F
F
^{13}C-NMR in CDCl$_3$
1700
1600
1500
1400
1300
1200
1100
1000
900
800
700
600
500
400
300
200
100
0
150
140
130
120
110
100
90
80
70
60
50
40
30
20
10
0
-10
f1 (ppm)

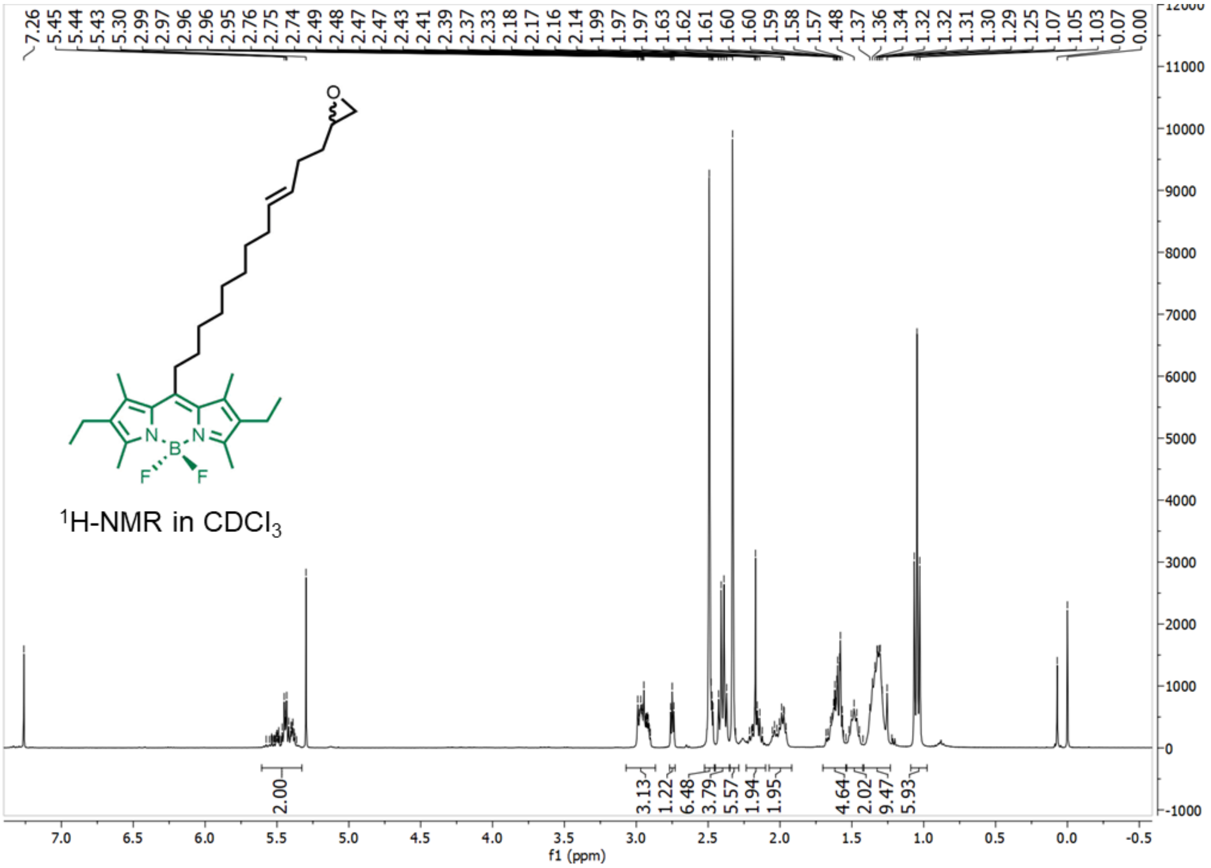

^{1}H-NMR in CDCl$_3$
O
N
B
N
F
F
7.26
5.45
5.44
5.43
5.30
2.99
2.97
2.96
2.96
2.95
2.76
2.75
2.74
2.49
2.48
2.47
2.47
2.43
2.41
2.39
2.37
2.33
2.18
2.17
2.16
2.14
1.99
1.97
1.97
1.63
1.62
1.61
1.60
1.60
1.59
1.58
1.57
1.48
1.37
1.36
1.34
1.32
1.32
1.31
1.30
1.29
1.25
1.07
1.05
1.03
0.07
0.00
2.00
3.13
1.22
6.48
3.79
5.57
1.94
1.95
4.64
2.02
9.47
5.93
7.0
6.5
6.0
5.5
5.0
4.5
4.0
3.5
3.0
2.5
2.0
1.5
1.0
0.5
0.0
-0.5
f1 (ppm)
12000
11000
10000
9000
8000
7000
6000
5000
4000
3000
2000
1000
0
-1000

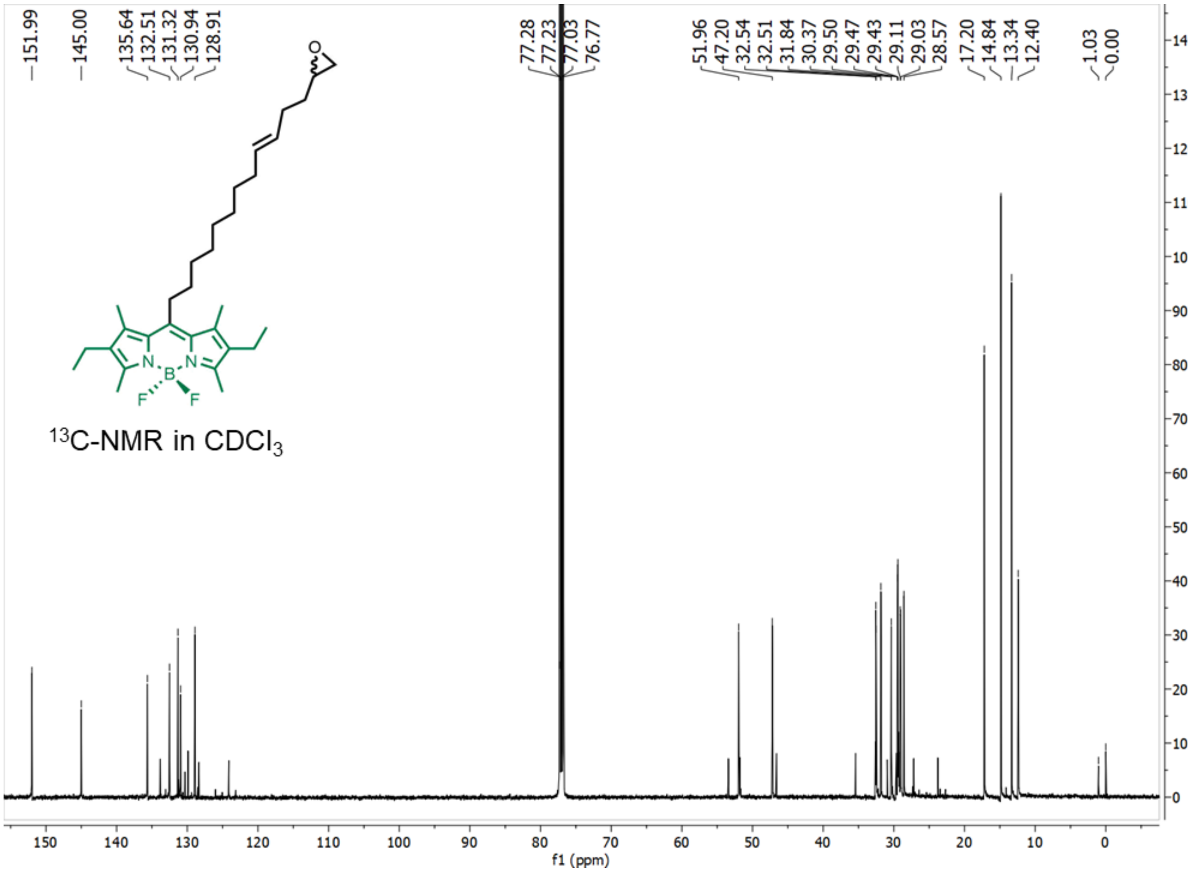
151.99
145.00
135.64
132.51
131.32
130.94
128.91
77.28
77.23
77.03
76.77
51.96
47.20
32.54
32.51
31.84
30.37
29.50
29.47
29.43
29.11
29.03
28.57
17.20
14.84
13.34
12.40
1.03
0.00
O
N
B
N
F
F
^{13}C-NMR in $CDCl_3$
1400
1300
1200
1100
1000
900
800
700
600
500
400
300
200
100
0
150
140
130
120
110
100
90
80
70
60
50
40
30
20
10
0
f1 (ppm)

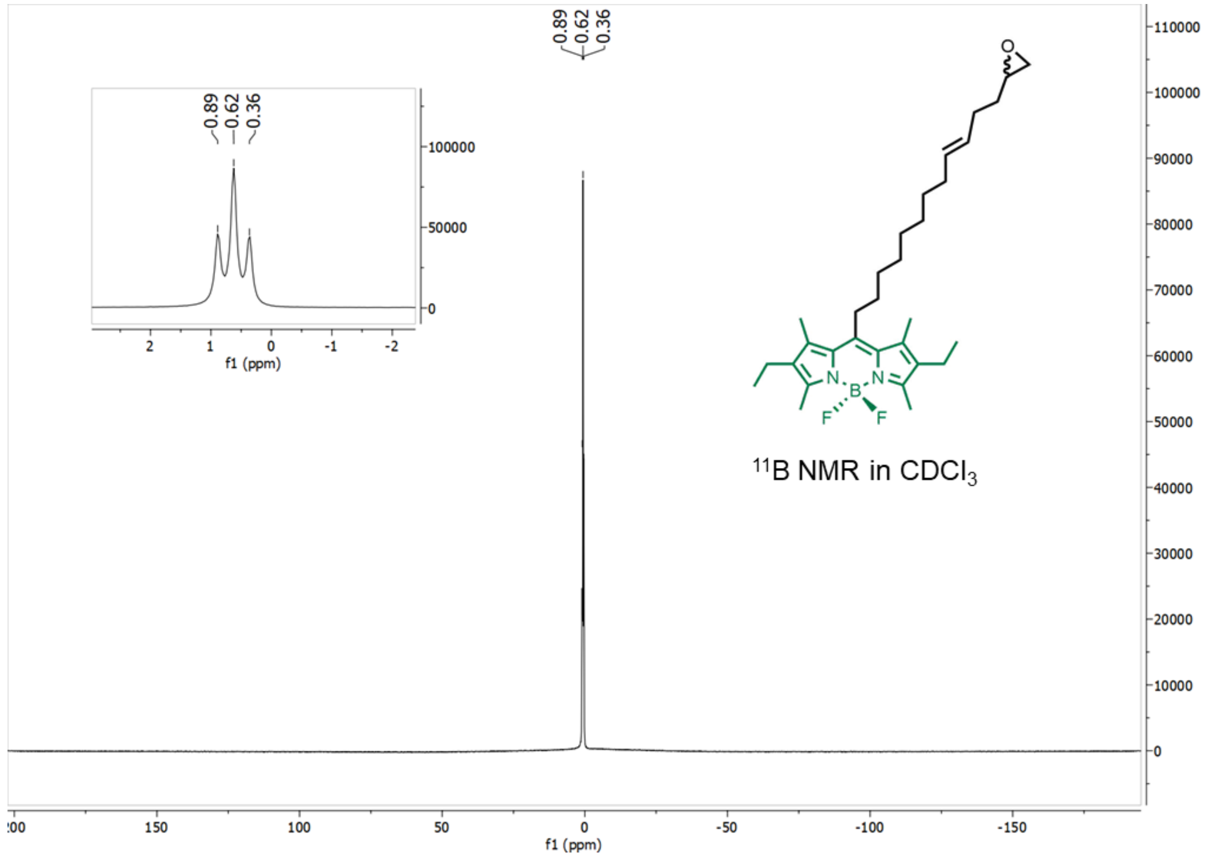

^{11}B NMR in $CDCl_3$

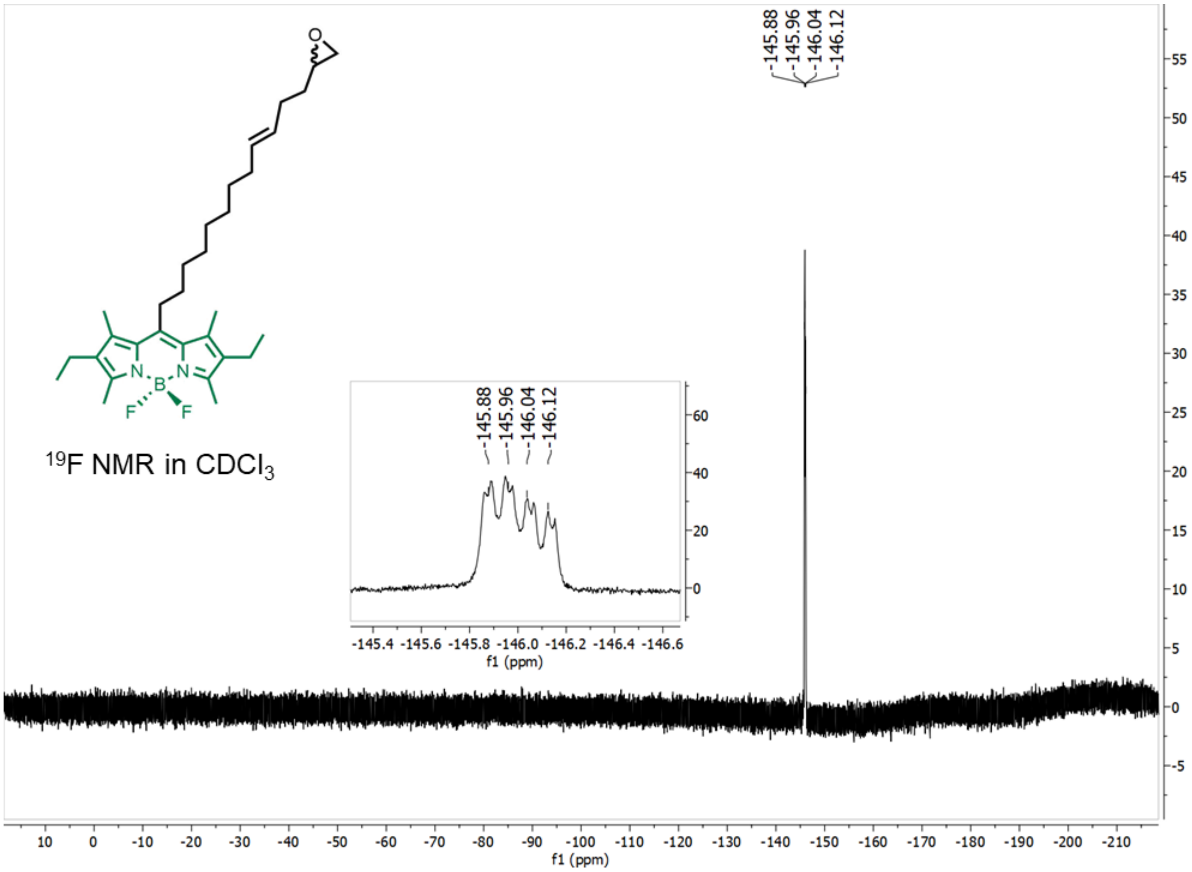
O
N
B
N
F
F
^{19}F NMR in CDCl$_3$
-145.88
-145.96
-146.04
-146.12
60
40
20
0
-145.4 -145.6 -145.8 -146.0 -146.2 -146.4 -146.6
f1 (ppm)
55
50
45
40
35
30
25
20
15
10
5
0
-5
10 0 -10 -20 -30 -40 -50 -60 -70 -80 -90 -100 -110 -120 -130 -140 -150 -160 -170 -180 -190 -200 -210
f1 (ppm)

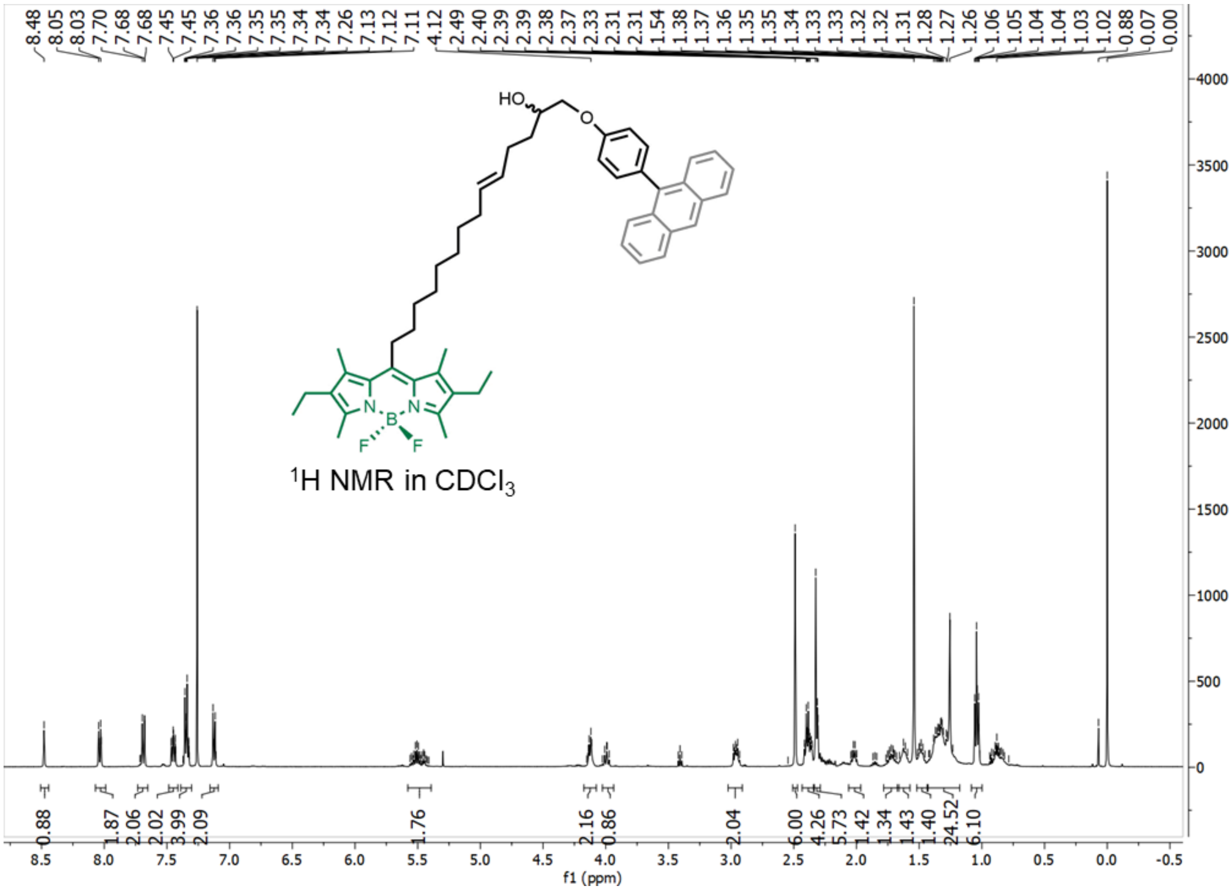
8.48
8.05
8.03
7.70
7.68
7.68
7.45
7.45
7.36
7.36
7.35
7.35
7.34
7.34
7.26
7.13
7.12
7.11
4.12
2.49
2.40
2.39
2.39
2.38
2.37
2.33
2.31
2.31
1.54
1.38
1.37
1.36
1.35
1.35
1.34
1.33
1.33
1.32
1.32
1.31
1.28
1.27
1.26
1.06
1.05
1.04
1.04
1.03
1.02
0.88
0.07
0.00
HO
O
N
B
N
F
F
^{1}H NMR in CDCl$_3$
4000
3500
3000
2500
2000
1500
1000
500
0
0.88
1.87
2.06
2.02
3.99
2.09
1.76
2.16
0.86
2.04
6.00
4.26
5.73
1.42
1.34
1.43
1.40
24.52
6.10
8.5
8.0
7.5
7.0
6.5
6.0
5.5
5.0
4.5
4.0
3.5
3.0
2.5
2.0
1.5
1.0
0.5
0.0
-0.5
f1 (ppm)

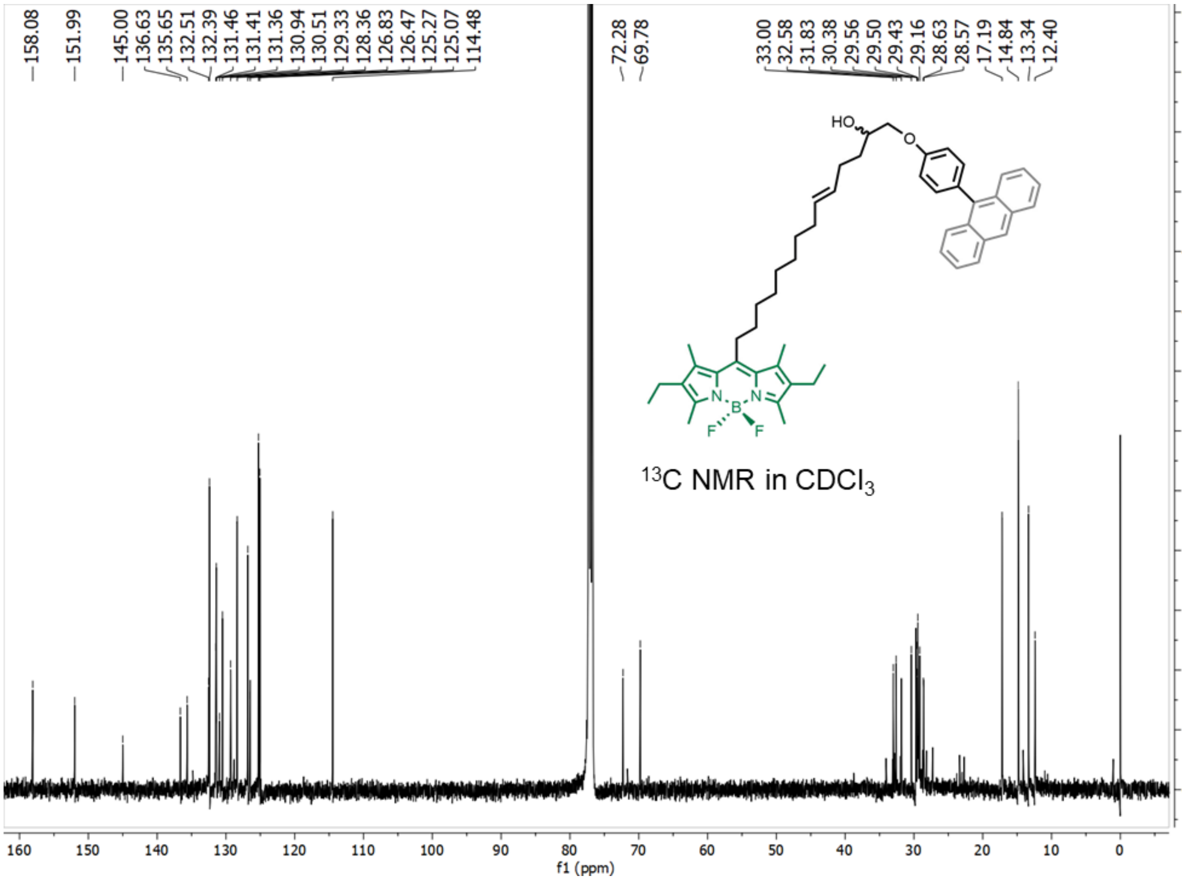
158.08
151.99
145.00
136.63
135.65
132.51
132.39
131.46
131.41
131.36
130.94
130.51
129.33
128.36
126.83
126.47
125.27
125.07
114.48
72.28
69.78
33.00
32.58
31.83
30.38
29.56
29.50
29.43
29.16
28.63
28.57
17.19
14.84
13.34
12.40
HO
O
N
B
N
F
F
^{13}C NMR in CDCl$_3$
650
600
550
500
450
400
350
300
250
200
150
100
50
0
160
150
140
130
120
110
100
90
80
70
60
50
40
30
20
10
0
f1 (ppm)

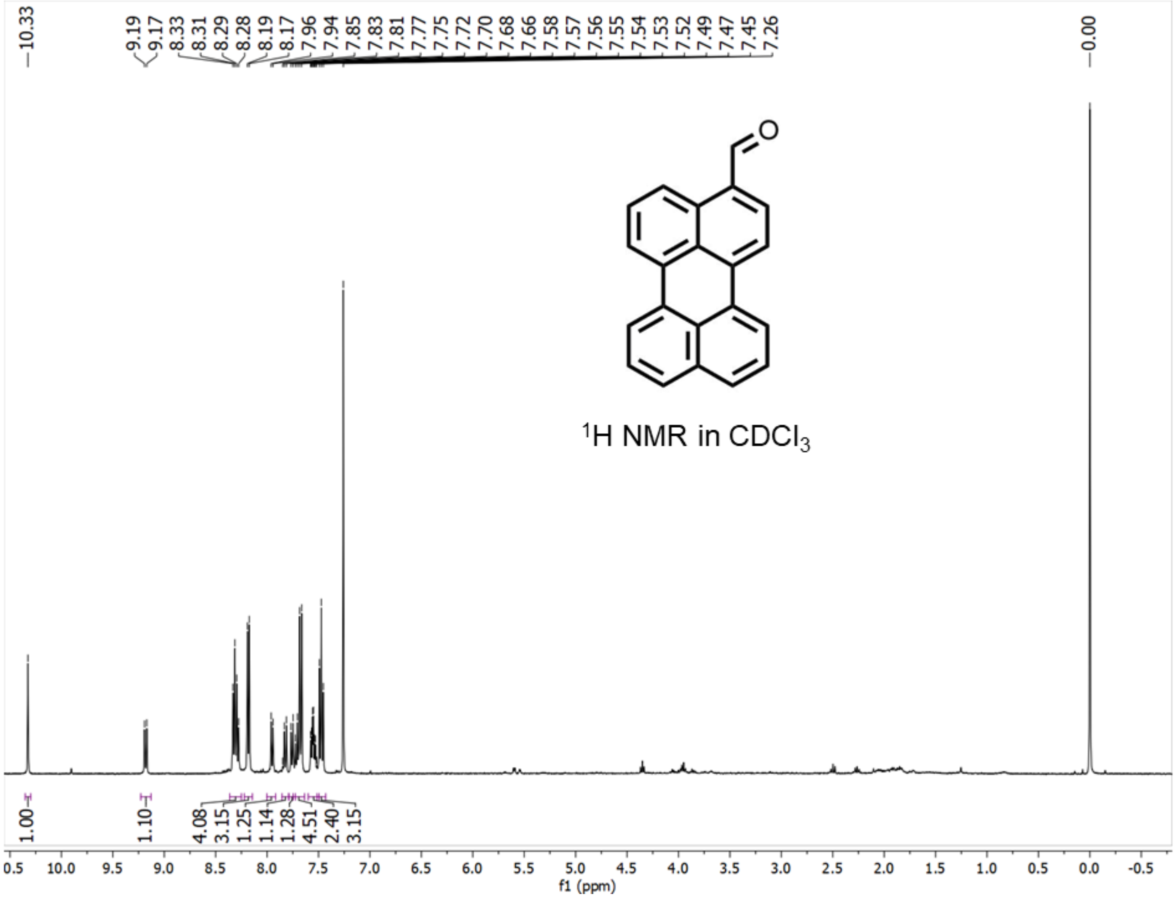

10.33
9.19
9.17
8.33
8.31
8.29
8.28
8.19
8.17
7.96
7.94
7.85
7.83
7.81
7.77
7.75
7.72
7.70
7.68
7.66
7.58
7.57
7.56
7.55
7.54
7.53
7.52
7.49
7.47
7.45
7.26
0.00
O
^{1}H NMR in $CDCl_3$
1.00
1.10
4.08
3.15
1.25
1.14
1.28
4.51
2.40
3.15
0.5
10.0
9.5
9.0
8.5
8.0
7.5
7.0
6.5
6.0
5.5
5.0
4.5
4.0
3.5
3.0
2.5
2.0
1.5
1.0
0.5
0.0
-0.5
f1 (ppm)

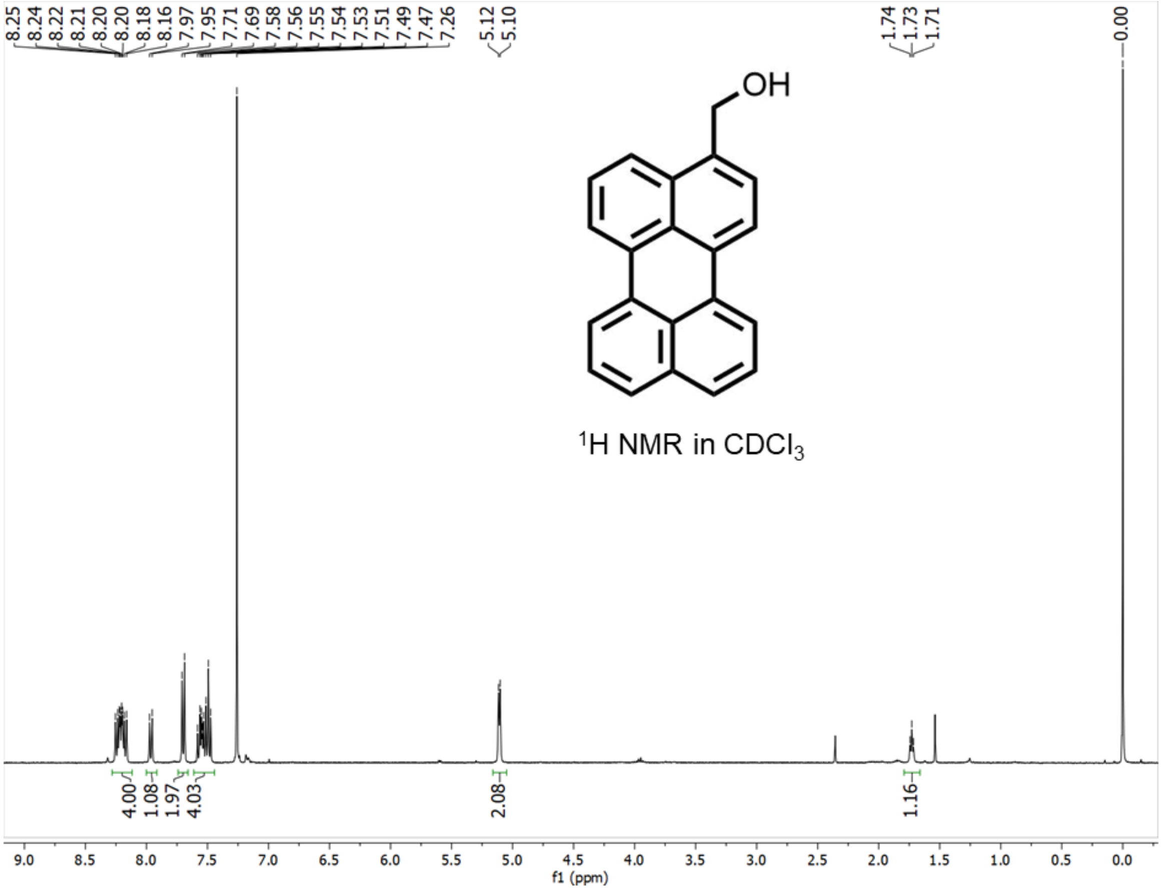
8.25
8.24
8.22
8.21
8.20
8.20
8.18
8.16
7.97
7.95
7.71
7.69
7.58
7.56
7.55
7.54
7.53
7.51
7.49
7.47
7.26
5.12
5.10
1.74
1.73
1.71
0.00
OH
^{1}H NMR in CDCl$_3$
4.00
1.08
1.97
4.03
2.08
1.16
9.0
8.5
8.0
7.5
7.0
6.5
6.0
5.5
5.0
4.5
4.0
3.5
3.0
2.5
2.0
1.5
1.0
0.5
0.0
f1 (ppm)

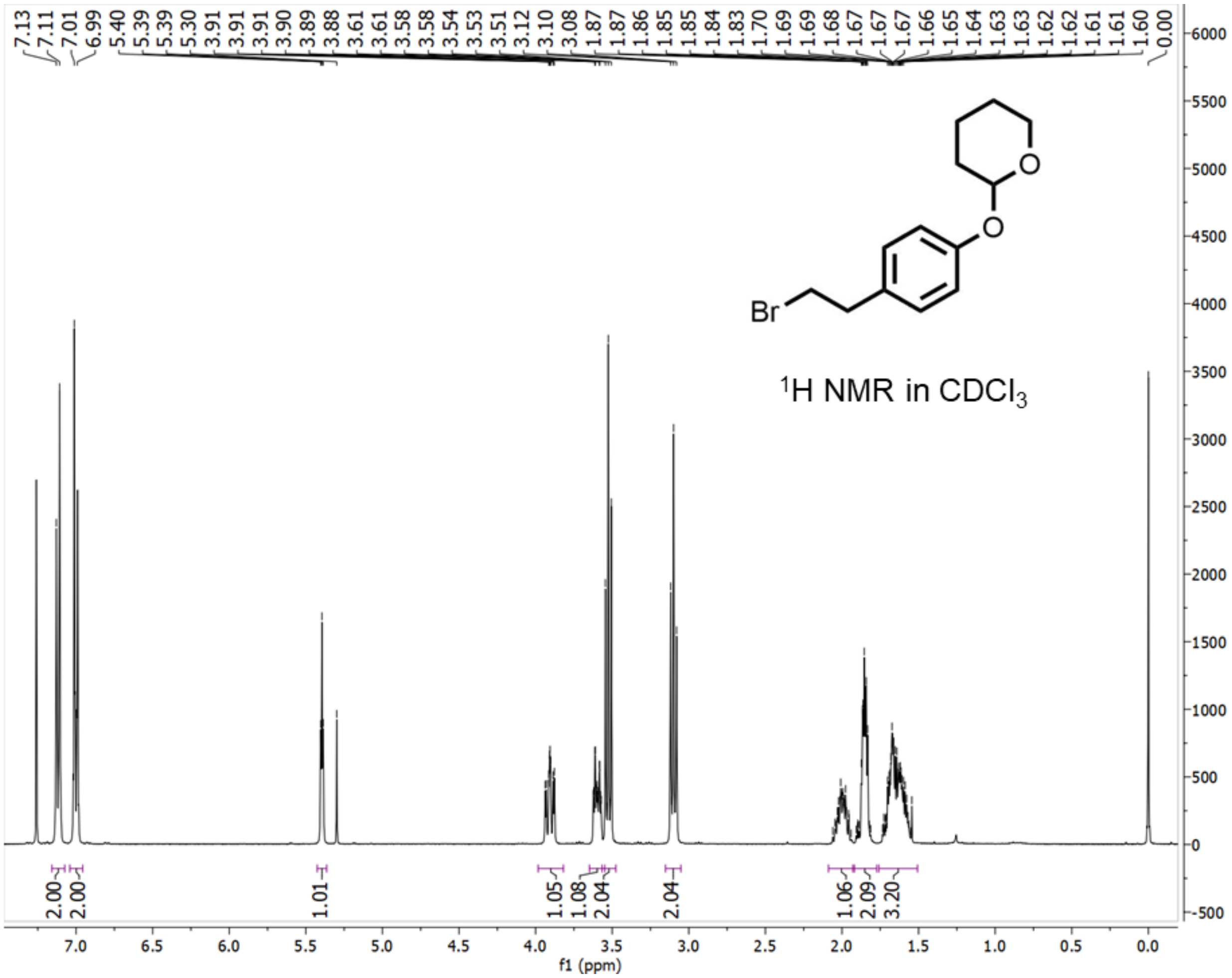
7.13
7.11
7.01
6.99
5.40
5.39
5.39
5.30
3.91
3.91
3.90
3.89
3.88
3.61
3.61
3.58
3.58
3.54
3.53
3.51
3.12
3.10
3.08
1.87
1.87
1.86
1.85
1.85
1.84
1.83
1.70
1.69
1.69
1.68
1.67
1.67
1.67
1.66
1.65
1.64
1.63
1.63
1.62
1.62
1.61
1.61
1.60
0.00
Br
O
O
^{1}H NMR in CDCl$_3$
2.00
2.00
1.01
1.05
1.08
2.04
2.04
1.06
2.09
3.20
f1 (ppm)

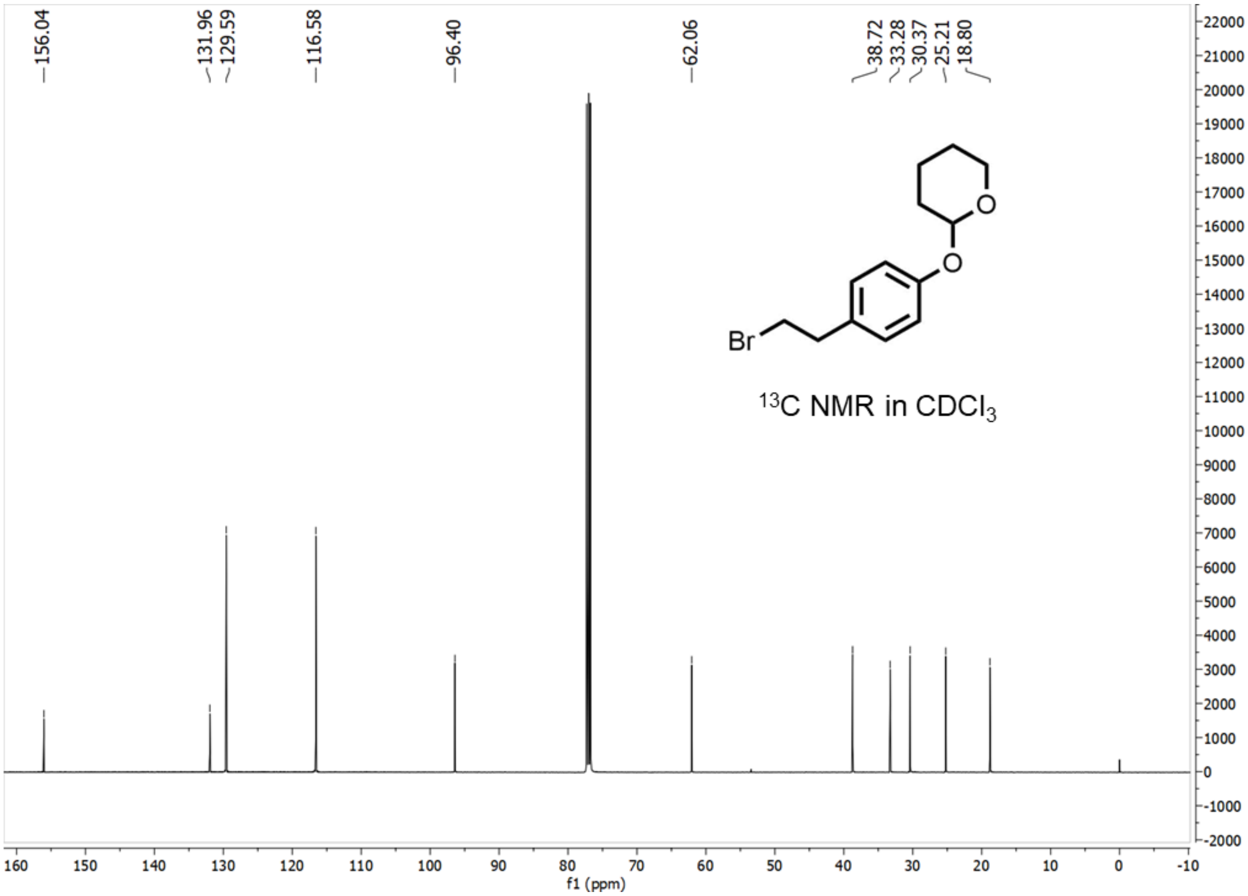
156.04
131.96
129.59
116.58
96.40
62.06
38.72
33.28
30.37
25.21
18.80
Br
O
O
^{13}C NMR in CDCl$_3$
f1 (ppm)
160
150
140
130
120
110
100
90
80
70
60
50
40
30
20
10
0
-10
22000
21000
20000
19000
18000
17000
16000
15000
14000
13000
12000
11000
10000
9000
8000
7000
6000
5000
4000
3000
2000
1000
0
-1000
-2000

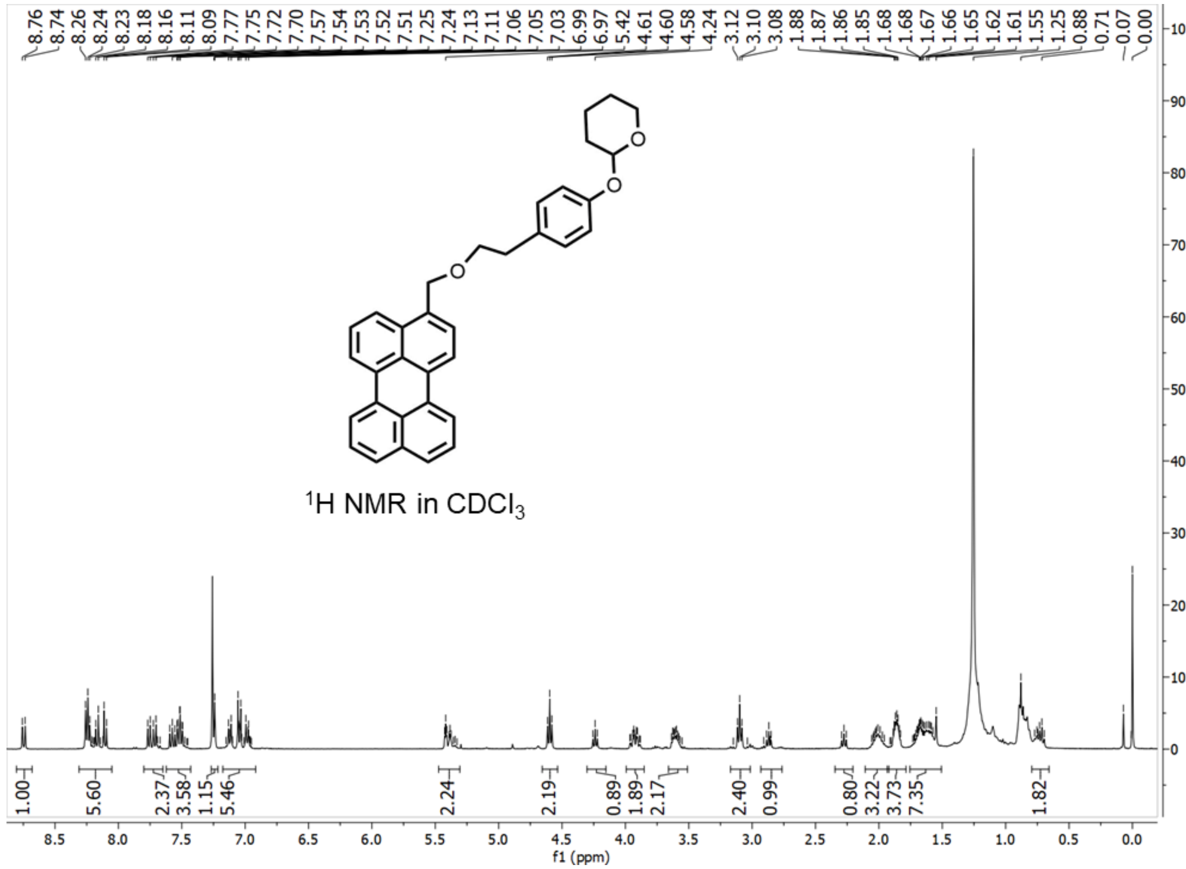

^{1}H NMR in $CDCl_3$

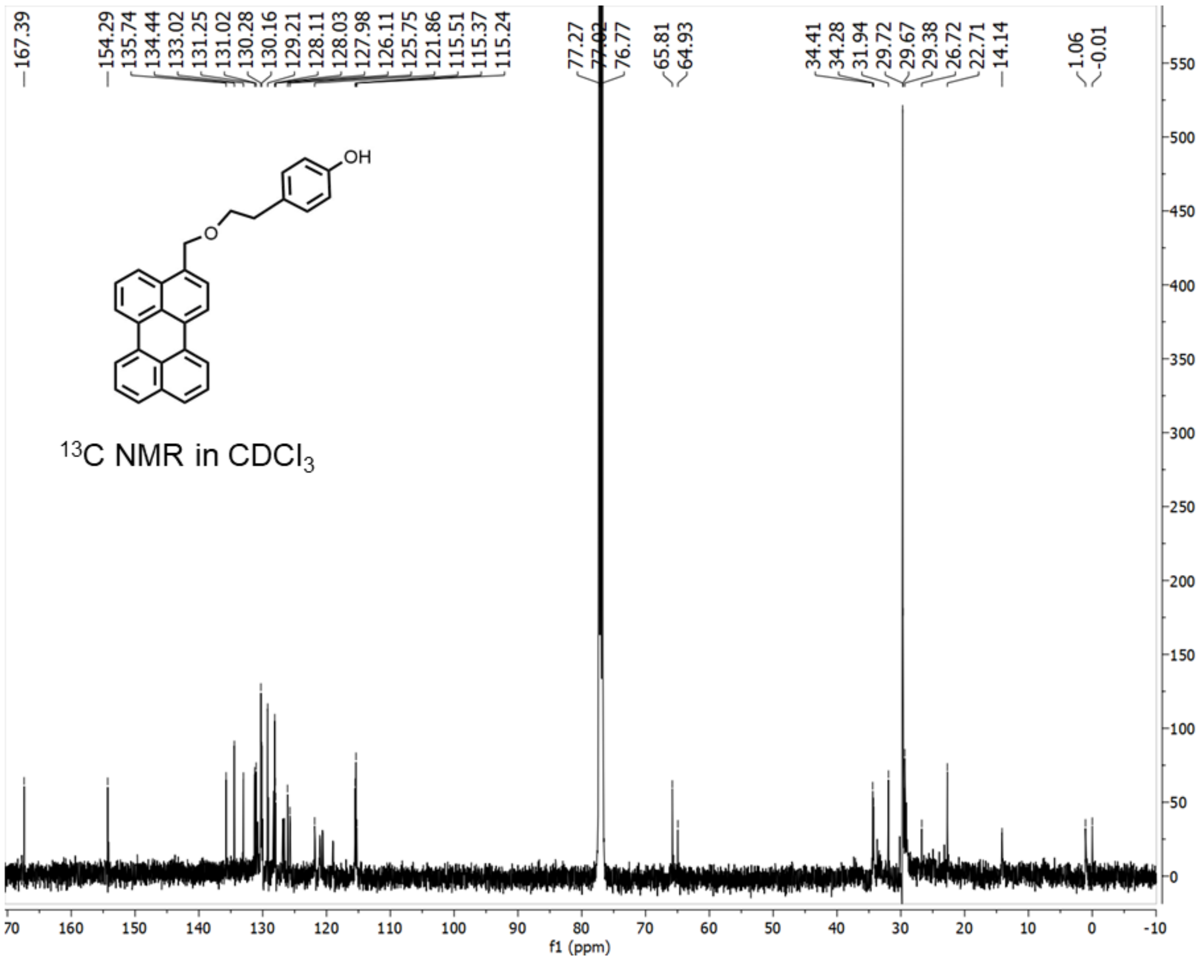
167.39
154.29
135.74
134.44
133.02
131.25
131.02
130.28
130.16
129.21
128.11
128.03
127.98
126.11
125.75
121.86
115.51
115.37
115.24
77.27
77.02
76.77
65.81
64.93
34.41
34.28
31.94
29.72
29.67
29.38
26.72
22.71
14.14
1.06
-0.01
OH
O
^{13}C NMR in CDCl$_3$
f1 (ppm)
170
160
150
140
130
120
110
100
90
80
70
60
50
40
30
20
10
0
-10
550
500
450
400
350
300
250
200
150
100
50
0